Spin-Isospin Structure Investigation via $\sigma\tau$-type Transitions starting from ^{64}Zn

Inaugural-Dissertation

zur

Erlangung des Doktorgrades

der Mathematisch-Naturwissenschaftlichen Fakultät

der Universität zu Köln

vorgelegt von

Felix Diel

aus Solingen

Köln 2019

Berichterstatter:	Prof. Dr. J. Jolie Prof. Dr. A. Zilges
Tag der mündlichen Prüfung:	03.05.2019

Zusammenfassung

Atomkerne mit gleicher Massenzahl A und verschiedener Isospinprojektion T_z (Isobare) weisen eine ähnliche Struktur von Zuständen auf. Darüber hinaus werden ähnliche Übergangsstärken für die Übergänge beobachtet, die diese Zustände verbinden. Diese Isospin-Symmetrie-Struktur ist ein direktes Ergebnis der Ladungsunabhängigkeit der Nukleon-Nukleon Wechselwirkung. In der vorliegenden Arbeit untersuchen wir die Isospin-Symmetrie-Struktur des Isospin-Multipletts um ^{64}Zn, welches aus ^{64}Zn selbst und seinen isobaren Nachbarn ^{64}Ga und ^{64}Cu besteht. Zu diesem Zweck haben wir die Ergebnisse eines ^{64}Zn(p,p')^{64}Zn, eines ^{64}Zn(^{3}He,t)^{64}Ga und eines ^{64}Zn(d,^{2}He)^{64}Cu Experiments kombiniert. In diesen Experimenten werden jeweils Spin-$M1$ ($M1_\sigma$), β^--artige Gamow-Teller (GT) und β^+-artige Gamow-Teller-Übergänge induziert. Diese Übergänge sind von gleicher $\sigma\tau$-artiger Natur. Aus diesem Grund sind sie die idealen Werkzeuge, um die Spin- und Isospin-Symmetrie-Struktur des jeweiligen Isospin-Multipletts zu untersuchen. Da die Ergebnisse der ^{64}Zn(^{3}He,t)^{64}Ga und der ^{64}Zn(d,^{2}He)^{64}Cu Experimente bereits vorlagen, liegt das Hauptaugenmerk dieser Arbeit auf der Analyse des ^{64}Zn(p,p')^{64}Zn Experiments. Das ^{64}Zn(p,p')^{64}Zn-Experiment wurde bei 200 MeV und kleinen Streuwinkeln einschließlich 0° an den iThemba LABS in Kapstadt, Südafrika durchgeführt. Um den direkten Vergleich mit Zuständen, die in den anderen Experimenten gemessen wurden zu ermöglichen, wurde eine hohe Energieauflösung angestrebt. Durch die Anwendung von Strahlanpassungstechniken auf das Spektrometersystem konnten wir eine Energieauflösung von 35 keV erreichen. Dadurch konnten wir isolierte Zustände auch im Bereichen mit hoher Leveldichte bis zu einer Anregungsenergie von etwa 13 MeV auflösen. Zum ersten Mal wurden Zustände in ^{64}Zn mit dieser Genauigkeit bis zu so hohen Anregungsenergien beobachtet. Zustände, die von Spin-$M1$-Übergängen angeregt wurden, konnten durch ihre charakteristische Winkelverteilung identifiziert werden. Die Stärke der Übergänge zu diesen Zuständen wurde unter der Annahme einer Proportionalität zwischen Wirkungsquerschnitten und $B(M1_\sigma)$ Werten berechnet. Zustände im ^{64}Zn(p,p')^{64}Zn, im ^{64}Zn(^{3}He,t)^{64}Ga und im ^{64}Zn(d,^{2}He)^{64}Cu-Spektrum wurden in einem Eins zu Eins Verfahren verglichen. Auf diese Weise konnten wir den Isospin der an-

geregten Zustände durch a) ihre Existenz und Nicht-Existenz in den jeweiligen Spektren und b) die relative Stärke der Übergänge zu diesen Zuständen identifizieren. Darüber hinaus haben wir unsere Ergebnisse mit Schalenmodell (SM)-Berechnungen verglichen und eine annehmbare Übereinstimmung für Zustände mit kleinen Anregungsenergien gefunden. Bei größeren Energien überschätzen die SM-Berechnungen die experimentell beobachtete Übergangsstärkenverteilung allerdings deutlich.

Abstract

Atomic nuclei with the same mass number A, but different isospin projection T_z (isobars), exhibit a similar structure of states. Additionally, similar transition strengths are observed for the transitions which connect these states. This isospin symmetry structure is a direct result of the charge independence of the nuclear force. In the present work, we investigated the isospin symmetry structure of the isospin multiplet around ^{64}Zn, which consists of ^{64}Zn and its isobaric neighbors ^{64}Ga and ^{64}Cu. For that purpose, we combined the results of a ^{64}Zn(p,p')^{64}Zn, a ^{64}Zn(^{3}He,t)^{64}Ga, and a ^{64}Zn(d,^{2}He)^{64}Cu experiment. In these experiments, Spin-$M1$ ($M1_\sigma$), β^--type Gamow-Teller (GT), and β^+-type Gamow-Teller transitions are the predominantly induced transitions, respectively. These transitions have the same $\sigma\tau$-type nature. For that reason, they are the ideal tools to probe the spin and isospin symmetry structure of the isospin multiplet in question. Because the results of the ^{64}Zn(^{3}He,t)^{64}Ga and the ^{64}Zn(d,^{2}He)^{64}Cu experiments were already available, the major concern of this work is the analysis of the ^{64}Zn(p,p')^{64}Zn experiment. The ^{64}Zn(p,p')^{64}Zn experiment was performed at 200 MeV and small scattering angles, including 0°, at the high-resolution facility of iThemba LABS in Cape Town, South Africa. To allow a level-by-level comparison with the other experiments, we aimed for a high energy resolution. Through the application of beam-matching techniques to the spectrometer system, we were able to achieve an energy resolution of 35 keV (FWHM). This allowed us to resolve isolated states, even in the region of high level density, up to an excitation energy of about 13 MeV. For the first time, states up to such high excitation energies were observed in ^{64}Zn with this excellent precision. We selected the states excited by Spin-$M1$ transitions by their characteristic angular distribution. The strength of the transitions to these states was calculated assuming a good proportionality between the cross sections and $B(M1_\sigma)$ values. We compared the ^{64}Zn(p,p')^{64}Zn, the ^{64}Zn(^{3}He,t)^{64}Ga, and the ^{64}Zn(d,^{2}He)^{64}Cu spectra using a level-by-level approach. In this way, we were able to identify the isospin of the excited states by a) their existence and non-existence in the respective spectra, and b) the relative strength of the transitions to these states. In addition, we compared our results with

Shell-Model (SM) calculations and found a reasonable agreement for states with small excitation energies. At larger energies, the SM calculations significantly overestimated the strength distribution observed experimentally.

Acknowledgement

I sincerely wish to thank all the people who contributed to the success of this thesis.

My special thanks goes to Prof. Jan Jolie. He supported my wish to go to Osaka, which has influenced my life in every considerable aspect. His encouragement and guidance motivated me to hang on to my ideas throughout the past four years. At the same time, he gave me the space I needed to pursue my own interests.

To Hiro, you are an excellent teacher. Thank you for your patience with my sometimes-hectic mind. Without your expertise in preparation and execution of the experiment, none of this would have been possible.

To Yoshi, for pushing me to my limits.

To Lindsay, the kind heart of iTL, you made my stays in South Africa special in every way. I will always remember this time as a very special part of my life. You have become a true friend.

To Azusa, probably the most underappreciated person at RCNP and a good friend.

To Retief, for your support from the very early stages of our research proposal to the late stages of data evaluation. In addition, I wish to thank all the collaborators who participated in the (p,p') experiment, especially Lindsay, Ricky, Luna, Azu, Sunday, Kevin, Felix, Rosa, Nima, and Vasil for taking shifts and providing reason and wit when needed. Everyone involved in the experiment acknowledged the support by the Deutsche Forschungs Gesellschaft (DFG) who provided the financial support for me and Felix.

Additionally, I wish to thank my collaborators in Room 227, Kerstin and Felix, and all the colleagues in the IKP for providing excellent working conditions. I especially thank

Ronja for the hours of valuable discussions, proof readings, and most importantly, for sharing each other's frustrations, and Prof. von Brentano for always being available for discussion and sharing research interests.

I couldn't have survived the past years without my friends. Simon and Raoul, thank you for handing me a Kölsch and a controller when I needed one. Ina, thank you for your love, your honesty and for always being there.

To my Mom, surely you had the largest impact on my personality as it is today and, therefore, have a considerable share in the success of this work. Bringing Rike and me up all by yourself and still managing to nurture us to where we are now wasn't an easy task. I can't thank you enough for that.

Most importantly, I thank my wife Kathi; without your support I couldn't have even accomplished a fraction of this work. You accept my flaws and build me up when I am at my worst. You and our *Flauschfamilie* Trudi, John, and Snow always give me a safe space to come home to.

I Love You.

Contents

1 Introduction and Fundamental Concepts

A fundamental feature of nuclear structure is associated with the presence of the two kinds of nucleons, the neutron and the proton. The near equality of the mass of these two particles immediately suggests a deep similarity between them (Heisenberg, 1932), and the more detailed study of their role in nuclear processes has revealed a basic symmetry between neutron and proton in all nuclear interactions. - 1969 Bohr and Mottelson [1]

1.1 Spin and Isospin

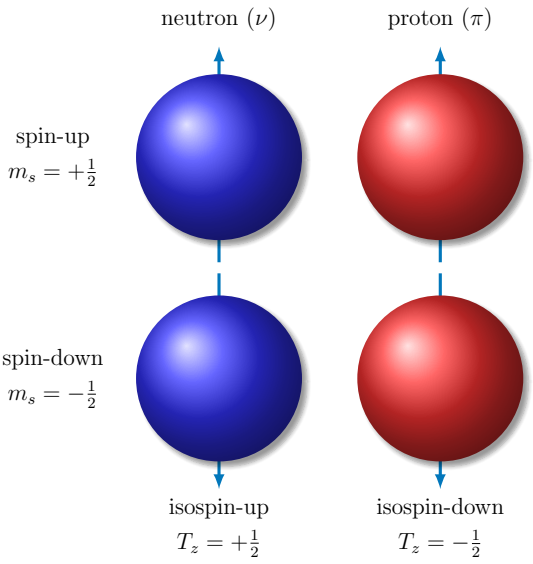

From the observations made by Heisenberg and Bohr & Mottelson, we assume that there is no need to distinguish between protons and neutrons with respect to their nuclear interactions [2]. If this assumption is correct, we can derive two symmetry conditions for the attractive nucleon-nucleon interaction V. First, it is required that V is charge symmetric, i.e., that $V_{nn} = V_{pp}$, and second, it is required that V is charge independent, i.e., that $V_{np} = (V_{nn} + V_{pp})/2$. In reality, both symmetry conditions are broken; however, the deviations are small and the nucleon-nucleon interaction can, therefore, be considered charge-invariant [3]. In this formalism, the proton and the neutron are no longer recognized as different particles and for that reason, we can group them together in the same family of particles, which we call the nucleons [4]. Similar to the degenerate spin-up and the spin-down states of particles, the proton and the neutron

are treated as the two degenerate states of the nucleon. This formalism is called the isobaric spin or, in short, isospin [5]. In analogy to the spin formalism, the nucleon is assigned the total isospin quantum number $T = \frac{1}{2}$. The isospin is quantized along the z-axis with the neutron acting as the isospin-up particle with $T_z = +\frac{1}{2}$ and the proton acting as the isospin-down particle $T_z = -\frac{1}{2}$.[1] It follows that $T_z = (N - Z)/2$ for a nuclear system consisting of N neutrons and Z protons. A direct consequence of the symmetry between the proton and the neutron is that nuclei with the same number of nucleons, i.e., isobars, are expected to have a similar structure. This is especially true for nuclei where the proton and the neutron number is interchanged. Because of the similarity of these nuclei, we call them mirror pairs of nuclei or simply mirror nuclei. The structural symmetry of mirror nuclei and also of isobars is so strong that excited states in these nuclei have the same excitation energies and quantum numbers when coulomb effects are neglected. These states are called analog states. The transitions connecting analog states are called analog transitions, accordingly.

In the next two sections, we will give an overview of the nuclear transitions that probe the isospin and also the spin structure of atomic nuclei. Then, in Sec. (1.6), we will explain how we can combine the study of these transitions to investigate the spin-isospin structure of an isobaric chain.

1.2 Gamow-Teller Transitions

The major concern of this work is the spin-isospin structure of atomic nuclei. The allowed ($\Delta L = 0$) [6] Gamow-Teller (GT) [7] transitions in β decay offer the most direct way to probe the spin-isospin response. In quantum-mechanical terms, GT transitions are mediated by the $\sigma\tau$ operator. The composition of the $\sigma\tau$ operator allows spin excitation ($\Delta S = 1$) through the σ operator as well as isospin excitation ($\Delta T = 1$) through the τ operator. As a result, the Gamow-Teller transitions can selectively probe the spin and the isospin degrees of freedom of an atomic nucleus. The selection rules of the GT transitions are summarized in Tab. (1.1). In general, transitions that are related to isospin excitations ($\Delta T = 1$) are called *isovector* (IV) transitions. On the other hand, transitions that do not include isospin excitation ($\Delta T = 0$) are called *isoscalar* (IS).

On top of GT transitions, Fermi transitions are also observed in β decay. Because of their $\Delta L = 0$ and $\Delta S = 0$ selection rules, Fermi transitions are commonly referred to as the "superallowed" transitions. As a result, only a single state, which is the analog

[1] This is the convenient notation in nuclear physics.

Table 1.1: In this table, the Gamow-Teller and Spin-$M1$ selection rules are summarized.

GAMOW-TELLER and SPIN-$M1$	
$\Delta J = 0, \pm 1$	$J_f = J_i \pm 1$ or 0, but $0 \rightarrow 0$ forbidden
$\Delta T = 0, \pm 1$	$T_f = T_i \pm 1$ or 0, but $0 \rightarrow 0$ forbidden
GT: $\Delta T_z = \pm 1$	$T_{zf} = T_{zi} \pm 1$
$M1_\sigma$:$\Delta T_z = 0$	$T_{zf} = T_{zi}$
$\Delta \pi = 0$	no parity change

state of the ground state of the initial nucleus, is excited. We call this state isobaric analog state (IAS). The transitions to the IAS exhaust the complete Fermi sum rule $\sum B(\mathrm{F}) = N - Z$ [8].

An important observable in nuclear structure studies is the probability of a transition. The probability of a GT transition is measured in the reduced GT transition strength $B(\mathrm{GT})$. In β decay, the strength of a GT transition to a level with energy E_j is expressed in terms of the $f_j t_j$ value, where t_j is the partial half-life to level j and f_j is the corresponding phase space factor:

$$B_j(\mathrm{GT})\lambda^2 = K/f_j t_j, \tag{1.1}$$

with $K = 6143.6(17)$ [9] and $\lambda = g_A/g_V = -1.270(3)$ [10]. The partial half-life t_j is related to the total half-life $T_{1/2}$ of the decaying mother nucleus by:

$$t_j = T_{1/2}/I(E_j), \tag{1.2}$$

where $I(E_j)$ is the feeding to the state j. It should be noted that the accessible excitations in the daughter nucleus are limited owing to the Q-value window of the respective β decay. In addition, the f_j value decreases rapidly as a function of the excitation energy as $\propto (Q_\beta - \mathrm{E_x})^5$ and, therefore, the intensities of higher-lying levels are strongly suppressed [11].

In addition to β decays, GT transitions can also be studied in charge-exchange (CE) reactions such as (p,n), (n,p), $(d,{}^2\mathrm{He})$, $({}^3\mathrm{He},t)$, etc. at intermediate energies and small scattering angles. Under these conditions, the CE reactions share the features of β decays. However, in contrast to the β decays, these studies do not suffer from the Q-value limitation. To obtain an expression for $B(\mathrm{GT})$ values measured in CE reactions, we start from $B(\mathrm{GT})$ reduced in spin (J) [12, 13, 14]. In order to be able to compare

the strengths of GT transitions, the GT matrix elements must be reduced in terms of spin and isospin [15]. Following the convention of Edmonds [16], the expression for $B(\mathrm{GT})$ reduced with respect to the spin (J) matrix element [17] reads:

$$B^{\pm1}(\mathrm{GT}) = \frac{1}{2J_i+1}\left|\langle J_f T_f T_{zf}\|\frac{1}{\sqrt{2}}\sum_{j=1}^{A}(\sigma_j\tau_j^{\pm1})\|J_i T_i T_{zi}\rangle\right|^2 . \tag{1.3}$$

Because $\tau^{\pm1} = \mp(1/\sqrt{2})(\tau_x \pm i\tau_y)$ transforms as a tensor of rank one, the Wigner-Eckart theorem in isospin space can be applied. We get

$$B(\mathrm{GT}) = \frac{1}{2J_i+1}\frac{1}{2}\frac{C_{\mathrm{GT}}^2}{2T_F+1}\left|\langle J_f T_f\|\|\sum_{j=1}^{A}(\sigma_j\tau_j)\|\|J_i T_i\rangle\right|^2 \tag{1.4}$$

$$= \frac{1}{2J_i+1}\frac{1}{2}\frac{C_{\mathrm{GT}}^2}{2T_F+1}[M_{\mathrm{GT}}(\sigma\tau)]^2, \tag{1.5}$$

where C_{GT} is the isospin Clebsch-Gordon (CG) coefficient and $M_{\mathrm{GT}}(\sigma\tau)$ is the GT matrix element. At intermediate energies ($>$ 100 MeV/nucleon) and small momentum transfer q, the CE reaction mechanism becomes more simple [18, 19]. Under these conditions, a well-studied relationship exists between the $B(\mathrm{GT})$ value and the differential cross section of a GT transition [20, 21]:

$$\frac{d\sigma_{\mathrm{GT}}}{d\Omega}(q,\omega) \simeq K(\omega)N_{\sigma\tau}|J_{\sigma\tau}(q)|^2 B(\mathrm{GT}) \tag{1.6}$$

$$= \hat{\sigma}_{\mathrm{GT}}(q,\omega)B(\mathrm{GT}). \tag{1.7}$$

Here, the differential cross section is dependent on the volume integral $J_{\sigma\tau}(q)$ of the effective interaction $V_{\sigma\tau}$ at momentum transfer q, and the kinematic factor $K(\omega)$. In this notation, ω is the total excitation energy of the final nucleus that can be expressed as $\omega = \mathrm{E_x} - Q_{g.s.-g.s.}$. The factor $N_{\sigma\tau}$ is a distortion factor. All three factors in Eq. (1.6) can be integrated into the unit (differential) cross section $\hat{\sigma}_{\mathrm{GT}}(q,\omega)$ in units of $[\frac{\mathrm{mb}}{\mathrm{sr}}]$ [22]. Owing to the momentum mismatch between projectile and ejectile, its value changes as a function of energy (ω). This kinematic effect can be estimated from distorted wave Born approximation (DWBA) calculations. The detailed derivation of $\hat{\sigma}_{\mathrm{GT}}(q,\omega)$ is explained in Sec. (1.6).

1.3 Spin-$M1$ Transitions

Similar to GT transitions discussed above, so-called Spin-$M1$ transitions are also mediated by the $\sigma\tau$ operator [18, 23]. Likewise, they also probe the spin-isospin response of atomic nuclei. However, in contrast to GT transitions, the z-component of the isospin T_z is not changed in Spin-$M1$ transitions [see Tab. (1.1)]. As a result, Spin-$M1$ transitions occur inside the initial nucleus when the spin of a nucleon in a j-unsaturated shell is flipped, i.e., in transitions from the $j_>$ to the $j_<$ orbit. The Spin-$M1$ strength can, therefore, also be interpreted as the extent to which unsaturated spin-orbit partners are occupied in the ground state of the nucleus [24].

We derive the expression for the reduced $M1_\sigma$ transition strength in analogy to Sec. (1.2) by replacing $\tau_j^{\pm 1}$ in Eq. (1.3) with τ_j^0. After applying the Wigner-Eckart theorem in isospin space, we obtain the expression for the reduced Spin-$M1$ strength:

$$B(M1_\sigma) = \frac{1}{2J_i+1}\frac{1}{2}\frac{C_{M1}^2}{2T_F+1}\left|\langle J_f T_f \| \sum_{j=1}^{A}(\sigma_j\tau_j) \| J_i T_i\rangle\right|^2 \tag{1.8}$$

$$= \frac{1}{2J_i+1}\frac{1}{2}\frac{C_{M1}^2}{2T_F+1}[M_{M1}(\sigma\tau)]^2. \tag{1.9}$$

Here, C_{M1} is the isospin CG coefficient $(T_i T_{zi} 10 | T_f T_{zf})$ and $M_{M1}(\sigma\tau)$ is the Spin-$M1$ matrix element [15].

The Spin-$M1$ transitions can be studied very well using hadron inelastic scattering such as (p,p') reactions at intermediate energies and small scattering angles, including 0°. Under these conditions, a simple relation between the differential cross section and the $B(M1_\sigma)$ values, similar to Eq. (1.6) exists:

$$\frac{d\sigma_{M1_\sigma}}{d\Omega}(q,\omega) \simeq K(\omega) N_{\sigma\tau} |J_{\sigma\tau}(q)|^2 B(M1_\sigma) \tag{1.10}$$

$$= \hat{\sigma}_{M1_\sigma}(q,\omega) B(M1_\sigma), \tag{1.11}$$

where $\hat{\sigma}_{M1_\sigma}(q,\omega)$ is the unit cross section for the Spin-$M1$ transitions. The $M1_\sigma$ unit cross section can be calculated from a standard $B(M1_\sigma)$ value. This technique is described in Sec. (1.6).

In addition to the use of hadronic probes, $M1$ transitions can also be studied using electron inelastic scattering reactions and γ-decay. These $M1$ transitions are mediated by the electro-magnetic (EM) interaction. In addition to the IV-type $\sigma\tau$ operator, the EM $M1$ operator (μ) contains an IV orbital component $l\tau$. Furthermore, μ contains an

orbital IS and a spin IS part [13, 14].

$$\mu = \Big[\sum_{j=1}^{A}(g_l^{\mathrm{IS}}\mathbf{l}_j + g_s^{\mathrm{IS}}\mathbf{s}_j) - \sum_{j=1}^{A}(g_l^{\mathrm{IV}}\mathbf{l}_j + g_s^{\mathrm{IV}}\mathbf{s}_j)\tau_{zj}\Big]\mu_N, \tag{1.12}$$

with $\mathbf{s} = \frac{1}{2}\sigma$. τ_{zj} takes the values $\tau_{zj} = 1$ for neutrons (ν) and $\tau_{zj} = -1$ for protons (π). μ_N is the nuclear magneton, and g^{IS} and g^{IV} are the IS and IV combinations of the gyromagnetic factors (g factors), respectively, with: $g_l^{IS} = \frac{1}{2}(g_l^{\pi} + g_l^{\nu})$, $g_s^{IS} = \frac{1}{2}(g_s^{\pi} + g_s^{\nu})$, $g_l^{IV} = \frac{1}{2}(g_l^{\pi} - g_l^{\nu})$, and $g_s^{IV} = \frac{1}{2}(g_s^{\pi} - g_s^{\nu})$. The g factors for bare protons and neutrons are: $g_l^{\pi} = 1$, $g_l^{\nu} = 0$, $g_s^{\pi} = 5.586$, and $g_s^{\nu} = -3.826$.

By exchanging the $\sigma\tau$ operator in Eq. (1.3) with μ and again applying the Wigner-Eckart theorem in isospin space, we get, after some intermediate steps, the expression for the reduced $M1$ transition strength [17]

$$B(M1) = \frac{1}{2J_i+1}\frac{3}{4\pi}\mu_N^2\Big[M_{M1}^{\mathrm{IS}} - \frac{C_{M1}}{\sqrt{2T_f+1}}M_{M1}^{\mathrm{IV}}\Big]^2, \tag{1.13}$$

where $C_{M1} = (T_iT_{zi}10|T_fT_{zf})$ is the isospin CG coefficient and M_{M1}^{IS} and M_{M1}^{IV} are the IS and IV terms of the $M1$ matrix element, respectively, given by:

$$M_{M1}^{\mathrm{IS}} = g_l^{\mathrm{IS}}M_{M1}(l) + \frac{1}{2}g_s^{\mathrm{IS}}M_{M1}(\sigma), \tag{1.14}$$

and

$$M_{M1}^{\mathrm{IV}} = g_l^{\mathrm{IV}}M_{M1}(l\tau) + \frac{1}{2}g_s^{\mathrm{IV}}M_{M1}(\sigma\tau). \tag{1.15}$$

Owing to the large g_s^{IV} value, the IV term usually dominates the $B(M1)$ strength. Depending on the configuration of the initial and the final state, the IS term can interfere destructively or constructively with the IV term. Similarly, the orbital terms can interfere constructively or destructively with the spin terms [25].

1.4 Dynamics of the (p, p') Reaction

Proton inelastic (IE) scattering at intermediate energies and small scattering angles, including 0°, is the ideal tool to probe the spin-isospin response of nuclei. Because the proton has spin $\frac{1}{2}$ and isospin $\frac{1}{2}$, the isoscalar non-spin-flip ($\Delta T = 0$, $\Delta S = 0$), the isoscalar spin-flip ($\Delta T = 0$, $\Delta S = 1$), the isovector non-spin-flip ($\Delta T = 1$, $\Delta S = 0$), and the isovector spin-flip ($\Delta T = 1$, $\Delta S = 1$) modes can be excited [8]. The effective

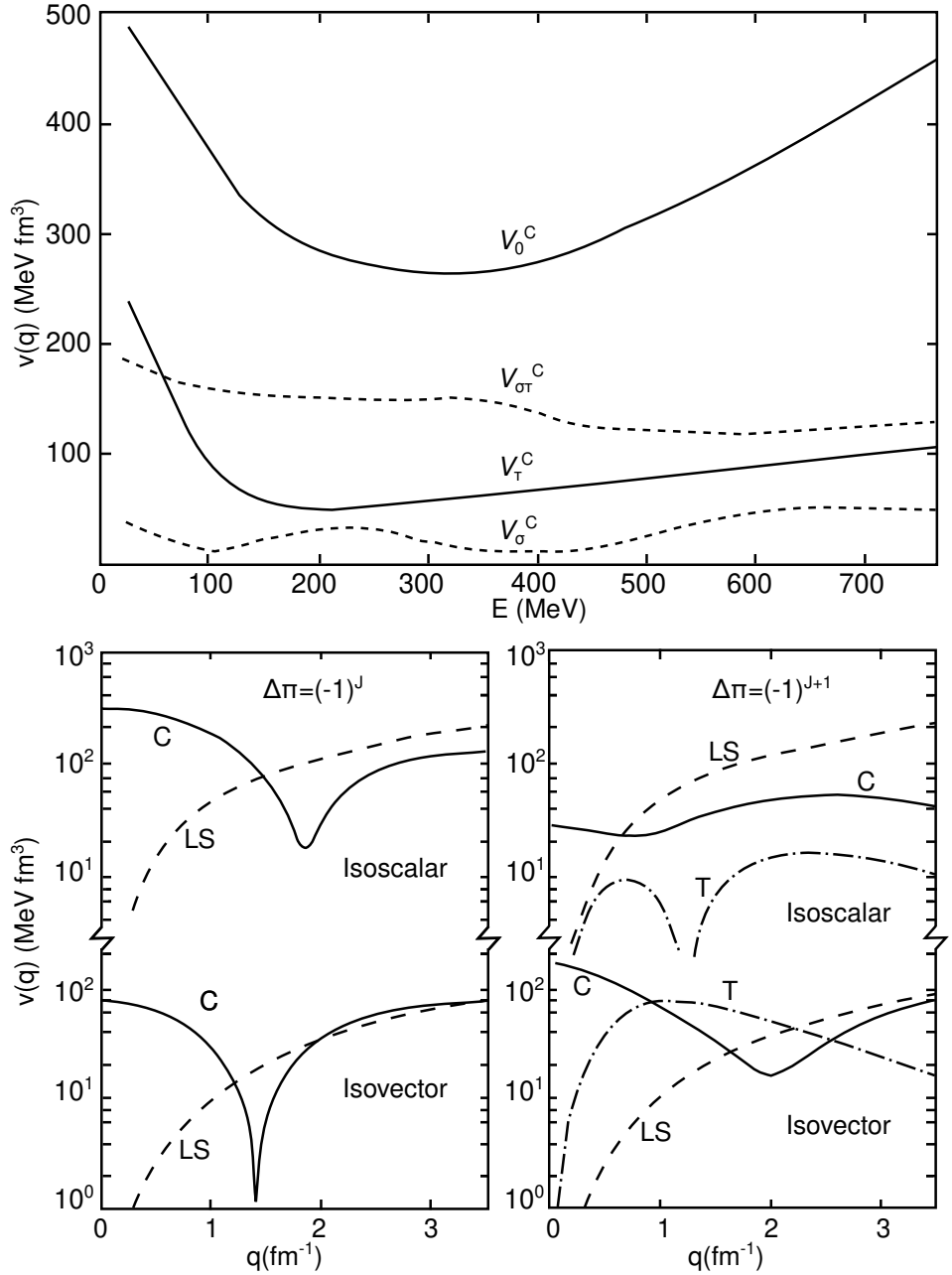

Figure 1.1: Nucleon-nucleon interaction. The energy dependence of the volume integrals of the central components of the interaction is shown at the top. The decomposition of the complete interaction at $E_p = 135$ MeV is shown at the bottom as a function of momentum transfer. C, LS, and T denote central, spin-orbit, and tensor, respectively. The knockout exchange contributions have been included approximately in the central and spin-orbit components. Modified from [19].

nucleon-nucleon interaction involved in the scattering process between the incoming proton p and the i-th nucleon of the target nucleus is given by [18]:

$$V_{ip}(r_{ip}) = V^C(r_{ip}) + V^{LS}(r_{ip})\vec{L}\cdot\vec{S} + V^T(r_{ip})S_{ip}(\hat{r}_{ip}), \tag{1.16}$$

where the spin-orbit and tensor operators are $\vec{L}\cdot\vec{S}$ and $S_{ip}(\hat{r}_i p)$, respectively. As is shown in the bottom part of Fig. (1.1), the spin-orbit and the tensor parts of Eq. (1.16) become small at small momentum transfer $q \leq 0.5$ fm^{-1}. Under these conditions, the interaction is essentially given by the central part:

$$V_{ip}(r_{ip}) = V^C(r_{ip}) \tag{1.17}$$

$$= V_0^C(r_{ip}) + V_\sigma^C(r_{ip})\vec{\sigma}_i\cdot\vec{\sigma}_p + V_\tau^C(r_{ip})\vec{\tau}_i\cdot\vec{\tau}_p + V_{\sigma\tau}^C(r_{ip})\vec{\sigma}_i\cdot\vec{\sigma}_p\vec{\tau}_i\cdot\vec{\tau}_p. \tag{1.18}$$

Figure (1.1) displays the contribution of the effective nucleon-nucleon t-matrix components at momentum transfer $q = 0$, as a function of incident proton energy [19, 23]. Although the central isoscalar interaction dominates at all energies, the spin-flip isovector interaction becomes relatively stronger owing to the broad minimum of the isoscalar interaction between 100 and 500 MeV. As a consequence, the nuclear distortion and multi-step processes are reduced. In addition, the isovector non-spin-flip modes and the isoscalar spin-flip modes are suppressed for (p,p')-and also (p,n)-type reactions and so, the spin-isospin response of atomic nuclei can be very well studied at small scattering angles and intermediate beam energies.

1.5 Collective Excitations

Assuming a shell structure in nuclei, some nuclear excitations can be understood as the promotion of one particle (nucleon) from its original shell to a higher shell [1]. Because a hole is left in the original shell, we call these excitations "one particle - one hole" ($1p-1h$) excitations. In the spectrum, we see the $1p-1h$ excitation mostly as narrow isolated states. On top of these isolated states, we also observe broad resonance-like structures. These resonances are caused by collective excitations in the nucleus, which are composed of many $1p-1h$ excitations participating in phase [11]. Resonances that exhaust a major part of the transition strength of the corresponding sum rule are called giant resonances (GRs). A full analysis of the properties and fine structure of GRs is beyond the scope of the present work; however, a brief summary of the properties of the relevant resonance modes and what can be learned from them is provided.

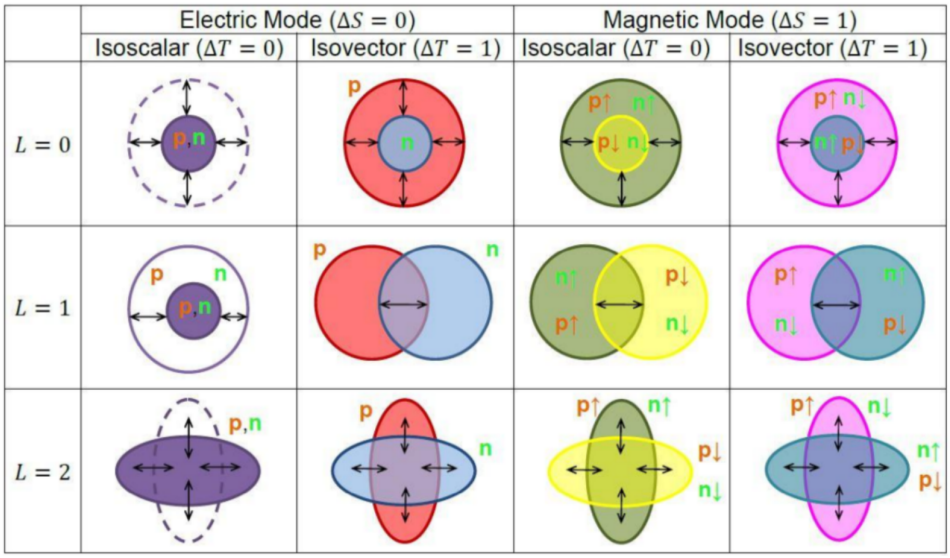

Figure 1.2: A schematic representation of the various collective resonance modes. From [26].

In a macroscopic picture a GR corresponds to a collective motion of many or all nucleons in an atomic nucleus. As stated in [8], this collective motion "can be viewed as a high-frequency, damped, (nearly) harmonic density/shape vibration around the equilibrium density/shape of the nuclear system". The modes of the collective motions are classified by the basic nuclear quantum numbers, i.e., the multipolarity L, the spin S and the isospin T. Resonances in which the spin-up and the spin-down particles move in phase around a common equilibrium are called the *electric* modes ($\Delta S = 0$), while modes where spin-up and spin-down nucleons move out of phase are called *magnetic* modes ($\Delta S = 1$). Similarly, resonances that include protons and neutrons moving in phase are called *isoscalar* modes ($\Delta T = 0$), whereas resonances with protons and neutrons moving out of phase are called *isovector* modes ($\Delta T = 1$). The multipolarity of a collective mode describes the oscillation of particles with respect to an equilibrium shape of the nucleus. The modes are called *monopole* ($\Delta L = 0$), *dipole* ($\Delta L = 1$), *quadrupole* ($\Delta L = 2$) modes and so forth. The various modes are illustrated in Fig. (1.2).

In the spectra of nuclei studied in the context of this work, we mainly observe contributions from three different resonance modes. These resonances are described in the following sections.

1.5.1 The Isovector Spin Giant Monopole Resonance

Behind this elaborate name hides the collective mode shown in the first row of the right-most column of Fig. (1.2). Macroscopically, it can be visualized as an oscillation of the spin-down protons against the spin-up neutrons and vice versa. Owing to the spin-isospin nature of this mode, its excitations are mediated by the $\sigma\tau$ operator. It is, therefore, the collective equivalent of the GT and Spin-$M1$ excitations, described in Sec. (1.2) and (1.3). In the $\sigma\tau_{\pm}$ channel, there exists a simple expression for the total GT resonance (GTR) strength

$$\sum B(\mathrm{GT}^-) - \sum B(\mathrm{GT}^+) = 3(N-Z), \tag{1.19}$$

also referred to as the "Ikeda sum rule limit" [27]. Experimental studies using CE-type (p,n) and (n,p) reactions have found that for nuclei with $N > Z$, only about 60% of the expected sum rule strength could be observed. A similar quenching phenomenon is observed for Spin-$M1$ transitions. Ichimura *et al.* [28] and Wakasa *et al.* [29] discuss the possibility of a mechanism pushing some amount of the GT strength up to ≈ 50 MeV. Possible mechanisms are the $\Delta(1232)$-isobar pushing some GT strength to the Δ excitation energies and the mixing of high-lying $(2p, 2h)$ with low-lying $(1p, 1h)$ states.

1.5.2 The Isovector Giant Dipole Resonance

In 1937, Bothe and Gentner found the first evidence of a giant-resonance phenomenon by measuring the photo-absorption cross section of various materials [8, 30]. The resonance they observed was the isovector giant dipole resonance (IVGDR), which corresponds to an $E1$ electic mode ($\Delta S = 0$) opposite-phase oscillation of protons and neutrons ($\Delta T = 1$) with respect to the center of mass of the nucleus ($\Delta L = 1$). In Fig. (1.2), the IVGDR is represented by the image in the second column of the second row. The IVGDR can be found in all nuclei ranging from the light ^{4}He to the heavy ^{238}U. In the lighter nuclei, the strength distribution of the IVGDR is more fragmented with a width of ≈ 5 MeV, while it takes a more-Lorentzian shape with ≈ 2.5 MeV width in the heavier spherical nuclei [8]. The excitation energy of the centroid of the IVGDR is given by:

$$\mathrm{E_x} = 31.2A^{-1/3} + 20.6A^{-1/6}\ \mathrm{MeV}\ [8], \tag{1.20}$$

and the strength is expressed in terms of the Thomas-Reiche-Kuhn (TRK) sum rule [31, 32]

$$\int_{E_{\min}}^{E_{\max}} \sigma_{\gamma}^{abs} dE = \frac{60NZ}{A}(1+\kappa) \text{ MeV mb [8].} \tag{1.21}$$

Here, κ is a required correction factor owing to meson-exchange contributions.

The IVGDR can be studied through γ absorption or emission, inelastic scattering of hadrons and even specific charge-exchange reactions. Because the IVGDR is strongly excited by virtual-photon Coulomb interaction, it can be studied well in proton inelastic scattering experiments at small scattering angles, including 0° [33]. As a result of the high resolution that can be achieved in proton inelastic scattering experiments, the fine structure of the resonance can be investigated in detail. Although the IVGDR is, in general, very well studied, the damping mechanisms driving the change of the width of the resonance as a function of mass are not fully understood [8]. Here, the examination of the fine structure of the IVGDR provides additional information about this problem. In addition, the structure and the splitting of the resonance is related to the deformation of the nucleus. The systematic study of the IVGDR structure is an indicator for phase-transitions between the different deformation modes [8].

1.5.3 The Pygmy Dipole Resonance

Because the GDR exhausts nearly 100% of the TRK sum rule, only a minor part of the $E1$ strength is expected at lower excitation energies. It was found that the strength split from the GDR is of the order of 1% of the TRK sum rule for stable nuclei, and up to about 5% for exotic nuclei [34]. Owing to its low strength, the low-lying $E1$ strength observed outside the region of the GDR is called the pygmy dipole resonance (PDR) [35]. The first observation of the PDR was made by Bartholomew in 1961, who observed an enhanced γ-ray emission after neutron capture [36]. In 1971, Mohan *et al.* proposed a description of the PDR in a three-fluid hydrodynamical model [37]. In contrast

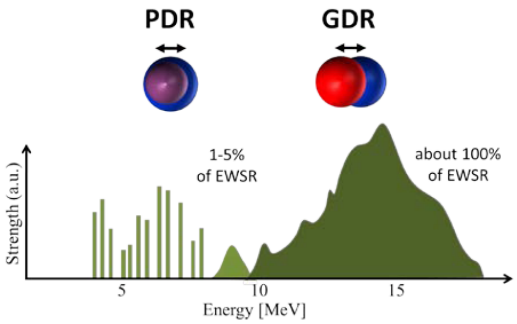

Figure 1.3: Schematic distribution of $E1$ strength in an atomic nucleus showing the splitting into a pygmy dipole resonance (PDR) and a giant dipole resonance (GDR). Octupole-coupled modes, which can generate $E1$ strength at even lower energies are not shown. From [34].

to the GDR mode, which is as an oscillation of all protons against all neutrons [see Sec. (1.5.2)], the PDR can be understood as an oscillation of an isospin-saturated core against the excess neutrons. Figure (1.3) shows the schematic distribution of the GDR and the PDR strength.

Experimentally, the GDR can be studied very well by real photons, Coulomb interaction (virtual photons), and hadronic interactions. The experiments using real photons, such as (γ,γ') nuclear resonance fluorescence (NRF) experiments, have the advantage of a high selectivity with respect to dipole-excited states and a well-known excitation mechanism [35]. Coulomb interaction experiments performed at modern radioactive beam facilities on the other hand, can access exotic nuclei close to the neutron dripline. To study the full dipole strength in stable nuclei, IE proton scattering at forward angles, such as the experiment performed in the context of this work, are excellent tools. Recently, IE proton and α scattering experiments using magnetic spectrometers have been complemented with high-purity germanium (HPGe) detector arrays. The high energy-resolution achieved in these experiments allows a detailed state-by-state investigation, even at high level densities. The results of these experiments suggest that the $E1$ strength splits into a low and a high excitation-energy mode, which are associated with isoscalar and isovector excitations, respectively [34]. The investigation of the PDR conveys valuable information on basic nuclear properties, such as the neutron skin thickness [38] and asymmetry energy [39] and also the mechanisms involved in the stellar r-process nucleosynthesis [40, 41].

1.6 Analog GT and Spin-$M1$ Transitions

Under the assumption that isospin is a good quantum number, analog states in an isospin multiplet of nuclei (isobars) should have a similar structure. On that basis, the strength of transitions connecting analog states, i.e., analog transitions, should also be similar. Figure (1.4) shows the schematic isospin symmetry for an isobaric chain centered around the $N = Z$, $T_z = 0$ nucleus ^{64}Ge. In order to investigate the symmetry structure of such an isospin multiplet, GT and $M1$ transitions studied in various types of experiments are very much complementary. The isospin multiplet illustrated in Fig. (1.4) is the one that was investigated in the present work. In principle however, an isospin structure investigation with the techniques described below is possible for any isospin multiplet with a stable $T_z = +2$ nucleus. Therefore, we will keep the discussion general.

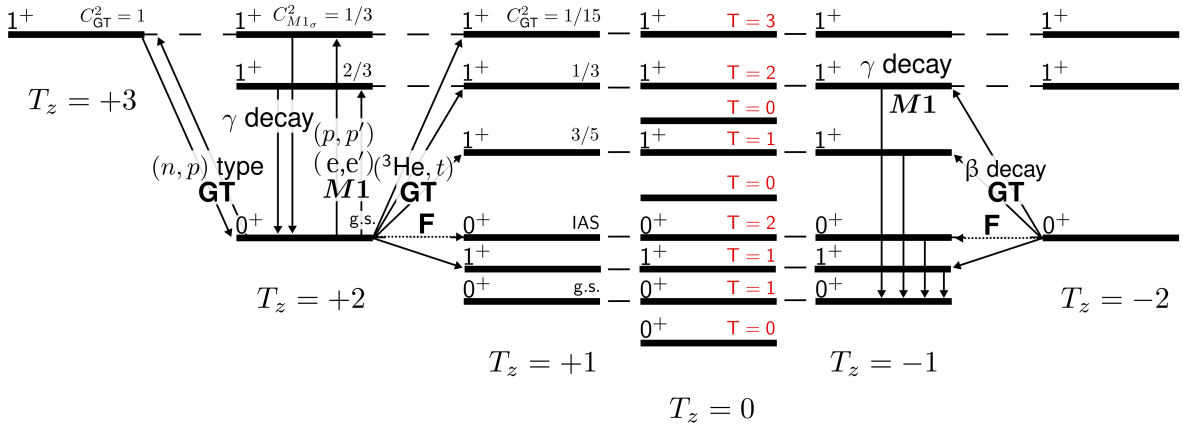

Figure 1.4: This figure shows a schematic drawing of the mirror symmetry in an isospin multiplet. The nuclei are labeled by their T_z values. Excited states are indicated by the solid horizontal bars and analog states are connected by dashed lines. The J^π values of each state are shown on the left side of each solid bar. The isospin CG coefficients of the transitions to a state are shown on the right of the respective solid bar. The isospin value T of each state is indicated for the $T_z = 0$ nucleus. The spin-isospin-type transitions are represented by the solid arrows.

Combination of GT Transitions in β Decays and CE Reactions

As was described in Sec. (1.2), GT transitions and their strengths [B(GT) values] are sensitive to the isospin structure of the final nucleus of the transition. Absolute B(GT) values can be obtained directly from β-decay experiments from the measurement of partial half-lives [see Eq. (1.1)]. In Fig. (1.4), the $T_z = -2$ nucleus is supposed to be unstable with respect to β^+ decay. The GT transitions of the decay are shown by the solid arrows connecting the ground state (g.s.) of the $T_z = -2$ nucleus with the states in the $T_z = -1$ nucleus. In addition, the Fermi transition is indicated by the dashed horizontal arrow. Owing to the GT selection rules [see Tab. (1.1)], GT transitions in β decay starting from the g.s. of a nucleus with isospin $T_0 = |T_z|$ can, in principle, excite states with $T = T_< = T_0 - 1$, $T = T_0$, and $T = T_> = T_0 + 1$. However, states with higher isospin are expected at higher excitation energies [1] and owing to the limited Q value, mostly low-lying states with $T = T_<$ are observed in β-decay spectra. Alternatively, if the so-called *mirror* nucleus is stable, GT transitions to highly excited states can also be studied in CE reactions like (^{3}He,t). In Fig. (1.4), the β^--type (GT$^-$) transitions connecting the g.s. of the $T_z = +2$ nucleus and states in the $T_z = +1$ nucleus are the *mirror* transitions of the $T_z = -2 \rightarrow -1$ β^+ decay. When B(GT) values from the mirror β decay are available, these so-called GT "standards" can be used to calibrate the GT

unit cross section in Eq. (1.7) via:

$$\hat{\sigma}_{\mathrm{GT}} = \left(\frac{d\sigma_{\mathrm{GT}}}{d\Omega}(q,\omega)\right) \Big/ B(\mathrm{GT}). \tag{1.22}$$

We can then determine the strengths of GT transitions in the CE reaction using Eq. (1.7). For heavy or large T_z nuclei, *absolute* $B(\mathrm{GT})$ values from the mirror β decay are often not available. In these cases, *relative* $B(\mathrm{GT})$ values can be calculated from a well-studied relationship between Fermi and GT transition strengths and their respective cross sections [21]:

$$R^2 = \frac{B(F)}{B(\mathrm{GT})} \times \frac{\sigma_{\mathrm{GT}}}{\sigma_{\mathrm{F}}}, \tag{1.23}$$

where R^2 is a function of the nuclear mass A. Typical R^2 values are between 4 for the very lightest and 12 for the heavier nuclei.

GT$^+$ and GT$^-$ Transitions starting from the same Nucleus

In addition to the strength of β^--type GT transitions, the strength of the analog β^+-type GT$^+$ transitions starting from the same nucleus can be measured in CE reactions like (n,p), or (d,^{2}He). In Fig. (1.4) this is illustrated for the nucleus with $T_z = +2$ (^{64}Zn). When the strength of the analog GT$^-$ transition is available, $B(\mathrm{GT}^-)$ values can be used as GT standards to calculate the unit cross section by Eq. (1.22), when the isospin CG coefficients are taken into account. The $B(\mathrm{GT}^+)$ values can then be calculated by Eq. (1.7).

Additionally, we can derive detailed information on the isospin structure of the excited nuclei by comparing analog GT transitions starting from the same initial nucleus. Here, we concentrate our discussion on the $T_z = +2$ nucleus. Owing to the isospin selection rules, only the states with $T = T_>$(here, $= 3$) are excited by the GT$^+$ transitions. In contrast, states with $T = T_<$, $T = T_0$, and $T = T_>$ are excited by the GT$^-$ transitions. By comparing the spectra we can, therefore, immediately identify the $T_>$ states in the GT$^-$ spectrum from the existence of their analog partners in the GT$^+$ spectrum. It should be noted that the $T = T_<$ and $T = T_0$ states cannot be distinguished from one another in this procedure.

Above, we described how mirror and analog transitions can be used as GT standards. However, a GT standard can also be obtained from the so-called "reversed" transition. In Fig. (1.4), the g.s to g.s. transition in the β^- decay of the $T_z = +3$ nucleus is the reversed transition of the GT$^+$ g.s. to g.s. transitions starting from the $T = +2$

nucleus. If the strength of the reversed transition is known, it can also be used as a GT standard. In that case, the spin and isospin geometrical factors, i.e., $\frac{1}{2J_i+1}\frac{C_{\rm GT}^2}{2T_f+1}$, have to be included. As a result of the symmetry between GT transitions in β decays and CE reactions, we can study transition strengths to highly excited states far outside the β-decay Q-value window. In addition, we can identify the isospin value T of individual states, granting us deeper insight into the isospin structure of atomic nuclei.

Combination of Spin-$M1$ and GT Transitions

We can gain even more information on the isospin symmetry structure of the excited nuclei by including Spin-$M1$ transitions in our studies. In Sec. (1.3), we described that the Spin-$M1$ transitions are very similar to the GT transitions because they are mediated by the same $\sigma\tau$ operator. Assuming isospin symmetry, the strengths of analog $M1_\sigma$ and GT transitions should, therefore, also be similar. The strength of $M1_\sigma$ transitions, i.e., $B(M1_\sigma)$ values can be calculated using Eq. (1.11), when the $M1_\sigma$ unit cross section $\hat{\sigma}_{M1_\sigma}(q,\omega)$ is known. In order to calibrate $\hat{\sigma}_{M1_\sigma}(q,\omega)$, we can first calculate a standard $B(M1_\sigma)$ value from the B(GT) value of the analog GT transition [42] using:

$$B(M1_\sigma) = R_{\rm MEC} \times (C_{M1_\sigma}^2/C_{\rm GT}^2) \times B({\rm GT}). \tag{1.24}$$

Here, $R_{\rm MEC}$ accounts for the different contributions of the meson exchange current (MEC) in the $\sigma\tau$ term of the $M1_\sigma$ and GT matrix elements, owing to their τ_0 and $\tau_\pm$ natures [25]. Typical values of $R_{\rm MEC}$ are around 1.3. For example, the comparison of a ^{28}Si(^{3}He,t)^{28}P and a ^{28}Si(e,e') experiment obtained a value of $R_{\rm MEC} = 1.33 \pm 0.17$ [43, 44]. In principle, $R_{\rm MEC}$ values for sd- and pf-shell nuclei are different; however, a value of $R_{\rm MEC} = 1.27 \pm 0.18$ was obtain recently from a comparison of a ^{54}Fe(^{3}He,t)^{54}Co [42] and a ^{54}Fe(e,e') experiment [45, 46]. It is worth noting that the $R_{\rm MEC}$ value of ^{64}Zn, which is studied in the present work, is not known.

From the standard $B(M1_\sigma)$ value, we can then in turn calculate the $M1_\sigma$ unit cross section $\hat{\sigma}_{M1_\sigma}(q,\omega)$ using:

$$\hat{\sigma}_{M1_\sigma} = \Big(\frac{d\sigma_{M1_\sigma}}{d\Omega}(q,\omega)\Big) \Big/ B(M1_\sigma). \tag{1.25}$$

Finally, we can use Eq. (1.11) to calculate the $B(M1_\sigma)$ values for all observed Spin-$M1$ transitions.

Similar to the GT$^+$ and the GT$^-$ transitions starting from the same initial nucleus, we

can also identify the isospin of an $M1_\sigma$ state by comparison with its analog GT states. The symmetry of $M1_\sigma$ and GT states for the transitions starting from the $T_z = +2$ nucleus is illustrated in Fig. (1.4). Owing to the isospin selection rules, only the $T = T_0$ and the $T = T_>$ states are excited in the indicated $M1_\sigma$ transitions. Therefore, the $T = T_<$(here $T = 1$) states can be identified by their existence and non-existence in the GT^- and $M1_\sigma$ spectra. Similarly, we can identify the $T = T_0$(here, $T = 2$) and the $T = T_>$ (here, $T = 3$) states by their existence and non-existence in the $M1_\sigma$ and GT^+ spectra. In cases where information on the GT^+-type transitions is not available, the $T = T_0$ and the $T = T_>$ states can still be distinguished because analog transitions exhibit relative strengths proportional to their relative CG coefficients. Because the ratios of $M1_\sigma$ and GT CG coefficients are different with respect to the isospin of the excited analog state, the isospin of the analog states can be determined from their $B(M1_\sigma)$ to $B(\mathrm{GT})$ ratios.

Combination with EM $M1$ Transitions

In Sec. (1.3), we described how EM $M1_\sigma$ transitions can be measured in IE electron scattering (e,e') and γ-decay experiments. Because the matrix element has a contribution from an isovector spin term $M_{M1}(\sigma\tau)$ [see Eq. (1.15)], similar states as in the Spin-$M1$ transitions are excited. On top of that, the matrix element has contributions from an IS-orbital, an IS-spin and IV-orbital term. These terms can interfere constructively and destructively with the $\sigma\tau$ term; however, they are usually smaller than the $\sigma\tau$ term. The contributions of the additional terms can be studied by comparison of the GT or $M1_\sigma$ strength with the EM $M1$ strength of analog transitions. In addition, based on the assumption that the constructive and destructive interferences are averaged when the $B(M1)$ and $B(\mathrm{GT})$ values of analog transitions are summed, the following relation holds [25]:

$$\sum B(M1) \simeq \frac{3}{8\pi}(\mu_p - \mu_n)^2 \frac{C_{M1}^2}{C_{\mathrm{GT}}^2} R_{\mathrm{MEC}} \sum B(\mathrm{GT}). \tag{1.26}$$

When sufficient analog $B(M1)$ and $B(\mathrm{GT})$ values are available, Eq. (1.26) can be used to determine a value for the contribution of the meson exchange current R_{MEC}.

1.7 Spin-Isospin Transitions starting from ^{64}Zn

The spin-isospin-type transitions are among the most interesting transitions in nuclear physics as they can selectively probe the spin and the isospin degree of freedom of the

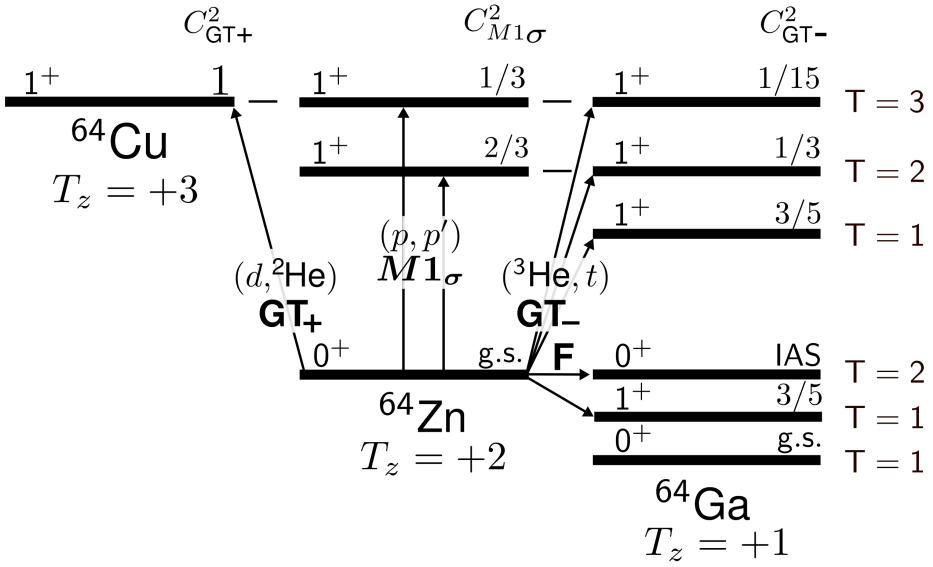

Figure 1.5: A schematic illustration of the isospin structure of GT and Spin-$M1$ transitions starting from ^{64}Zn. J^π values are given for the relevant states. The isospin values T of analog states are shown on the rightmost side. The isospin Clebsch-Gordon coefficients (C^2) are written for each transition. Note that the ^{64}Zn g.s. to ^{64}Ga g.s. transition is forbidden owing to the GT and Fermi (F) selection rules. From [47].

nucleus [8]. Here, we studied the spin-isospin-type Spin-$M1$ and GT transitions starting from the pf-shell $T_z = +2$ nucleus ^{64}Zn. Because ^{64}Zn is the heaviest stable nucleus with $T_z = +2$, the isospin structure of ^{64}Zn and its isobars are of special interest. In addition, GT transitions starting from pf-shell nuclei play an important role in the nuclear synthesis of heavy elements (rp-process) as well as in the core-collapse process of the Type-II supernovae [47, 48].

In order to study the isospin structure of ^{64}Zn and its isobars in more detail, it is necessary to determine the isospin T value of excited states. Owing to the $\Delta T = 1$ nature of the $\sigma\tau$ operator, the GT$^-$ transitions starting from ^{64}Zn excite $J^\pi = 1^+$ states with isospin $T = 1, 2$ and 3 in the final nucleus ^{64}Ga [see Fig. (1.5)] [47]. Although states with higher isospin values generally have higher excitation energies [1], the identification of the isospin value T of individual states is difficult because the distributions of different T states are overlapping in the spectrum. On the other hand, GT$^+$ transitions starting from ^{64}Zn only excite the $T = 3$ states in the final nucleus ^{64}Cu. In [47] and [22] we compared the ^{64}Ga and the ^{64}Cu spectra and were able to identify the prominent $T = 3$ states in both nuclei. However, the GT$^-$ isospin Clebsch-Gordon coefficient ($C^2_{\mathrm{GT}-}$) is small for the GT$^-$ transition to the $T = 3$ states, and as a result, these states were

poorly populated. Consequently, the $T = 3$ assignment of these states in ^{64}Ga is rather ambiguous. As is described in Sec. (1.3), similar to GT transitions, Spin-$M1$ transitions are also mediated by the $\sigma\tau$ operator and so a similar structure of states is excited by GT and Spin-$M1$ transitions starting from the same initial nucleus. The Spin-$M1$ transitions starting from ^{64}Zn excite $J^\pi = 1^+$ states with $T = 2$ and $T = 3$. These states are the analog states of the $T = 2$ and $T = 3$ states in ^{64}Ga and the $T = 3$ states in ^{64}Cu. It is important to note that $T = 1$ states do not exist in ^{64}Zn because of the minimum isospin $T = |T_z| = 2$ of ^{64}Zn. For that reason the $T = 1$ states in ^{64}Ga can be identified directly by comparison of a ^{64}Zn and a ^{64}Ga spetrum because the analog $T = 1$ states do not exist in ^{64}Zn. The identification of the $T = 2$ and $T = 3$ states is more complicated because they are excited by the Spin-$M1$ as well as the GT$^-$ transitions. However, the isospin CG coefficients for the analog transitions are different and thus the $T = 3$ states are enhanced compared to the $T = 2$ states in the ^{64}Zn spectrum. In addition, we can compare the ^{64}Zn and the ^{64}Cu spectra and identify the $T = 2$ and $T = 3$ states via their existence and non-existence in the ^{64}Cu spectrum.

1.7.1 GT$^-$ Transitions[2]

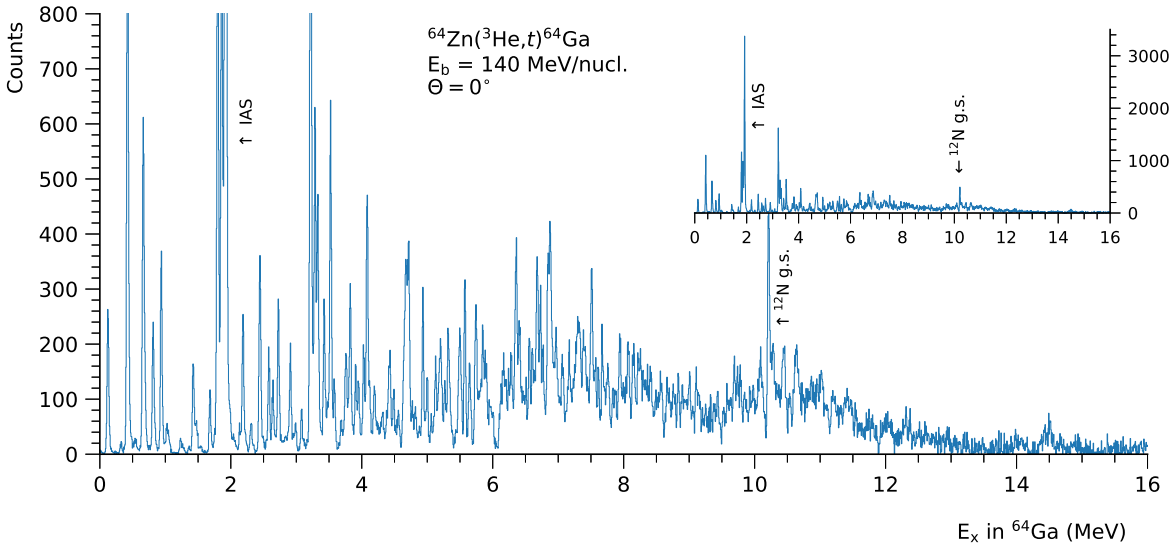

Figure 1.6: A ^{64}Zn(^{3}He,t)^{64}Ga spectrum measured at RCNP. The main figure shows a zoomed ($\times 4$) version of the spectrum. The full spectrum is shown in the top right corner. From [47].

[2]Minor parts of this section were adopted from [22]

We studied the GT$^-$-type transitions starting from ^{64}Zn in a CE-type (^{3}He,t) reaction performed at 200 MeV and small scattering angles, including 0°. The experiment was performed at the Research Center for Nuclear Physics (RCNP) in Osaka, Japan as part of a systematic investigation of stable Zinc nuclei. During the experiment, the ^{3}He beam was boosted to 420 MeV/u by RCNPs K400 Cyclotron. At RCNP, the beam is transported from the accelerator section to the target chamber by a dispersive beam transport system called west-south (WS) course. After making the CE reaction at the target, the outgoing tritons ($t = ^3$H) were analyzed with respect to their momentum by the Grand Raiden spectrometer. By matching the properties of the spectrometer and the beamline, a high energy resolution of 34 keV was achieved. The position and the inclination of the particle ray in the focal plane were measured by a detector system consisting of two multi-wire drift-chambers (MWDCs) and two scintillators. From the detector signals, the particles of interest were selected by their time of flight (TOF) and energy deposit in the scintillators. In the subsequent data analysis, we determined the excitation energy and angular distribution of excited states in ^{64}Ga. A calibrated spectrum is shown in Fig. (1.6). Among these states, GT candidates were selected by their characteristic $\Delta L = 0$ angular distribution. We calculated the strengths B(GT) of the transitions populating the GT states assuming a proportionality between the cross section and B(GT) values [see Eq. (1.7)]. Excitation energies and B(GT) values extracted from the experimental data are listed in Tab. (8.1). Shell-Model (SM) calculations [49] using the GXPF1J [50, 51, 52] interaction reproduce the general behavior of the GT$^-$ structure and hint at the GT$^-$ strength distributions for the three final T values. The comparison to Shell-Model calculations is shown on Fig. (6.2).

1.7.2 GT$^+$ Transitions

The GT$^+$-type transitions starting from ^{64}Zn were studied in a (d,^{2}He) reaction experiment performed at a beam energy of 183 MeV at the Kernfysisch Versneller Instituut (KVI) in Groningen, Netherlands by Grewe *et al.* [53]. The deuterons ($d = ^2$H) were accelerated to the desired energy by the superconducting cyclotron AGOR. A highly enriched (99.7%) ^{64}Zn foil was placed at the target position. Subsequent to the (d,^{2}He) reaction, the two outgoing protons were analyzed according to their momentum by the Big-Bite magnetic spectrometer (BBS) and detected in coincidence by the EuroSuperNova detector (ESN detector). Optimal energy resolution of 115 keV was achieved through the application of dispersion matching to the beamline and the BBS. Measurements at spectrometer angles $\Theta_{\mathrm{BBS}} = 0°$, 2.5° and 4° were performed. These

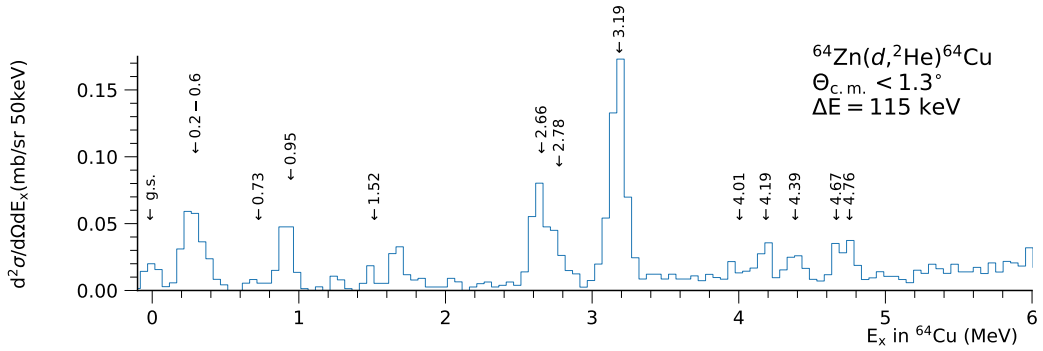

Figure 1.7: A ^{64}Zn(d,^{2}He)^{64}Cu spectrum measured at KVI. The identified GT$^+$ states are indicated by their excitation energies. From [53].

measurements allowed the identification of GT$^+$ candidates in ^{64}Cu owing to their characteristic $\Delta L = 0$ angular distribution. B(GT) values were determined from the cross section of states in the 0° spectrum. A standard B(GT) value was obtained from the β^- decay of the ^{64}Cu ground state. Figure (1.7) shows the 0° spectrum. The extracted B(GT) values are summarized in Tab. (8.1). It is worth pointing out that the GT$^+$ transitions were also measured in a ^{64}Zn(t,^{3}He)^{64}Cu reaction experiment performed at 115 MeV/nucleon [54]. However, the energy resolution was $\approx$ 250 keV and for that reason, individual states could not be resolved. In the following chapters, we will therefore focus our discussion on the GT$^+$ results obtained in the (d,^{2}He) reaction experiment [53].

1.7.3 Spin-$M1$ Transitions

The analysis and evaluation of the Spin-$M1$ transitions in ^{64}Zn, measured in a ^{64}Zn(p,p') experiment at iThemba LABS is the main component of this work. A detailed overview of the iThemba LABS facility and the techniques employed during the experiment is given in Chap. (2). In addition, we briefly summarize the experiment itself in a short experiment report in Chap. (3). In Chap. (4), we describe the analysis of the raw data to obtain high-resolution spectra and in Chap. (5) we explain how we analyzed the spectra to retrieve information about the involved physics. Finally, the results are summarized in Chap. (6) and (7).

2 Experimental Instruments and Techniques

2.1 Milestones of 0° Measurements

The first 0° (^{3}He,t) reaction experiments were performed in 1985 at the Kernforschungsanlage (KFA) in Jülich, Germany. In 1986, dispersion matching was applied for the first time to the beamline and the BIG KARL [55] spectrometer. However, the attainable energies in these experiments were limited because of the 45 MeV beam energy of the KFA cyclotron. In the same year, the $K600$ spectrometer was commissioned at the Indiana University Cyclotron Facility (IUCF) in Bloomington (IN), USA. At IUCF, the Separated Sector Cyclotron (SSC) allowed to achieve much higher beam energies around 100 MeV per nucleon. Through the development of dispersion matching for the IUCF $K600$ spectrometer [56], an energy resolution of 17 keV at a beam energy of 200 MeV was achieved in 0° (^{3}He,t) reaction experiments. In the same year iThemba LABS in Cape Town, South Africa received the blueprints for the $K600$ spectrometer as a donation from IUCF. In 1990, proton (p,p') and alpha (α,α') inelastic scattering measurements at 0° became possible at IUCF owing to the development of the transmission and forward angle mode for the $K600$ spectrometer [57, 58]. On top of that, the off-focus mode was developed for the $K600$ spectrometer in 1993 [59], which significantly increased the resolution of the vertical scattering angle. This technique was adopted by the Research Center for Nuclear Physics in Osaka, Japan in 1997 [60]. In 1999, the last 0° (p,p') experiment was performed at the $K600$ by a collaboration of IUCF and RCNP. After it's decommission, the $K600$ was shipped to RCNP and was employed as a bending magnet in the newly developed WS-beamline [61]. In 2000, the application of beam dispersion matching to the RCNP spectrometer system, consisting of the new WS-beamline and the Grand Raiden spectrometer, achieved an energy resolution of 35 keV (FWHM) at an incoming beam energy around 100 MeV/u [11, 62]. In 2004, the first high resolution 0° (p,p') reaction measurements were performed at RCNP [63]. Only one year

later, similar experiments became possible at the $K600$ spectrometer at iThemba LABS [41]. In the recent years, the $K600$ as well as the Grand Raiden were coupled to the HPGe arrays, AFRODITE and CAGRA, respectively, to perform (p,p'γ) coincidence experiments. Today, these experiments are the benchmark for IE scattering measurements at 0°.

2.2 The High-Resolution Facility at iThemba LABS

The schematic outline of the iThemba[1] Laboratory for Accelerator Based Sciences (iThemba LABS) is shown in Fig. (2.1). The $K = 200$[2] Separated Sector Cyclotron (SSC) forms the core of the facility. It can produce beams of charged particles for nuclear physics research, isotope production and radio therapy [64]. Two Solid Pole injector Cyclotrons (SPC1 and SPC2) provide the pre-accelerated ion beams for the SSC. The protons used in the present experiment were produced by the external Electron Cyclotron Resonance (ECR) ion source of SPC2. They were pre-accelerated by SPC2 and guided to the SSC through the K and the J beamlines. After being boosted to 200 MeV by the SCC, the proton beam was directed to the $K600$ spectrometer via the X, the P, and the S beamline.

2.2.1 The K600 Spectrometer

A dipole magnet works on an achromatic beam of charged particles in a manner similar to the way in which a prism works on white light [see Fig. (2.5)]. When the charged particles enter the dipole magnet, they are dispersed by the magnetic field according to their momentum. Quadrupole magnets (also called quadrupole lenses) have a similar effect on charged particles that convex optical lenses have on light. When an incoming particle ray passes through the quadrupole, it is bent towards the beam axis. Quadrupole magnets are, therefore, well suited for the focusing and defocusing of a particle beam. It should be noted that in contrast to optical lenses, magnetic lenses focus the beam in one plane and, at the same time, defocus the beam in the perpendicular plane [65]. In addition to dipole and quadrupole magnets, higher-order combinations of magnetic multipoles are employed in ion optics. These elements are applied for the sophisticated

[1] In the Zulu language native to South Africa, iThemba translates to the word "hope".
[2] K is the energy constant of a magnetic device with $K = \frac{mE}{q^2}$
[3] This type of viewer was developed by K. Hatanaka who provided one to iThemba LABS. At iThemba LABS, therefore, it is simply referred to as 'The Hatanaka'.

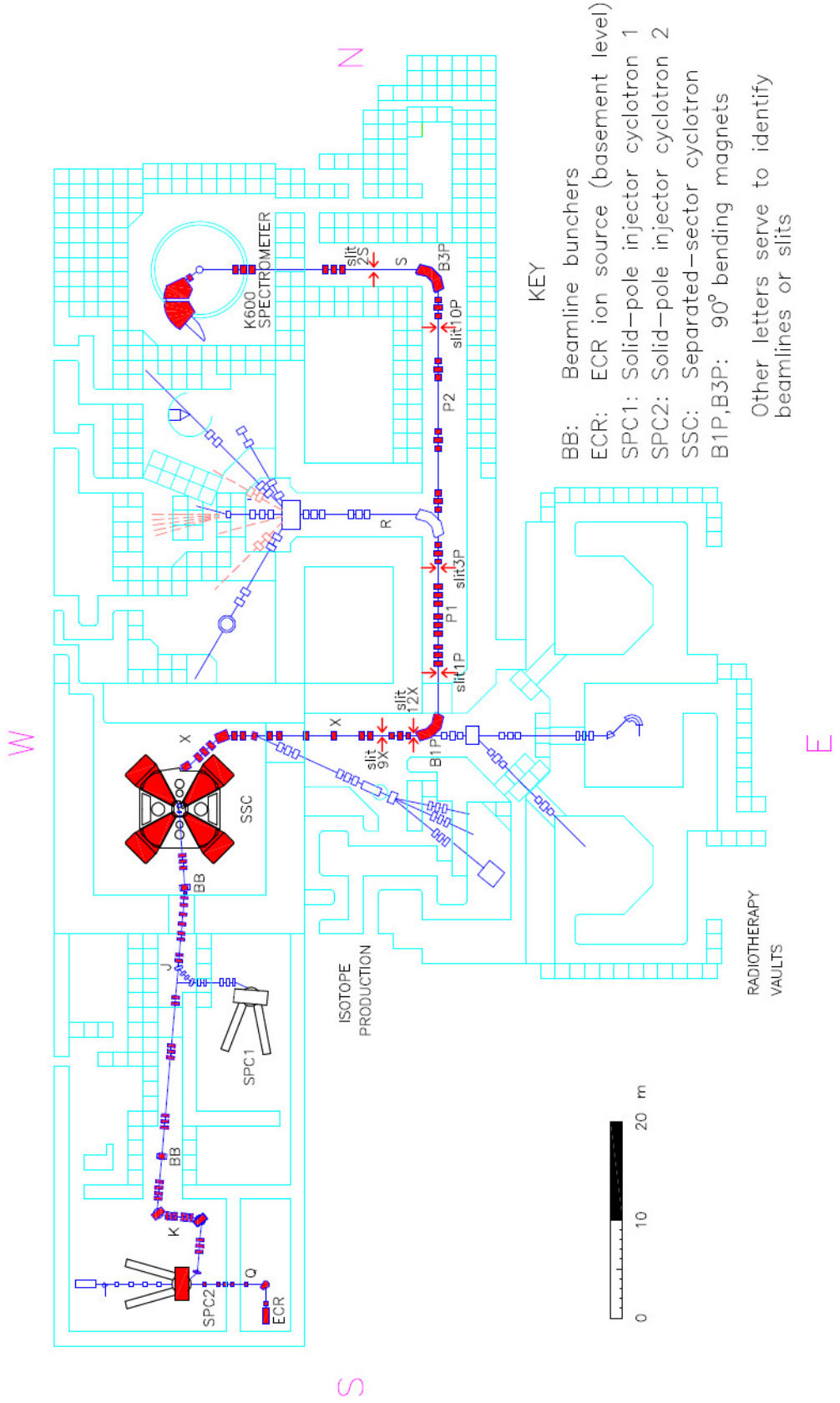

Figure 2.1: Schematic overview of the iThemba LABS cyclotron facility. From [41].

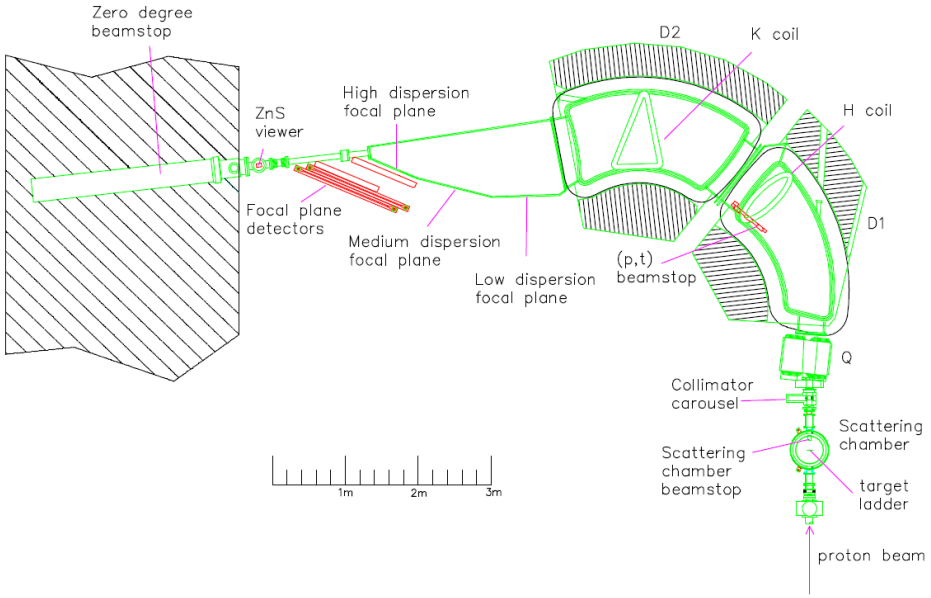

Figure 2.2: A schematic overview of the $K = 600$ zero-degree facility. The focal plane detectors are positioned in the high-dispersion focal plane. The (p, t) beam-stop is removed in (p,p') measurements. The zero degree beamstop is installed in the wall behind the $K600$. With the fluorescing ZnS viewer[3], the spatial shape of the beam can be visualized. From [41].

shaping of the particle beam, such as the reduction of aberration effects.
In the K=600 QDD magnetic spectrometer (hereafter referred to as 'the $K600$'), several magnetic elements are combined to achieve the optimal ion-optical conditions for high-resolution nuclear spectroscopy. The combination of the two dipole magnets 'D1' and 'D2' [see Fig. (2.2)] allows for the variation of the momentum dispersion $(x|\Delta p/p)$ (nomenclature adopted from [65]) between -6.2 and -9.8%. As a result, three distinct focal planes, i.e., the *high*-, *medium*-, and *low*-dispersion focal planes are available. The properties of the high- and the medium-dispersion focal planes of the $K600$ are summarized in Tab. (2.1). At the entrance of the $K600$, a quadrupole 'Q' is installed, which is used to achieve the vertical focusing of the beam. In addition, two trim coils, namely the 'H coil' and the 'K coil', are located inside the dipole magnets. The H and the K coils are both used to optimize scattering angle (Θ_{scat}) dependent momentum variations. The H coil, located in D1, is designed to act like a hexapole element to reduce $(x|\Theta^2)$ aberrations, while the K coil in D2 acts like a quadrupole element to reduce first-order $(x|\Theta)$ variations.

Magnetic spectrometers like the $K600$ are the ideal tools for high-resolution nuclear spectroscopy. They become even more powerful when they are coupled to a dispersive

Table 2.1: Calculated ion-optical properties near the central momentum of the medium- and high-dispersion focal planes of the $K600$ magnetic spectrometer in vertical focus mode. Taken from [41].

Matrix element/ characteristic	Medium dispersion R=1.00	High dispersion R=1.49
$(x\|x)$	-0.52	-0.74
$(\Theta\|\Theta)$	-1.89	-1.37
$(y\|y)$	-5.45	-7.05
$(\phi\|\phi)$	-0.20	-0.13
$(x\|\frac{\Delta p}{p})$	-8.4 cm/%	-10.9 cm/%
$p_{max}/\ p_{min}$	1.097	1.048

beamline that allows for the application of beam-matching techniques. This procedure is described in Sec. (2.3).

2.2.2 The Focal-Plane Detector System[4]

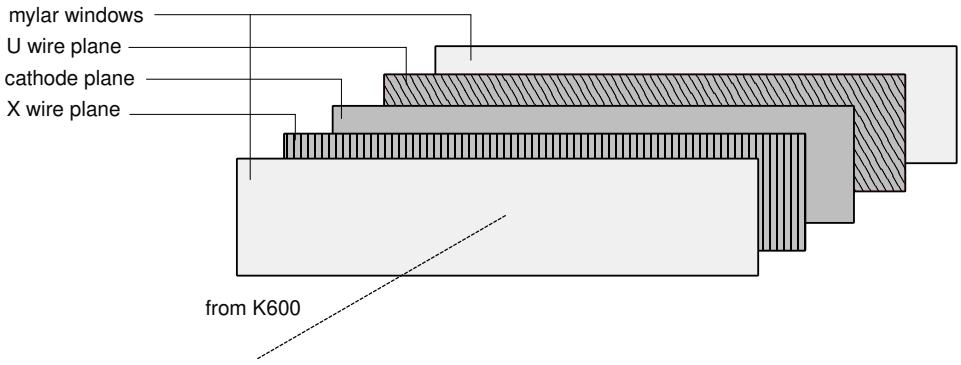

Figure 2.3: Schematic drawing of the components of a multi-wire drift-chamber (MWDC).

A crucial part of nuclear spectroscopy measurements is the precise determination of the excitation energy and the cross section of resonances in atomic nuclei. In addition, the angular distribution of the cross section of a resonance carries information about the angular momentum transferred in the initial nuclear reaction. Therefore, it is important to also determine the scattering angle of the nuclear reaction products.

At iThemba LABS, this is achieved by a position-sensitive focal-plane detector system consisting of two multi-wire drift-chambers (MWDCs) and two scintillators installed at

[4]Minor parts of this section were adopted from [22]

the focal-plane position of the $K600$ spectrometer [see Fig. (2.2)]. All detectors are inclined 32.2° relative to the central ray of the beam axis. The scintillators are positioned after the MWDC cluster and are used for particle identification, Time-of-Flight (tof) measurements and event triggering. The $K600$ distributes the incoming particle beam according to the momenta of its constituent particles along the horizontal axis. Using the MWDCs, the position of the reaction products, which is proportional to their energy loss at the target position, can be measured. In addition, by concatenating the two chambers, the inclination of the beam rays can be determined. From the information about the inclination of the beam rays at the focal plane, the scattering angle at the target position can be deduced. Figure (2.3) shows a schematic drawing of the MWDC components. Two signal-wire planes arranged in an XU configuration are combined in each of the MWDCs. The X wire plane consists of 198 signal wires with 4 mm spacing, interspersed between 199 field-shaping wires. The U wire plane is inclined at an angle of 50° with respect to the scattering plane. In the U plane 143 signal wires and 144 field-shaping wires are mounted. Similar to the X plane, the spacing between the U wires is also 4 mm. All wires are made of gold-plated tungsten. The X and U wire planes of each MWDC are sandwiched between three cathode planes made of 20-μm-thick aluminum foils. When used for proton detection, a negative voltage of 500 V is applied to the field shaping (guard) wires and -3500 V is applied to the cathode planes. The MWDCs are filled with a gas mixture composed of 90% Ar and 10% CO_2 that is isolated from the atmosphere by two 25-μm-thick mylar planes. The MWDC signals are pre-amplified and discriminated by 16-channel electronic cards [66] before being processed by multi-event Time-to-Digital Converters (TDCs) [41, 67]. The position resolutions of the X and U wires planes are ~ 0.35 mm (FWHM) and ~ 0.8 mm (FWHM), respectively. In a typical (p,p') experiment performed at 200 MeV and 0° scattering angle, a resolution of 31 keV/mm can be achieved. Therefore, the resolution of the MWDCs is more than sufficient to obtain high-resolution spectra. The efficiency of each of the wire planes is $\sim 92 - 94\%$, which results in an overall tracking efficiency of $\sim 74\%$ [41].

Behind the MWDCs, two rectangular plastic scintillators (1219×102 mm^2) with a thicknesses of 12.7 and 6.35 mm are installed. A total of four photomultiplier tubes are installed with one tube at each end of the scintillators [see Fig. (2.4)]. The signals from these tubes trigger the MIDAS data acquisition system (DAQ) [68]. In addition, the signals provide information for identification of the penetrating particle because the intensity of the signals is proportional to the energy loss of the particle in the scintillators.

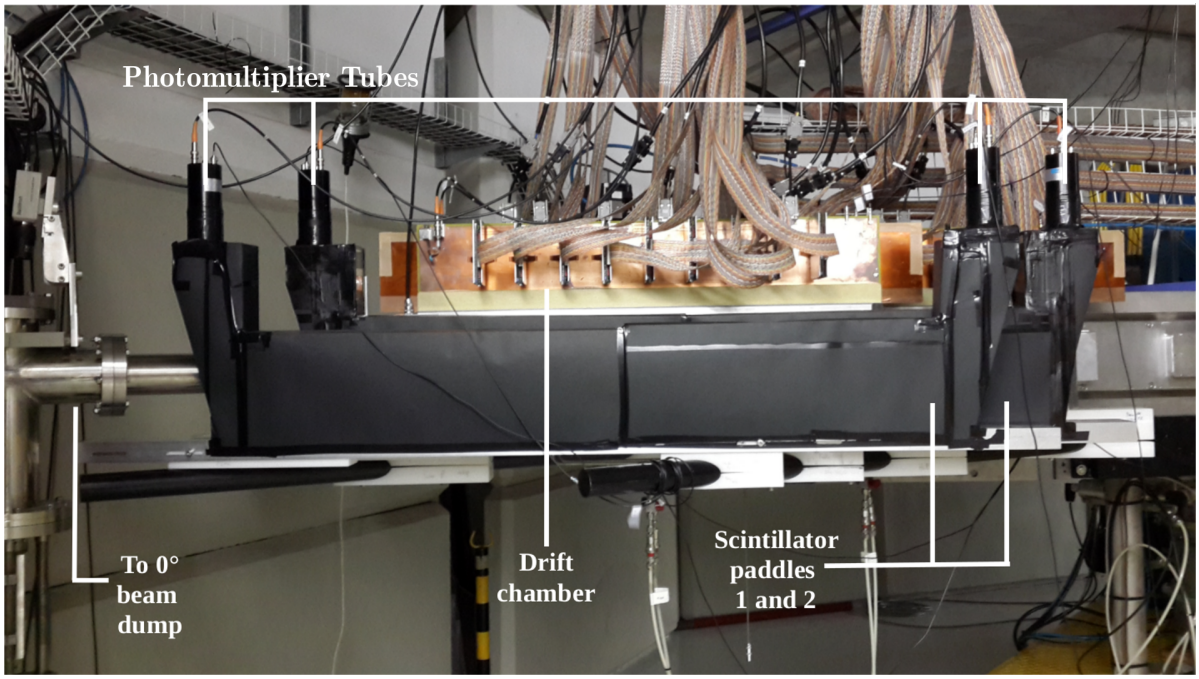

Figure 2.4: The Detector system installed at iThemba LABS. In this perspective, the $K600$ is located behind the detector system and the beam is coming in the direction towards the reader. The 0° beam dump for beam particles is located on the left-hand side of the picture. The scintillators are wrapped in opaque foil to protect the photomultiplier tubes from direct light. Modified from [26].

2.3 Beam-Matching Techniques[5]

In general, the resolution of nuclear spectroscopy is limited by the momentum spread ($\pm\frac{\Delta p}{p}$) of the beam provided by the accelerator [60]. In 1959, Cohen [69] introduced the technique of *lateral dispersion-matching*. Through the application of this method, the performance of a spectrometer system is unchained from the momentum resolution of the incoming beam. Figure (2.5) illustrates the effects of matching techniques on a beam with small emmitance (also referred to as a pencil beam).

(a) In the situation shown in Fig. (2.5) (a) no matching conditions are applied. Therefore, the beam is transported in the achromatic mode. Under this condition, the beam is focused on the target for all possible values of p inside the momentum spread of the beam. After entering the spectrometer, the particles are dispersed

[5]Parts of this section were adopted from [22]

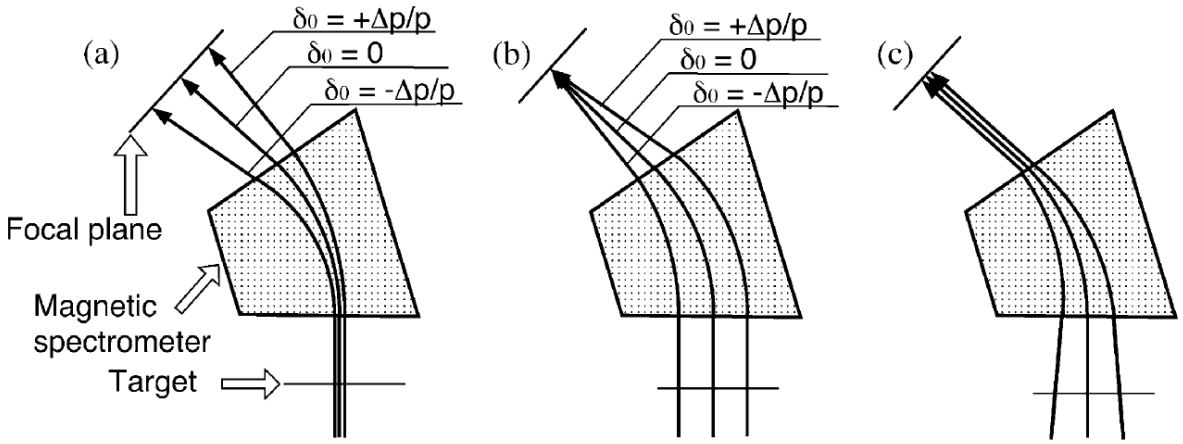

Figure 2.5: Schematic ion-beam trajectories under different matching conditions.
(a) Achromatic mode,
(b) when lateral dispersion-matching is realized,
(c) and when lateral and angular dispersion-matching are realized.
From [62].

according to their momentum. For that reason, the momentum spread of the initial beam is translated to a lateral position-spread at the focal-plane position. The achievable resolution is therefore limited to the momentum spread of the beam.

(b) Under the condition of *lateral dispersion-matching*, shown in Fig. (2.5) (b), the beam is dispersed according to its momentum spread by the beamline preceding the target. If this is done carefully, the dispersion of the spectrometer and the dispersion of the beamline accurately cancel out. In this way, the resolution of the spectrometer system is independent of the momentum spread inside the beam.

(c) When *angular dispersion-matching* is additionally realized, as shown in Fig. (2.5) (c), the dispersion of the beamline is set up such that particles with different p strike the target at different positions and at different incoming angles. By adjusting the inclination angles of the incoming particles at the different positions of the target, the particles leave the spectrometer in parallel rays at the same position. In addition to a high lateral resolution, a good angular resolution for the scattering angle is achieved.

2.3.1 Derivation of Transport Parameters

Here, the notation was chosen in accordance with *T. Wakasa et al.* [61], *S.A. Martin et al.* [55] and the computercode TRANSPORT [70]. The initial coordinates of an arbitrary charged particle with respect to the central beam-trajectory at the source point of the spectrometer system are given by x_0 (initial position-deviation), θ_0 (angle deviation) and δ_0 (fractional momentum-deviation). From the initial source-point to the focal plane, the components are transformed by two 3×3 transport matrices (**B** for the beamline and **S** for the spectrometer) and the target function T. The transformations of the complete spectrometer system starting from the source point $\mathbf{x_0}$ can be summarized by the following expression, which was adopted from [26, 55]:

$$\mathbf{B}\begin{pmatrix} x_0 \\ \theta_0 \\ \delta_0 \end{pmatrix} \rightarrow \begin{pmatrix} x_1 \\ \theta_1 \\ \delta_0 \end{pmatrix} \Rightarrow \mathbf{T}(\begin{pmatrix} x_1 \\ \theta_1 \\ \delta_0 \end{pmatrix}) \rightarrow \begin{pmatrix} x_2 \\ \theta_2 \\ \delta_2 \end{pmatrix} \Rightarrow \mathbf{S}\begin{pmatrix} x_2 \\ \theta_2 \\ \delta_2 \end{pmatrix} \rightarrow \begin{pmatrix} x_{\mathrm{fp}} \\ \theta_{\mathrm{fp}} \\ \delta_{\mathrm{fp}} \end{pmatrix}$$

beamline transf.	in front of target	target transf.	after target	spectr. transf.	at K600 focal plane

The matrix elements of **B** and **S** are denoted as $b_{\mu\nu}$ and $s_{\mu\nu}$ with $\mu, \nu = 1, 2, 6$ for position, angle and momentum, respectively. A full transformation of the spectrometer system with respect to **B** and **S** can be written as

$$\begin{aligned} x_{\mathrm{fp}} = {} & x_0(s_{11}b_{11}T + s_{12}b_{21}) \\ & + \theta_0(s_{11}b_{12}T + s_{12}b_{22}) \\ & + \delta_0(s_{11}b_{16}T + s_{12}b_{26} + s_{16}C) \\ & + \Theta(s_{12} + s_{16}K) \end{aligned} \tag{2.1}$$

$$\begin{aligned} \theta_{\mathrm{fp}} = {} & x_0(s_{21}b_{11}T + s_{22}b_{21}) \\ & + \theta_0(s_{21}b_{12}T + s_{22}b_{22}) \\ & + \delta_0(s_{21}b_{16}T + s_{22}b_{26} + s_{26}C) \\ & + \Theta(s_{22} + s_{26}K), \end{aligned} \tag{2.2}$$

where K and C are kinematic factors, T describes the target function and Θ is the relative scattering angle [44]. The detailed derivation of these functions is given in App. (8.1).

When the matching conditions are achieved, the resolving power of the spectrometer is given by

$$R = \frac{1}{2x_0}\frac{s_{16}}{M_{\text{Ov.}}}, \tag{2.3}$$

where $M_{\text{Ov.}}$ is the overall magnification given by $M_{\text{Ov.}} = s_{11}b_{11}T - s_{16}b_{21}K$.

2.3.2 Beam-Matching Techniques in Practice

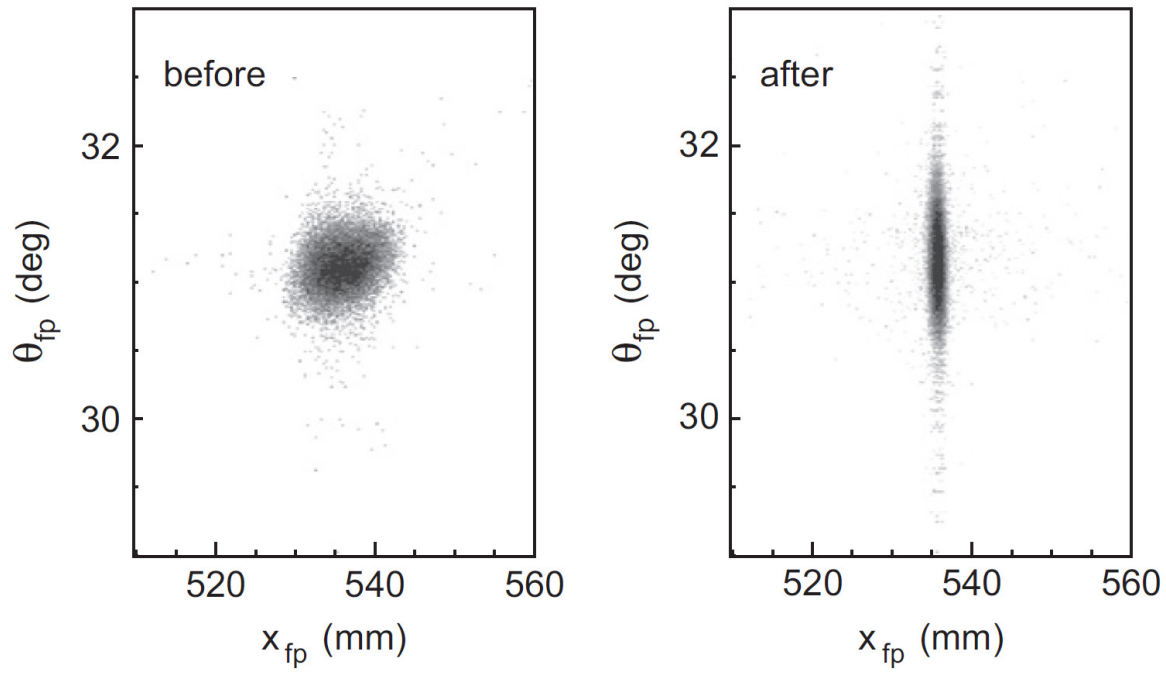

Figure 2.6: The faint-beam image in the $(x_{\text{fp}}, \theta_{\text{fp}})$ scatterplot before and after dispersion and focus matching were achieved for $E_p = 200$ MeV. From [41].

As described above, when none of the matching conditions are realized, the momentum spread of the beam is translated to a lateral spread of the beam in the focal plane. The focal-plane beam-image under this condition is shown on the left of Fig. (2.6) for a faint-beam [62] measurement [see Sec. (2.3.3)][6]. In order to achieve a high energy-resolution, the position of the beam particles in the focal plane has to be independent from the initial momentum-deviation from the central beam-ray δ_0. Effectively, this means that the lateral image of the beam in the focal plane has to be minimized. This condition is shown on the right in Fig. (2.6). Recalling Eq. (2.1), we see that this can be achieved when the coefficients of the θ_0, δ_0 and Θ terms are minimized. In addition, the beam

[6]This corresponds to part (a) of Fig. (2.5).

image at the source point (the x_0 coordinate) should be small. In the same way, when a good angular resolution is requested, angular dispersion-matching has to be realized as well [this is not shown in Fig. (2.6)]. This requires the minimization of the coefficient of δ_0 in Eq. (2.2), which has a large influence on the angular resolution when *lateral dispersion-matching* is achieved.

In order to achieve *lateral* and *angular dispersion-matching* simultaneously, the requirements stated above for the matrix elements of $\mathbf{B}$ and $\mathbf{S}$ have to be met. The results are summarized in Eqs. (2.4) to (2.7) as follows:

$$b_{12} = \frac{s_{12}}{s_{11}} b_{22} T \tag{2.4}$$

$$b_{16} = -\frac{s_{16}}{s_{11}}(1 + s_{11}s_{26}K - s_{21}s_{16}K)\frac{C}{T} \tag{2.5}$$

$$b_{26} = (s_{21}s_{16} - s_{11}s_{26})C \tag{2.6}$$

$$s_{12} = -s_{16}K. \tag{2.7}$$

In order to achieve the *lateral dispersion-matching* conditions, a beam-transport system that can compensate for the momentum spread of the beam is required. At iThemba LABS, a dispersive beam-transport system realized through the P and the S beamline is installed [see Fig. (2.1)]. In combination with the $K600$ spectrometer, this forms the spectrometer system. Slit 9X separates the spectrometer system from the accelerator complex and, therefore, serves as the source point $\mathbf{x_0}$. In contrast to other facilities such as RCNP, a hardware slit-system (9X) has to be used to limit the beam spread at the object-point position. It should be noted that scattering from this slit can introduce additional beam halo.

In order to achieve the conditions necessary for dispersion matching, the horizontal and the vertical emittance[7] of the beam should be $\sim 5\pi$ mm mrad and $\sim 1.5\pi$ mm mrad, respectively [26]. At iThemba LABS, three harps are installed in the S-Line to ensure these properties. In general, before dispersion matching can be performed, the K- and H-coils settings are adjusted to reduce $(x|\Theta)$ and $(x|\Theta^2)$ aberrations. A calibration target is placed at the target position. As a result of the aberrations, the spectral line of an excited state of the calibration target is distorted in the focal plane. When the K- and the H-coil are adjusted correctly, a straight vertical line is visible. Nowadays, however, the aberration effects can be corrected in the offline software analysis. For

[7]The emittance can be visualized as an ellipse in the position and momentum phase space.

that reason, minimal time is spent setting the $K600$ magnetic coils. Because the setting of the coils changes the matrix elements of the **S** matrix, they must be fixed before dispersion matching can be performed. For the same reason, the coil settings are kept constant relative to the other ion-optical elements in the spectrometer throughout the experiment.

Finally, dispersion matching can be applied to the spectrometer system. The beam is tuned to the conditions required for the experiment and the faint-beam method is implemented. In order to measure the quality of the beam directly, the target ladder in the scattering chamber is moved to an empty target frame. To achieve the matching conditions, the ion-optical elements of the beamline are set up in such a way that the dispersion of the beamline at the target position matches the dispersion of the spectrometer. Ideally, this results in a minimized θ_{fp} vs. x_{fp} beam-spot in the focal plane, which corresponds to a good lateral and angular resolution. Through application of the matching techniques, an energy resolution of 30 keV and an angular resolution of 0.5° can be achieved for 200 MeV protons under faint-beam conditions.

2.3.3 The Faint-Beam Method

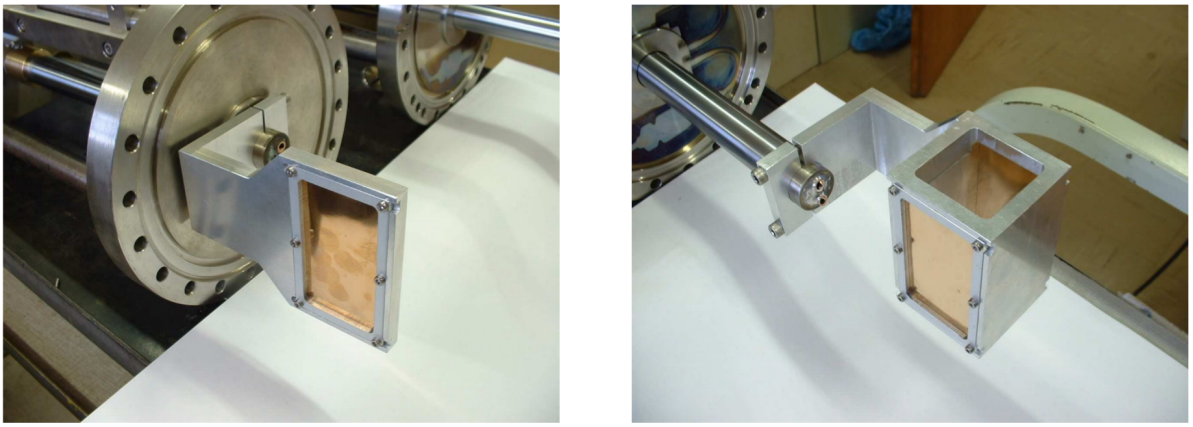

Figure 2.7: Photos of the two attenuators used at iThemba LABS. From [71].

To achieve the matching conditions at $K = 0$ (0° scattering), the image of the beam in the focal plane has to be analyzed. The best way to do this is through the spectrometer and the detector system itself. However, common beam-intensities are too high to allow the direct measurement of the beam since even a 1 nA intensity beam can damage the detector system. At RCNP [72], a method was developed to reduce the beam intensity to about 10^3 particles per second, without changing the emittance and the momentum

spread of the beam. By placing attenuation meshes made of special perforated copper after the ion source, the beam intensity can be reduced without changing its spacial properties. At iThemba LABS, two attenuators [see Fig. (2.7)] are placed in the Q-line which guides the beam from the ECR ion source to SPC2 [see Fig. (2.1)]. The first mesh reduces the beam intensity by 1/100'th of its initial intensity. In addition, the second attenuator, which is composed of a 1/10'th and a 1/1000'th mesh, is installed right behind the first one. Both attenuators can be rotated in such a way that either both, only one, or none are placed inside the trajectory of the beam. Combining both attenuators, a collective reduction of $1/10^6$'th of the initial beam intensity can be achieved.

2.4 Overfocus Mode[8]

Gamow-Teller and Spin-$M1$ transitions are mediated by the $\Delta L = 0$ $\sigma\tau$ operator [see Sec. (1.2) and (1.3)]. In a reaction with a small angular-momentum transfer, the outgoing particles are expected to mainly have small scattering angles around 0° (i.e. they are strongly forward-angle peaked). In order to distinguish states excited by $\Delta L = 0$ transitions from transitions with higher multipolarity, a good angular resolution as well as a large acceptance in the vertical direction is needed. A large acceptance in the vertical direction is realized by the quadrupole magnet Q. The quadrupole creates a small vertical magnification allowing the acceptance of a large scattering angle [57, 59]. To also achieve a good resolution of the vertical scattering-angle we consider the image of a particle ray in the focal plane [60]. In terms of the elements of the transfer matrix, introduced in Sec. (2.3), the vertical position of a particle at the focal plane y_{fp} can be expressed using ion-optical properties of the outgoing particle from the target [73]:

$$\begin{aligned} y_{\mathrm{fp}} = {} & (y|y)y_{\mathrm{tgt}} + (y|\phi)\phi_{\mathrm{tgt}} + (y|yx)y_{\mathrm{tgt}}x_{\mathrm{tgt}} \\ & + (y|y\theta)y_{\mathrm{tgt}}\theta_{\mathrm{tgt}} + (y|y\delta)y_{\mathrm{tgt}}\delta \\ & + (y|\theta x)\theta_{\mathrm{tgt}}x_{\mathrm{tgt}} + (y|\phi\theta)\phi_{\mathrm{tgt}}\theta_{\mathrm{tgt}} \\ & + (y|\theta\delta)\theta_{\mathrm{tgt}}\delta + \text{higher order terms.} \end{aligned} \tag{2.8}$$

In this notation, the label 'tgt' is the identifier for the target position. Generally, the $K600$ is operated in the *focused mode*, illustrated in Fig. (2.8) (a). In this mode, the spectrometer is designed to have $(y|\phi) = 0$ for the central ray. By adjusting the

[8] This section was adopted from [22] and modified to match the $K600$ sepctrometer.

strength of the Q magnet, the $K600$ spectrometer can be operated in an *over-focus mode* ($(y|\phi) > 0$) and also in an *under-focus mode* ($(y|\phi) < 0$). They are illustrated in Figs. (2.8) (b) and (c), respectively, where the *over-focus* and *under-focus mode* together are called *off-focus mode*. As we see in Fig. (2.8) (a), particles scattered in different ϕ directions converge and make a small image in the y direction. On the other hand, in both of the off-focus modes the particles scattered with large scattering angles are coming to different positions in the y direction.

Therefore, the scattering angle ϕ of a particle at the target position (ϕ_{tgt}) can be determined by the measurement of the y position at the focal-plane detector (y_{fp}). It should be noted that an accurate ϕ_{tgt} value can be deduced from the y_{fp} value only if the $(y|\phi)\phi_{\mathrm{tgt}}$ value is larger than the value of $(y|y)y_{\mathrm{tgt}}$ value. Therefore, the strength of the Q magnet should be adjusted correctly in order to realize an appropriate condition.

The matching techniques discussed in Sec. (2.3) have to be applied *after* the *off-focused mode* is established. A detailed and comprehensive description of the adjustment of the Q quadrupole is given in [71].

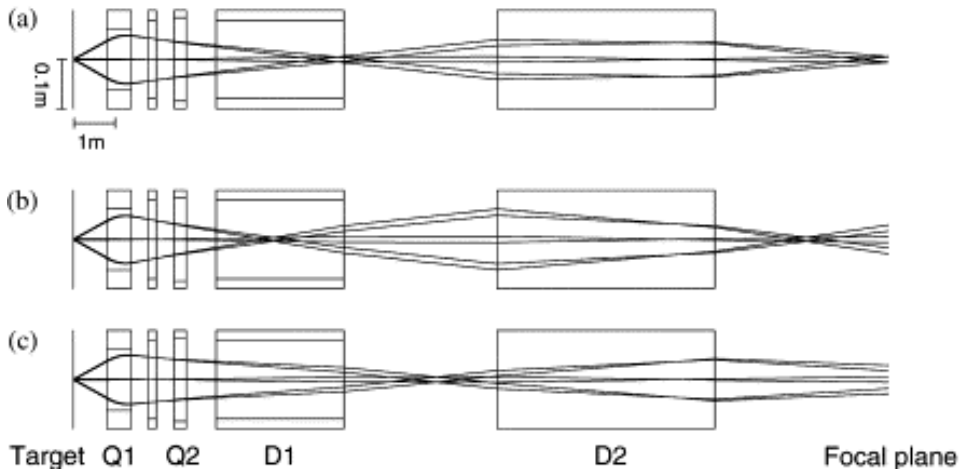

Figure 2.8: Schematic ion-beam trajectories under different focus-conditions.
(a) In *focus mode*.
(b) In *over-focus mode*.
(c) In *under-focus mode*.
Adopted from [60].

2.5 Pepper-Pot Technique

Owing to the $\Delta L = 0$ property of the $\sigma\tau$ operator, the Spin-$M1$ transitions are strongly forward-peaked. For that reason, the cross section of Spin-$M1$ transitions is strongest

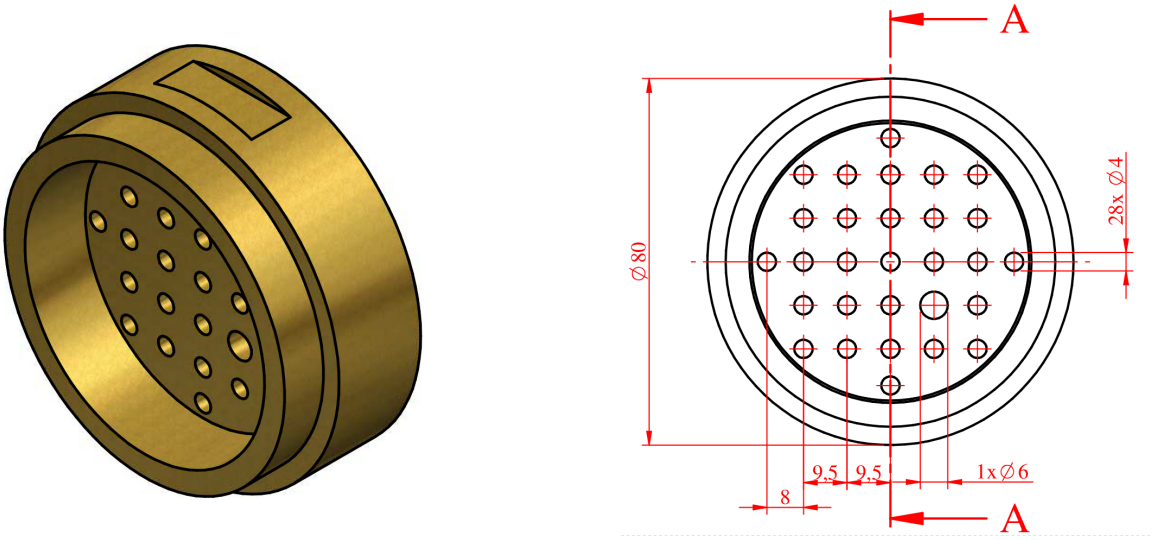

Figure 2.9: Technical drawing of the Pepper Pot collimator. From [71].

at small scattering angles, including 0°. The angular distribution of transitions with higher-order angular-momentum transfer (such as $E1$ or $E2$), however, behaves very differently as a function of the scattering angle. We can, therefore, distinguish the states excited by the Spin-$M1$ transitions from other states by the angular distribution of their cross section. In order to do that, it is crucial to determine the scattering angle of the scattered protons at the target position.

As was described above, a cluster of two MWDCs is installed at the focal-plane position of the $K600$. With the MWDCs, the inclination of the beam in the focal plane, which is proportional to the scattering angle at the target position, can be measured. In order to calibrate the initial scattering angle as a function of the beam-ray inclination at the focal plane, a multi-hole aperture called the 'Pepper Pot'[9] is placed 862 mm downstream from the target. Figure (2.9) shows a technical drawing of the Pepper Pot. The configuration of the Pepper Pot is a 5×5 matrix of holes each with a diameter of 4 mm and spaced 9.5 mm apart. In addition, four holes are located at positions outside of the matrix edges. In contrast to the matrix holes, these holes are only separated from the hole matrix by 8 mm. When installed, the outer holes of the Pepper Pot correspond to $\Theta = \pm 1.79°$ and the inner holes of the central axis to $\pm 1.26°$, $\pm 0.63°$ and 0°, respectively.

The Pepper-Pot calibration runs are usually performed at the beginning of a $K < 0$ ($\Theta > 0°$) measurement. It should be noted that the Pepper-Pot technique is not applicable to inelastic-scattering reactions at $K = 0$. The reason for this is discussed at

[9]Named after its resemblance to the top of a pepper pot (pepper shaker)

the end of this section. After dispersion-matching conditions are achieved, the Pepper-Pot collimator is installed. In addition, a thick gold foil is mounted in the target ladder and moved inside the beam trajectory. After being elastically scattered from the gold target, the protons are collimated by the Pepper Pot. As a result, potato-shaped spots corresponding to the collimator holes are observed in the Θ_{fp} vs. X_{fp} spectrum. Using the geometry of the Pepper Pot, these spots can be related to the scattering angle at the target position. It should be noted that, owing to variations in the $K600$ field, the calibration of the scattering angle changes as a function of the focal-plane position. Thus, several runs with different $K600$ field-settings are performed. In addition, it is noteworthy that the vertical scattering-angle (ϕ_{fp}) is relatively flat; hence, it is not necessary to recalibrate (ϕ_{fp}) for each experiment.

As stated above, the Pepper-Pot technique cannot be applied in the 0° mode of the $K600$. At 0°, the incoming beam passes through the spectrometer along with the scattered particles. Because the protons elastically scattered from the gold are used, and because these scattered protons have the same magnetic rigidity as the beam protons, they hit the focal plane at the same position. This is impractical because even a beam with an intensity of 1 nA can damage the detector system. It has been suggested to apply the faint-beam method to 0° Pepper-Pot measurements, which would technically solve this problem; however, the background caused by the beam particles might be too high to resolve the signals of the elastically-scattered particles. Suggestions of a modified Pepper Pot that simultaneously works as a beam stop for the unscattered particles have also been made. When dispersion matching is realized, however, the beam is defocused on the target resulting in a wide beamspot. Because there are no ion-optical elements between the target and the Pepper Pot, this also results in a wide beam spot on the collimator. For that reason, the beamstop would have to take up a large fraction of the Pepper Pot rendering its calibration features useless. In addition, background from beam particles scattering at the slits would overwhelm the events caused by elastic scattering.

2.6 Collimator-Related Background

In a real experiment, only a small fraction of the initial beam particles interact with the target nuclei through the desired inelastic-scattering mechanism. A much larger amount is scattered elastically from the target material. When these particles hit the hardware inside the $K600$, they can contribute a large background to the detector signals [41].

In order to reduce this effect, a brass collimator is installed at the entrance slit of the $K600$. The purpose of this collimator is the reduction of the background, however, it also introduces a new source for secondary scattering. This situation is illustrated in Fig. (2.10) (a). In order to suppress this effect, a tapered lip was added to the collimator. Beam particles that undergo secondary scattering at the collimator or are outside the allowed acceptance have to pass the lip material [see Fig. (2.10) (b)]. Because of the energy loss inside the lip, the particles are swept outside the detector systems acceptance, even if they undergo secondary scattering inside the $K600$. As a result, the background of secondary-scattered beam-particles is significantly reduced.

During the experiment presented in this work, a new collimator with an elongated lip was used. As is shown in the part (c) of Fig. (2.10), beam particles that experienced secondary scattering inside the collimator were successfully removed from the detector systems acceptance. However, because the collimator neck did not have enough material, elastically-scattered particles with scattering angles larger than the desired $K600$ acceptance were not sufficiently slowed down. These particles were scattered inside the $K600$ and contributed a background to our data, similar to the situation when no collimator is used. Similar effects have been observed in [26]. The influence of this background on our data is discussed in detail in Sec. (4.7.1).

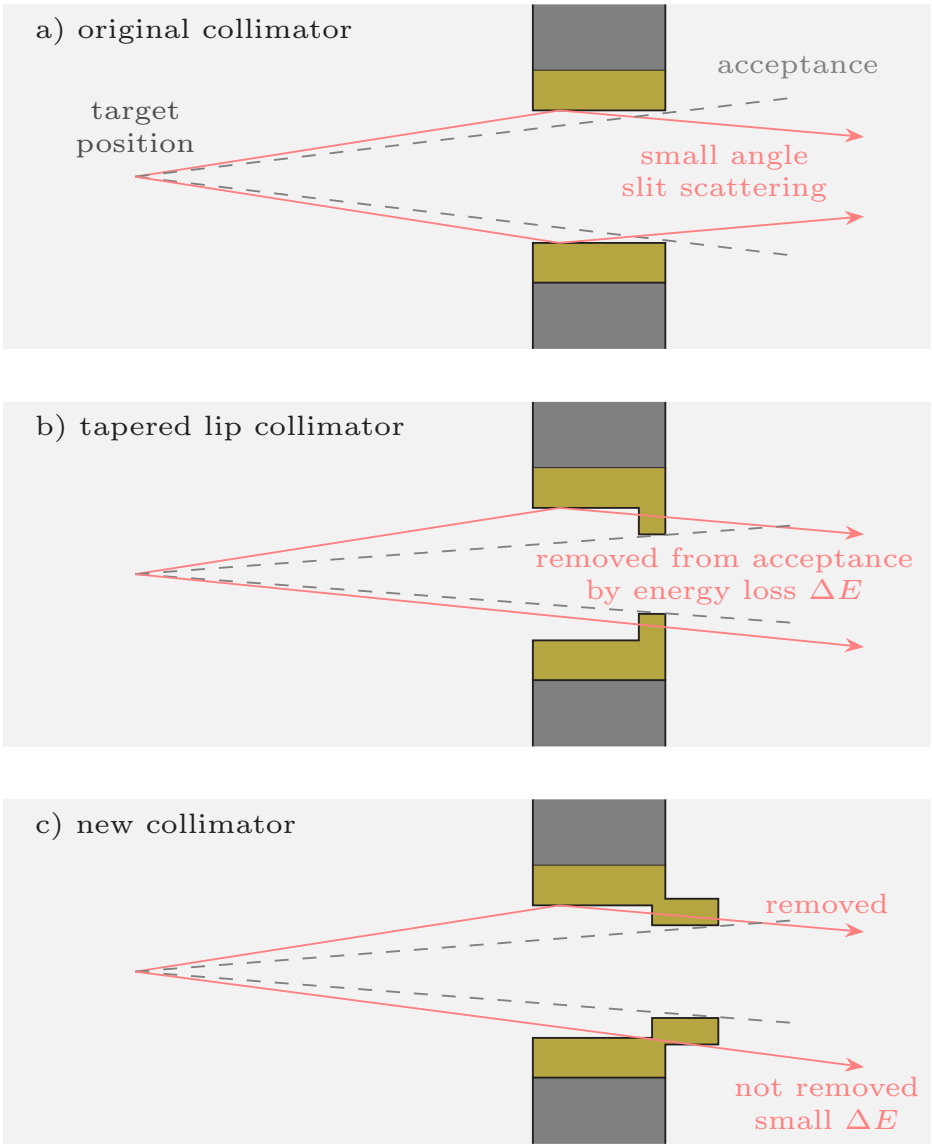

Figure 2.10: Schematic drawing of the spectrometer collimators (brass) used at iThemba LABS. The beam particle that should be removed by the collimators are illustrated by the red lines. The acceptance of the spectrometer is shown by the dashed gray lines. Modified from [26]

3 Experiment Report

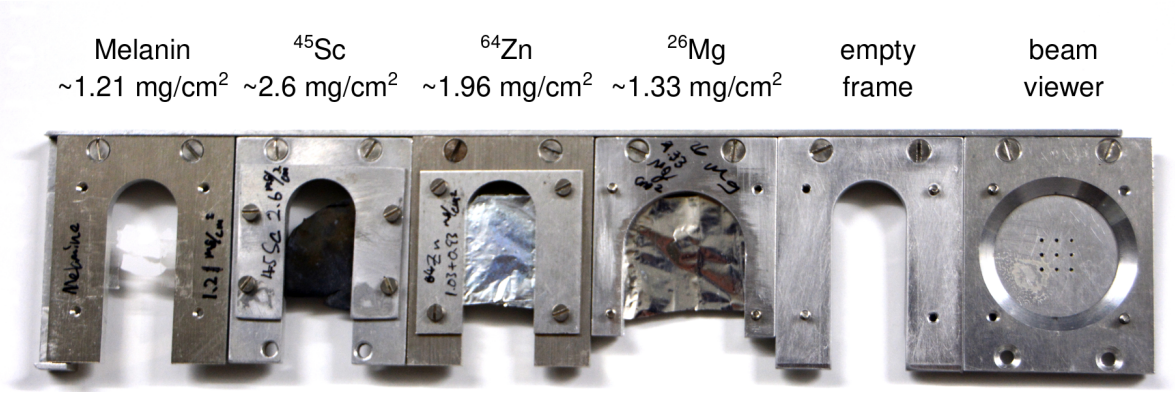

Figure 3.1: Target ladder mounted with the targets used in the first measurement weekend at 0°.

The ^{64}Zn(p,p')^{64}Zn reaction experiment was performed in February of 2017 at iThemba LABS in Cape Town, South Africa. During the week, the main operative of the iThemba LABS facility is treatment of cancer patients through proton and neutron therapy as well as the production of medical radioisotopes. The measurements motivated by nuclear structure interests are, therefore, limited to the weekends, including Thursdays and Fridays. We performed our measurements on four consecutive weekends in February and March 2017. On the first two weekends, we operated the $K600$ spectrometer in the 0° mode and we switched to the 4° mode for the remaining weekends. The initial design of the experiment also included measurements using the 7° facility of the $K600$ spectrometer. However, owing to complications with the high voltage supply of the ion source and the injector cyclotron (SPC2) we were not able to perform these measurements.

In order to achieve the high resolution of 35 keV, we applied dispersion matching to the spectrometer system on each of the experiment weekends. In the beginning of the 3rd weekend, we also performed measurements using a multi-hole slit aperture and a gold target. This allowed the calibration of the scattering angle at the target position in the offline analysis. Figure (3.1) shows a typical arrangement of the targets

in the target ladder on one of the weekends. With exception of the Melamine target[1], which was held in place by a thin plastic film, all targets were made of self-supporting foils. The low momentum side of the target frames was removed to reduce secondary scattering of beam particles [41]. The target of major interest, ^{64}Zn, is located on position 3 from the left. During the experiment, we repeated a routine of 1h long measurements with ^{64}Zn at the target position, followed by a $\frac{1}{2}$h run with the ^{26}Mg target, and a 5 minute *beam-halo* run with the empty target frame. ^{26}Mg has many well-known states and is, therefore, well suited to track position shifts to correct angular aberrations and to calibrate excitation energies. The empty target runs were used to check for increased beam halo contributions. We also performed a few runs bombarding the Melamine and the ^{45}Sc target. Melamine ($C_3H_6N_6$) is composed of Carbon, Hydrogen, and Nitrogen and, therefore, also serves as an additional source for shift tracking and energy calibration.

Although the cross section of the ^{64}Zn(p,p')^{64}Zn reaction was lower than expected, we achieved sufficient statistics to be able to analyze the data. We have to stress, however, that the analysis of the angular distribution of states suffers from the loss of the 7° measurements.

[1]The Melamine target was produced by H. Fujita by evaporating a commercial melanin cleaning sponge onto a glass plate.

4 Offline Raw-Data Analysis

The goal of the offline analysis is to translate the signals from the detector system (raw data) to high-resolution spectra from which eventually information about nuclear excitations can be obtained. In the following chapter, we will outline the essential parts of the offline analysis, starting from the very raw detector signals to an energy-calibrated high-resolution spectrum with minimal background. Here, we describe the systematic workflow of the analysis. We wish to stress that in reality the procedure is not always as streamlined as it appears from the following description.

4.1 Drift-Chamber Signal Calibration

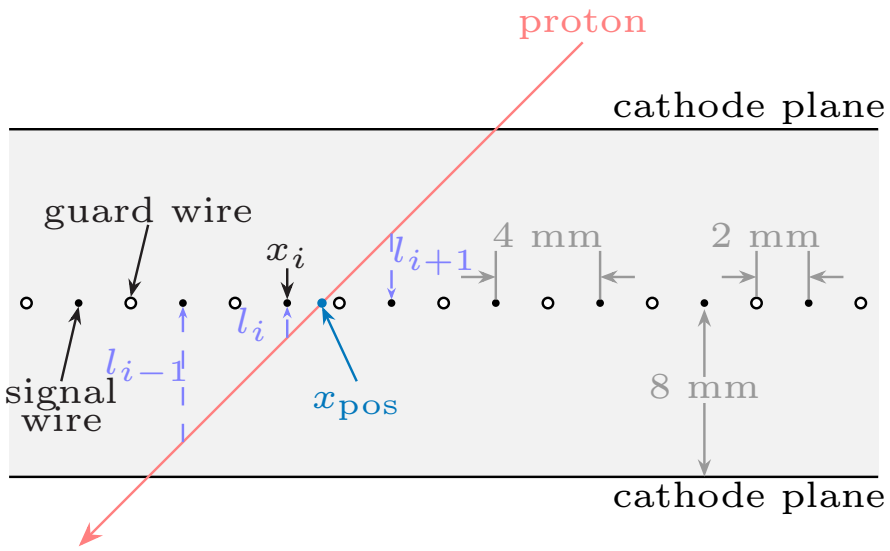

Figure 4.1: Schematic drawing of a beam particle passing the MWDC at iThemba LABS. A detailed description of the MWDC is given in Sec. (2.2.2). Modified from [74].

When a particle passes the MWDC, it creates electron-ion pairs along its path. The electrons drift to the signal wires and create the MWDC signals when they reach the

wires. From the relative timing information of these signals, the distance of the proton ray from the signal wire can be determined. Figure (4.1) shows a schematic drawing of this process. The drift length of the electrons to the signal wires x_i is labeled l_i. From a linear fit of the $x_i(l_i)$ dependence, the real position of the proton in the focal plane x_{pos} can be calculated.

4.1.1 Timing-Offset Correction

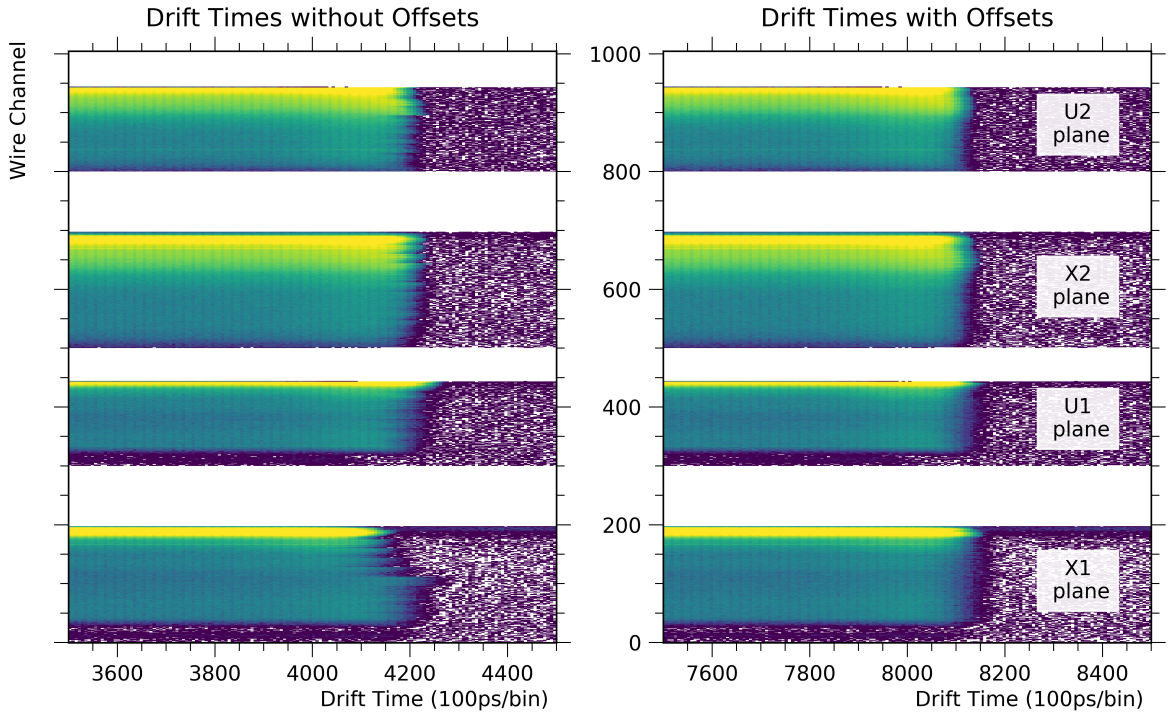

Figure 4.2: Initial and corrected drift times for each wire in wire chamber 1 and 2 in the x and u wire plane.

The relative time between coincident signals of neighboring wires is measured by Time-to-Digital converters (TDCs). There are several factors that influence the arrival time of the signals at the TDCs, such as the difference in length of cables connecting the MWDCs and the TDCs, and different response characteristics of the preamplifier channels [71]. As a result, the drift time of each wire can be artificially shifted. Owing to the high sensitivity of the analyzer system, shifts of the order of a few nanoseconds (ns) are observable. The unshifted drift-time spectra of each individual wire are shown in the left part of Fig. (4.2) Eventually, drift-time offsets between neighboring wires can introduce uncertainties in the focal-plane position of the particles and for that reason it is crucial

to shift all wires to a common value. This is shown in the right part of Fig. (4.2) where all spectra are shifted to a common drift-time offset of 820 ns.

4.1.2 Drift-Length Calibration

In principle, the drift-time distributions of all wires in each wire plane should be similar when the whole MWDC is uniformly illuminated. For the calculation of the drift length l, it is therefore sufficient to observe the characteristic drift-time distribution of each wire plane. The characteristic distributions of each wire plane are obtained by accumulating the signals of all wires in the respective plane. The distributions are shown in Fig. (4.3). It should be noted that Fig. (4.2) shows a situation where the wires on one side of each wire plane are more strongly illuminated than others. The wires with increased statistics can contribute distortions to the drift-time distribution and, therefore, have to be excluded from the drift-time analysis. From the drift-time distribution ($\frac{dN}{dt}$), we can

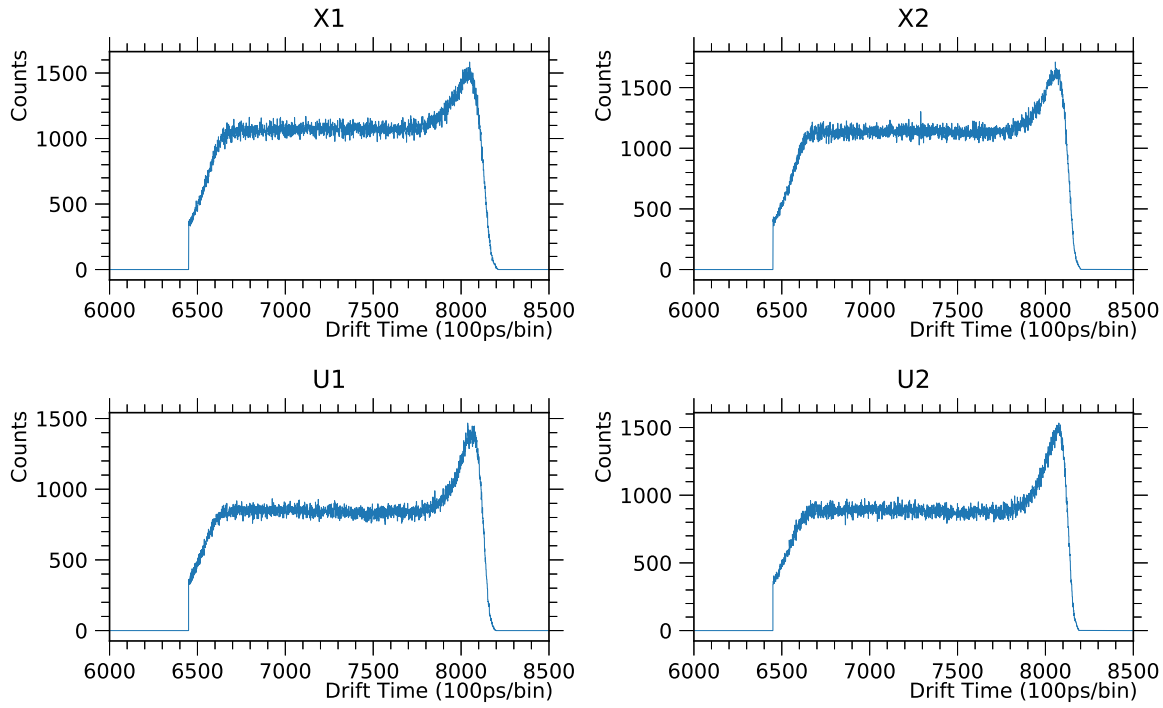

Figure 4.3: Clean drift-time spectra for all wire planes.

calculate the drift length l of the particle ray from each wire in the wire plane via:

$$l(t) = \left(\frac{dN}{dl}\right)^{-1} \int_{t_0}^{t} \left(\frac{dN}{dt'}\right) dt', \tag{4.1}$$

where t_0 is the reference time and t is the time of the signal-wire signal [71, 75]. When the MWDC is uniformly illuminated, the drift-length distribution $\frac{dN}{dl}$ is constant and thus:

$$l(t) \propto \int_{t_0}^{t} \left(\frac{dN}{dt'}\right) dt'. \tag{4.2}$$

We use normalized look-up tables (LUTs) to correlate the drift-time signal to the drift length l. The distributions of the LUTs of each wire plane are shown in Fig. (4.4). In the

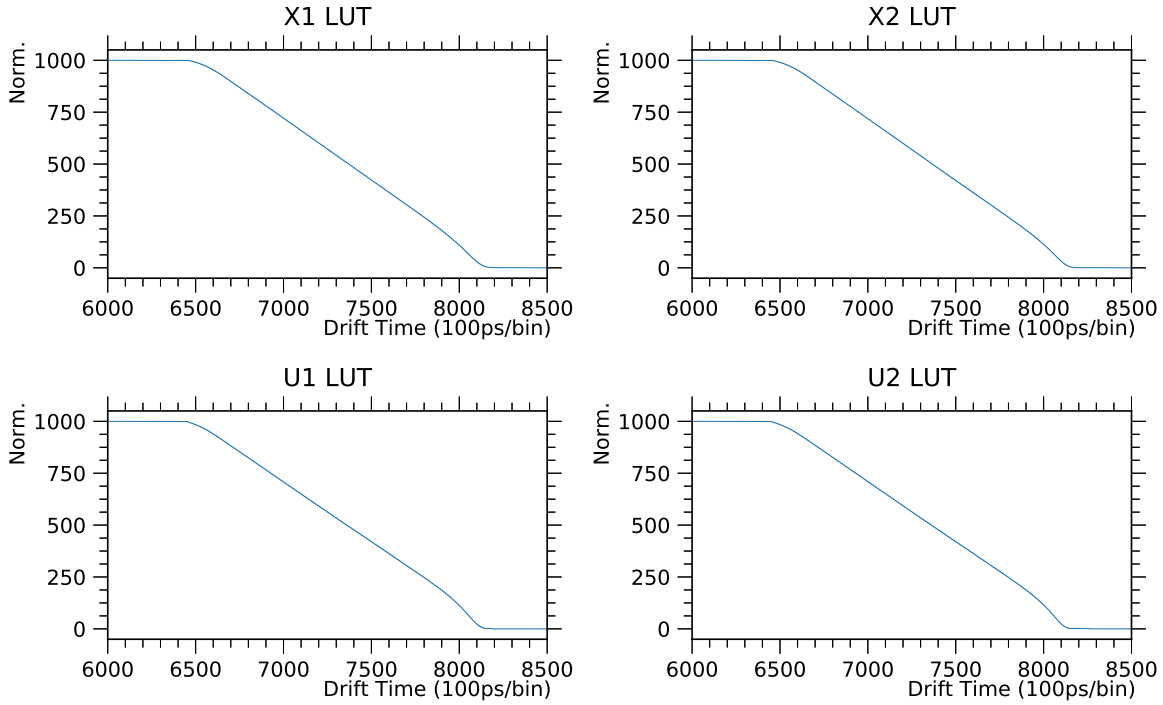

Figure 4.4: Lookup tables for all wire planes.

subsequent analysis, the drift length can then be calculated from looking up the value of l for each measured drift time and multiplying it with the maximum drift length, which is the distance of the wire to the anode plane, i.e., 8 mm. If the LUTs are correct, the distribution of l should be flat. This condition is shown in Fig. (4.5). However, when the electrons are created in the close vicinity of the wires, and as such, have very short drift times, the non-linearity of the electric field of the respective wire can cause ambiguities of the calculated drift length. We can examine the influence of this effect by comparing the calculated drift length with an estimated drift length for events with short drift times. The correlation of these values are compared in the so-called resolution (Res2d) shown in Fig. (4.6). If these plots show a straight distribution, the quality of the LUTs

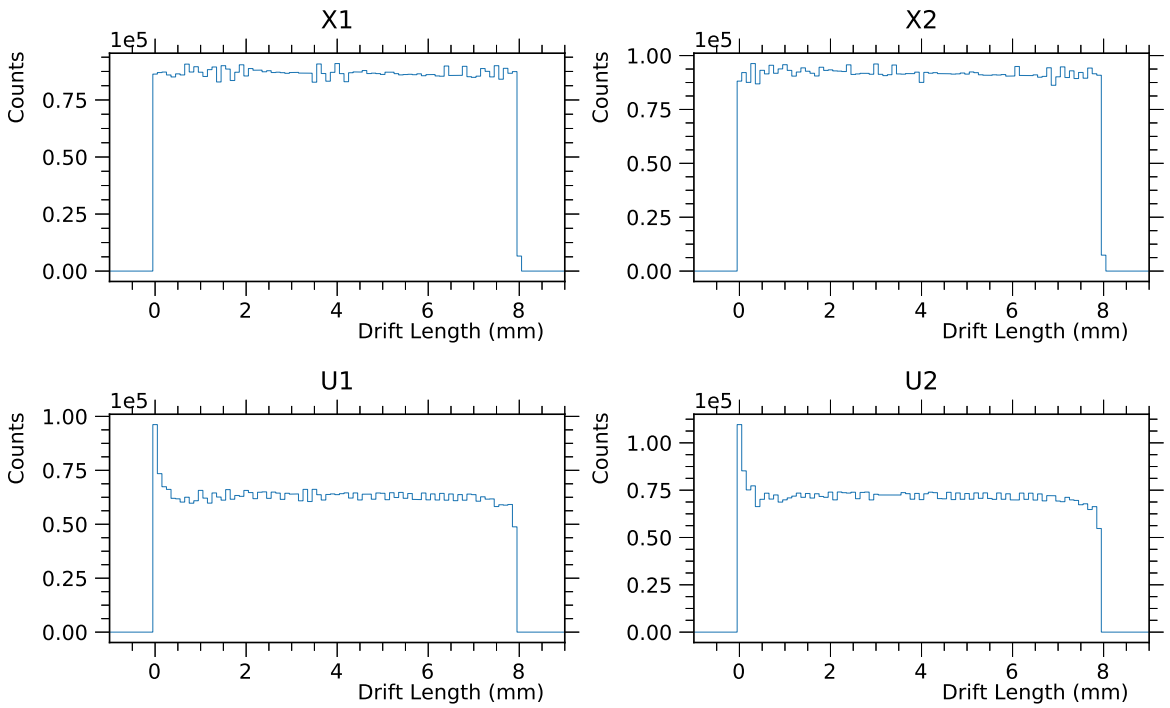

Figure 4.5: Flat drift-length spectra for all wire planes. The spike on the left hand side of each spectrum is caused by non-linearities of the electric field of the anode wires. These signals are rejected by the analyzer software.

is reasonably good. In some cases however, it is necessary to apply additional offsets to the LUTs. Finally, if a correct drift time to drift length conversion is ensured, the particle position in the focal plane of each wire chamber is calculated from a fit of the coincident drift-length signals. It should be noted that *lazy* wires as well coincidence of close-lying particle rays (W and Z signals) can cause errors in the estimation of the ray position in the focal plane. These events can be corrected by the analyzer software.

4.2 MWDC Detection Efficiency

To obtain reliable data across the full focal plane, we have to monitor the detection efficiency across the MWDC. In addition, it is desired to achieve maximum efficiency for all MWDCs to obtain maximum statistics. The efficiency inside the MWDCs is largely influenced by the gas quality and also the functioning of the TDC-cards. We write the total efficiency as the product of the geometric efficiency ϵ_g and the intrinsic efficiency ϵ_i [71, 76].

$$\epsilon = \epsilon_g \cdot \epsilon_i. \tag{4.3}$$

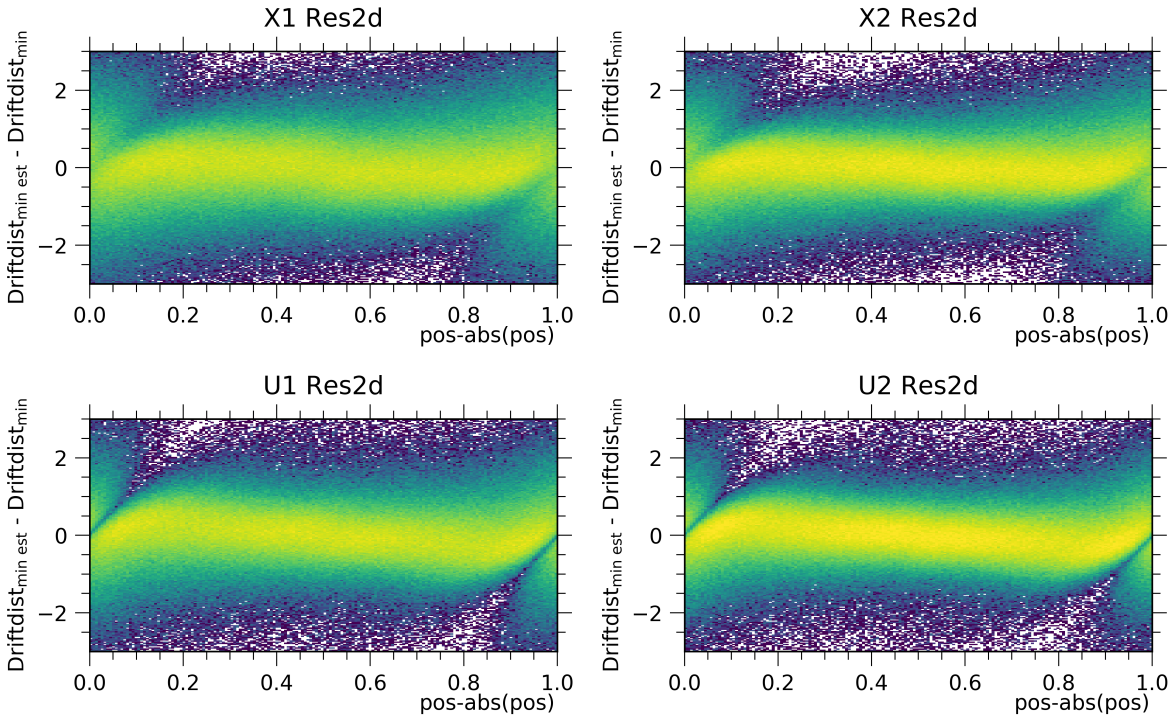

Figure 4.6: Resolution plots for all wire planes.

In our experiment, the particles of a given rigidity were well focused in the vertical direction. As a result, we can assume that the geometric efficiency is 100%, i.e., $\epsilon_g = 1$. The intrinsic efficiency, on the other hand, is the ratio of the number of events N_{accepted} that were accepted by the detector system and the total number of events N_{total}.

$$\epsilon_i = \frac{N_{\text{accepted}}}{N_{total}}. \tag{4.4}$$

At iThemba LABS, events are accepted if they meet the following criteria:

- TOF and scintillator signals fall within the gated regions
- number of hit wires in the MWDC is between 3 and 6
- the reduced chi-squared for position reconstruction is less then 1
- drift times fall into the gated regions

We tracked the detector efficiency for all weekends to maintain a constant and high efficiency during the full experiment time. A typical efficiency distribution for the four wire planes is shown in Fig. (4.7). Throughout the experiment, the detection efficiencies

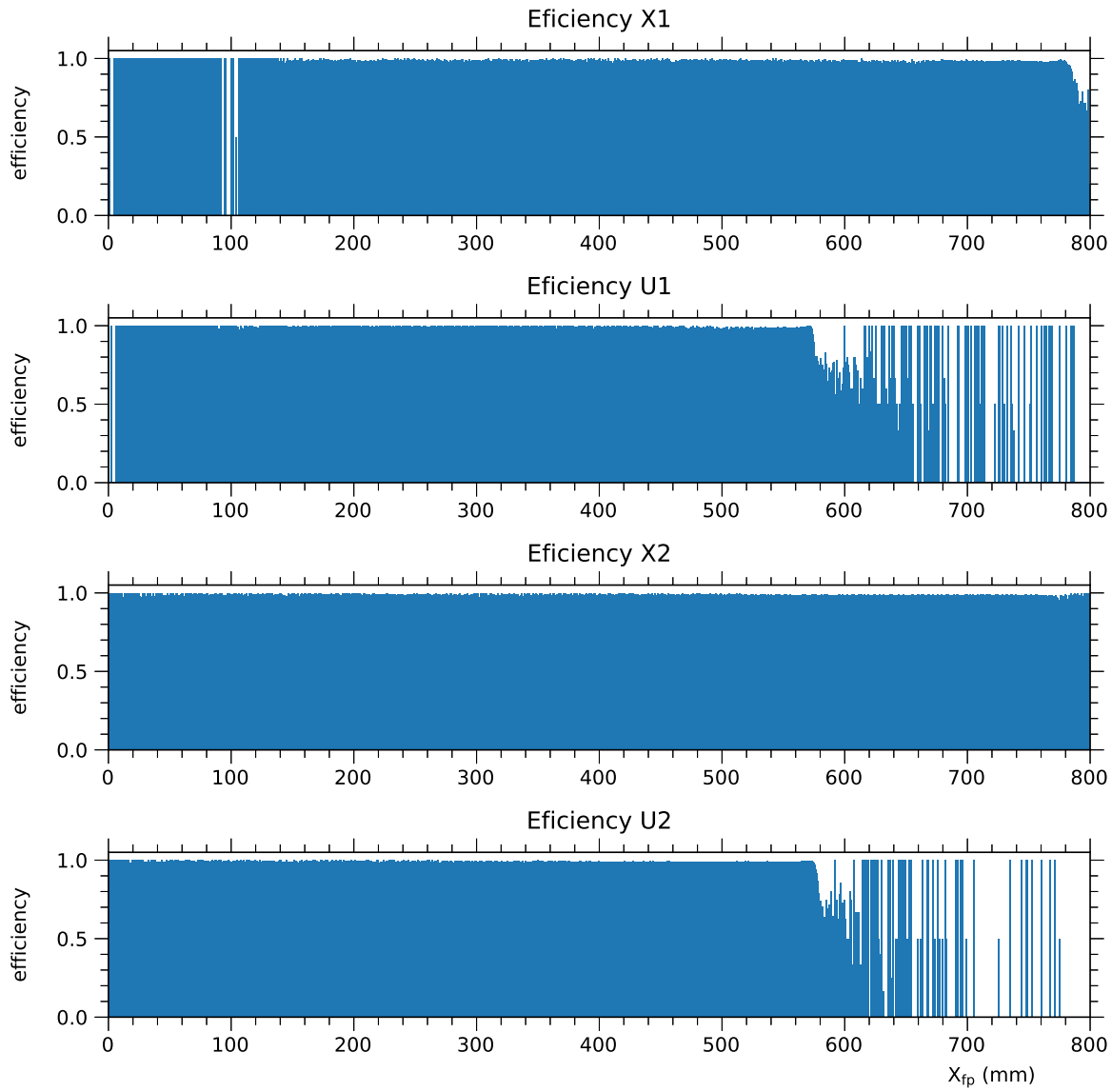

Figure 4.7: Typical intrinsic detection efficiency for all wire planes.

of each wire plane were of the order of 95%. This results in a total detection efficiency of more than 80%.

4.3 Scattering-Angle Reconstruction

By the application of beam-matching techniques, we achieved a high lateral and angular resolution. Both properties are closely connected and limit each other. The angle of the scattered protons in the detector plane can be determined by the slope of the particle

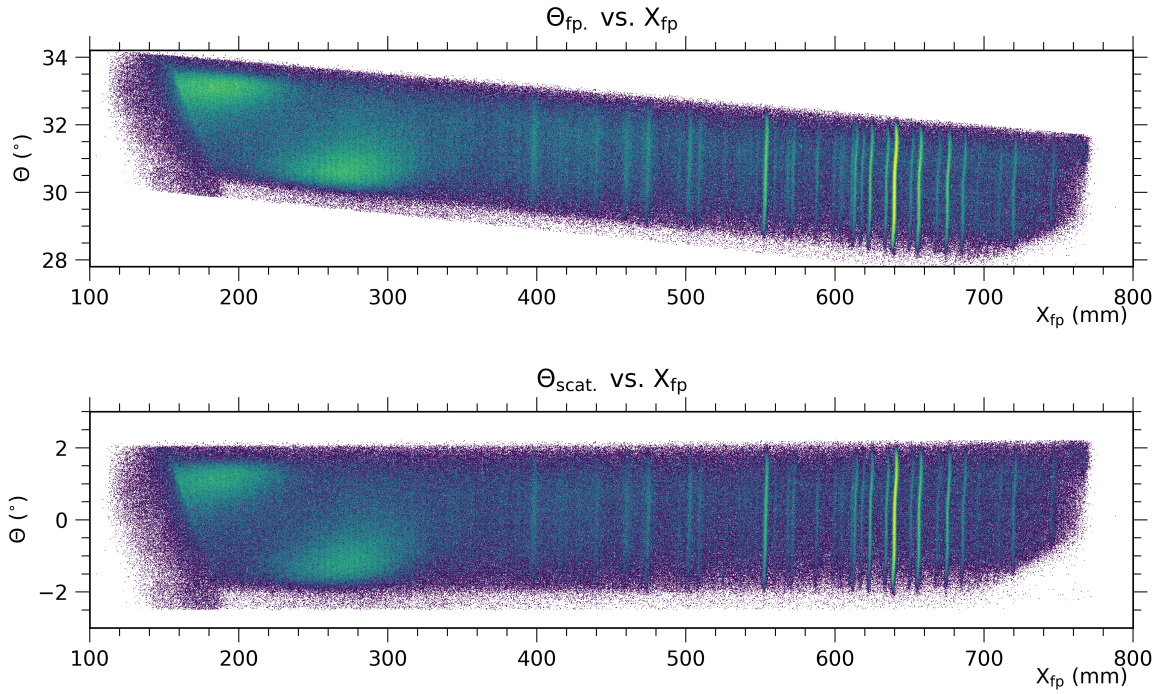

Figure 4.8: Calibration of the scattering angle at 0°. Top: The scattering angle observed by the focal-plane detector system Θ_{fp}. Bottom: Calibrated scattering angle at the target position Θ_{scat}.

ray in two wire chambers. During the experiment we did not aim to achieve angular dispersion-matching, however, the achieved angular resolution was sufficient to perform a calibration of the horizontal scattering angle. The aim of the calibration is to connect the scattering angle, which was measured at the focal-plane position (Θ_{fp}), to the scattering angle at the target position (Θ_{scat}). Therefore, the parameters a_{slope}, a_{offset}, b_{slope} and b_{offset}, which are used in the calibration function Eq. (4.5), have to be determined.

$$\Theta_{\mathrm{scat}} = (a_{\mathrm{slope}}\mathrm{X}_{\mathrm{fp}} + a_{\mathrm{offset}})\Theta_{\mathrm{fp}} + (b_{\mathrm{slope}}\mathrm{X}_{\mathrm{fp}} + b_{\mathrm{offset}}) \tag{4.5}$$

In the next two sections, the reconstruction procedure is described in more detail.

4.3.1 0° Measurements

When the *K*600 spectrometer is operated in the 0° mode, the Pepper-Pot technique cannot be applied [see Sec. (2.5)]. In this case, it is not possible to divide the data into smaller angle bins. However, the calibration ensures that the scattering angles are centered within the acceptance of the spectrometer, which is [-2°,+2°]. We picked points

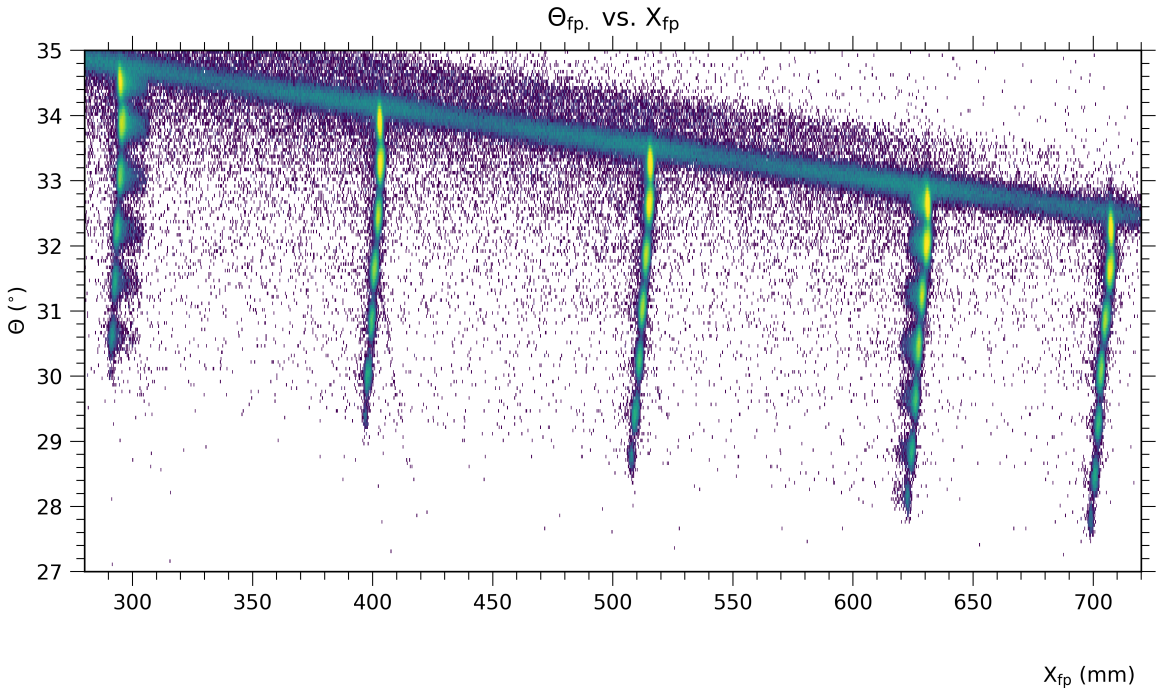

Figure 4.9: Each vertical line of *potatoes* corresponds to one D1 setting. D1 settings from left to right: (1) D1 = 465.5, (2) D1 = 460.5, (3) D1 = 455.5, (4) D1 = 450.5, (5) D1 = 447.5.

at the edge of the acceptance of the rectangle in the Θ_{fp} vs. X_{fp} histogram. The lower edge of the acceptance corresponds to $\Theta_{\mathrm{scat}} = -2°$, while the upper edge corresponds to $\Theta_{\mathrm{scat}} = +2°$. We selected points at both edges and fitted Eq. (4.5) via its parameters to these points. This technique was performed for both 0° measurement weekends separately. Fig. (4.8) shows the results for weekend 1. The calibration parameters for both weekends are listed in Tab. (4.1).

4.3.2 4° Measurements

In order to study the angular distribution of states observed in the 0° spectrum and to resolve states with small excitation energies ($>$ 2.0MeV), the $K600$ spectrometer was operated in the 4° mode during weekend 3 and 4. For the calibration of Θ_{fp}, 5 runs using a gold target and the Pepper-Pot collimator were performed at the beginning of the third weekend. The $K600$ was operated in the +3% over-focus mode to achieve good separation in the Y_{fp} direction. The Pepper Pot was installed 862.11 mm downstream of the target. A technical drawing of the collimator is shown in Fig. (2.9). The magnetic field of the first dipole magnet (D1) in the $K600$ was changed for each cali-

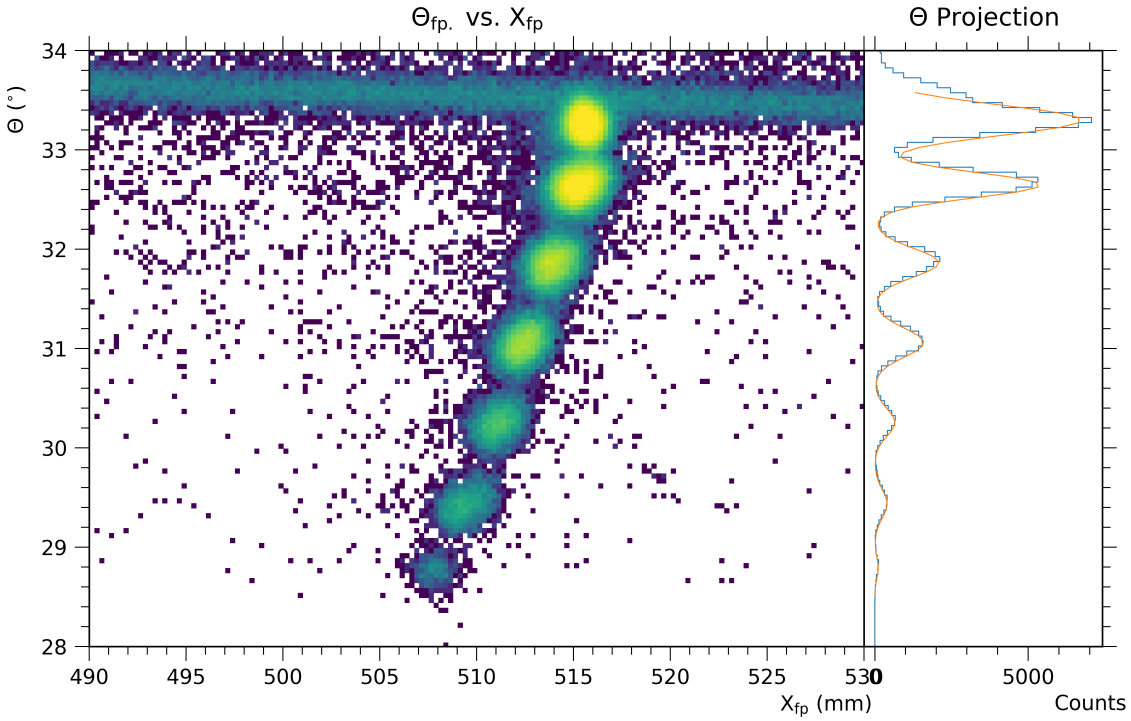

Figure 4.10: Detailed view of the *potatoes* corresponding to one D1 setting. On the right hand side, the projection of the potatoes to the Θ axis is shown. The Gaussian functions fitted to the projections are illustrated by the orange line.

bration run. For each D1 setting, the elastically scattered protons hit the focal plane at different X_{fp} positions, allowing a calibration of Θ_{scat} across the entire focal plane. An accumulated Θ_{scat} vs X_{fp} histogram of all five calibration runs is shown in Fig. (4.9).

For each D1 setting, the vertical line of *potatoes* is projected to the Θ_{fp} axis, resulting in a Gaussian-like peak for each *potato*. By fitting the peaks, the corresponding Θ_{fp} values of each *potato* can be determined. An example for this procedure is shown in Fig. (4.10). From the geometry of the Pepper-Pot setup, the corresponding Θ_{scat} value can be derived. As shown in Fig. (4.11) (a) - (e), the Θ_{fp} values were fitted to the respective Θ_{scat} values for each D1 setting using linear functions. In order to obtain the calibration parameters for Eq. (4.5), the resulting offset and slope parameters were then fitted separately using linear functions. The results of these fits are shown in Fig. (4.12a) and Fig. (4.12b).

The calibration parameters are summarized in Tab. (4.1). It should be noted that below $X_{fp} \approx 400$ mm the acceptance of the $K600$ spectrometer decreased. For that reason, we could not measure scattered protons with $\Theta_{scat} > 5.7°$ in that region.

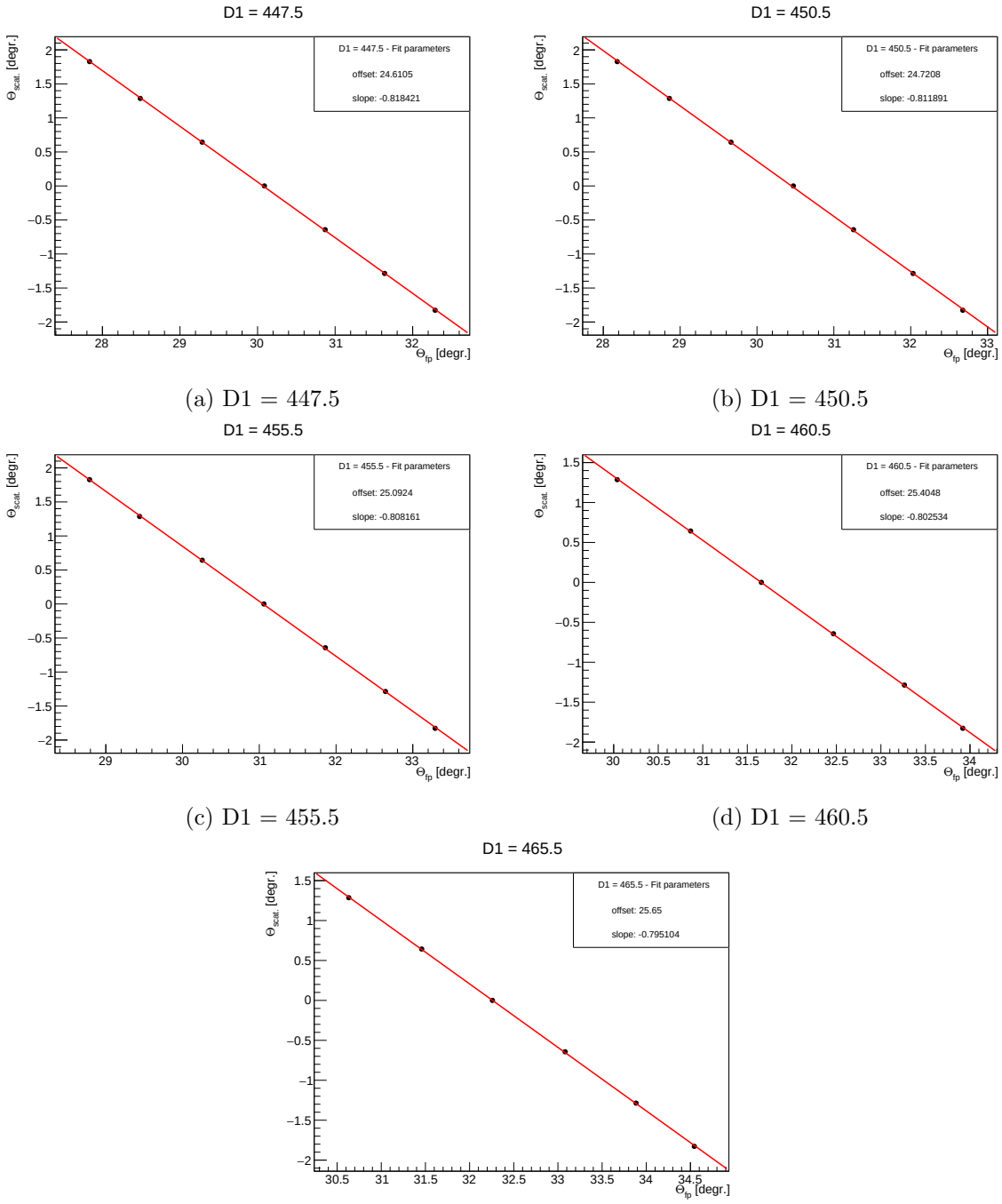

(a) D1 = 447.5

(b) D1 = 450.5

(c) D1 = 455.5

(d) D1 = 460.5

(e) D1 = 465.5

Figure 4.11: Θ_{scat} vs.Θ_{fp} fitting results.

4.4 Particle Identification

In order to obtain clean proton spectra, it is crucial to remove the systematic background from the data. For particle identification, two scintillators, also called *paddels*

Table 4.1: Θ_{scat} calibration parameters for each experiment weekend.

	Weekend 1	Weekend 2	Weekend 3 & 4
a_{slope}	-1.52634e-04	-2.02057e-04	-5.42435e-05
a_{offset}	1.14098	1.16797	-0.77984
b_{slope}	9.36722e-03	10.8047e-03	-2.62210e-03
b_{offset}	-37.4468	-38.2834	26.4301

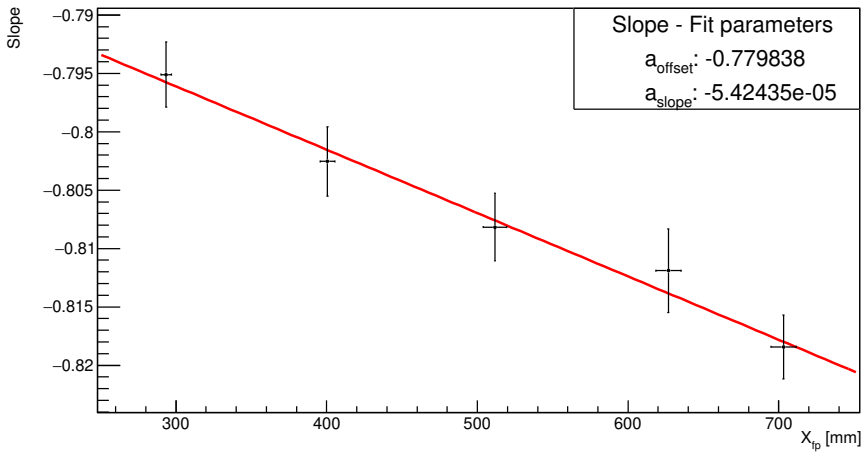

(a) Slope fit.

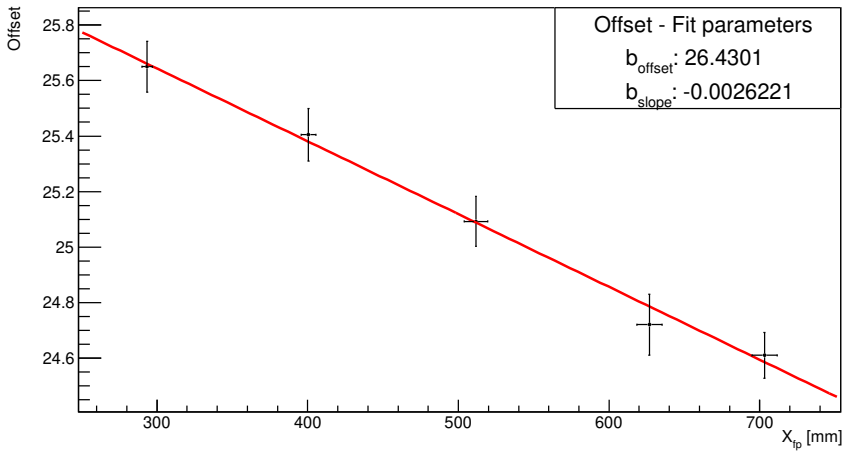

(b) Offset fit.

Figure 4.12: Fit of the slope and offset parameters determined from Fig. (4.11).

at iThemba LABS, were installed downstream the two MWDCs. The paddle signals were used to determine the energy loss (ΔE) of the beam particles inside the paddels

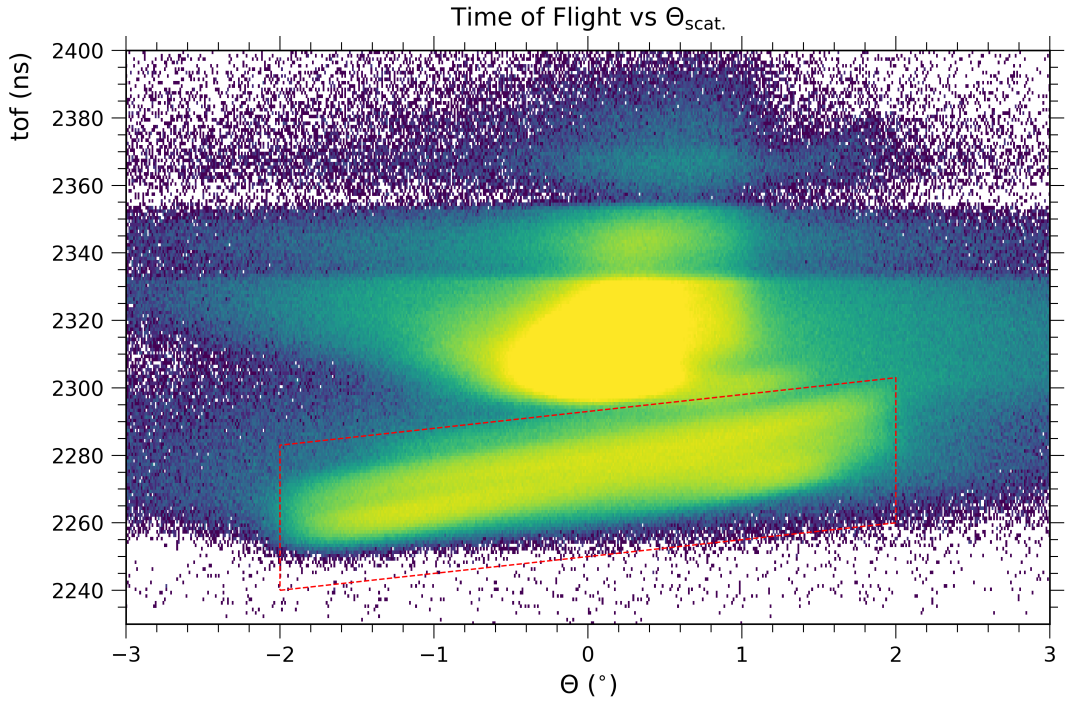

Figure 4.13: PID gate in the TOF vs. $\Theta_{\text{scat.}}$ plane.

(pad) and as stop signals to measure the time-of-flight (TOF) of the beam particles with respect to the SSC frequency. Therefore, the particles of interest can be separated very well from most background events by placing software gates in the $\Delta E_{Pad.1}$ vs. TOF and $\Delta E_{Pad.2}$ vs. TOF plane as well as gates in the TOF vs. X_{fp} plane. Here, we found that an additional software gate in the TOF vs. Θ_{scat} plane is also very effective in removing most of the background events. Figure (4.13) shows the application of the TOF vs. Θ_{scat} plane gate. The effect of the gate onto the position spectrum is shown in Fig. (4.14).

After the particle identification, additional background is still present in the region of interest. A discussion on the subtraction of this background is given in Sec. (4.7).

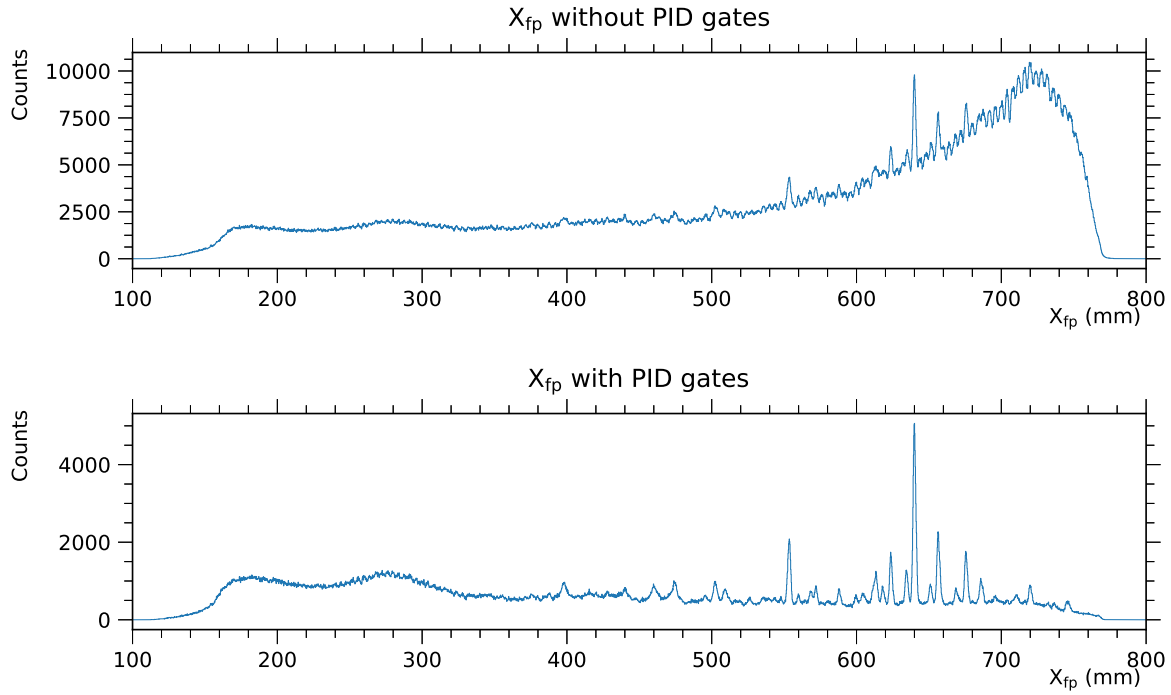

Figure 4.14: Comparison of ^{26}Mg spectra with and without PID gates.

4.5 Correction of the Spectrometer Aberration[1]

The $K600$ spectrometer is a large dipole magnet, which works on charged particles like a prism on white light [see Sec. (2.2.1)]. According to their momentum, the particles are dispersed by the magnetic field of the $K600$. Owing to inhomogeneties of the field inside the spectrometer and target-related recoil effects, higher order aberrations influence the particles' trajectories. For that reason, spectral lines of excited states seen in the focal plane are distorted. The top part of Fig. (4.15) shows the distorted lines in the Θ_{fp} direction. Because the position spectrum is made from a projection of these histograms to the X_{fp} axis, the aberrations have to be removed in order to achieve a high position/energy resolution. This is done by a detailed analysis of the shape of each individual spectral line. By studying the aberration behavior across the focal plane, it's effect on the spectral line shapes can be reduced. A detailed description of the correction of the spectrometers aberration effects is given in App. (8.2). The corrected spectral lines are shown in the bottom part of Fig. (4.15) and the effect of the line-shape correction on the position spectrum is shown in Fig. (4.16). From the projection of the spectral lines in

[1]This section was adopted from [22] and modified to match the present discussion.

Θ_{fp} direction to the position (X_{fp}) axis, high-resolution spectra are produced. Through the correction of the aberration effects, an energy resolution of 35 keV was achieved.

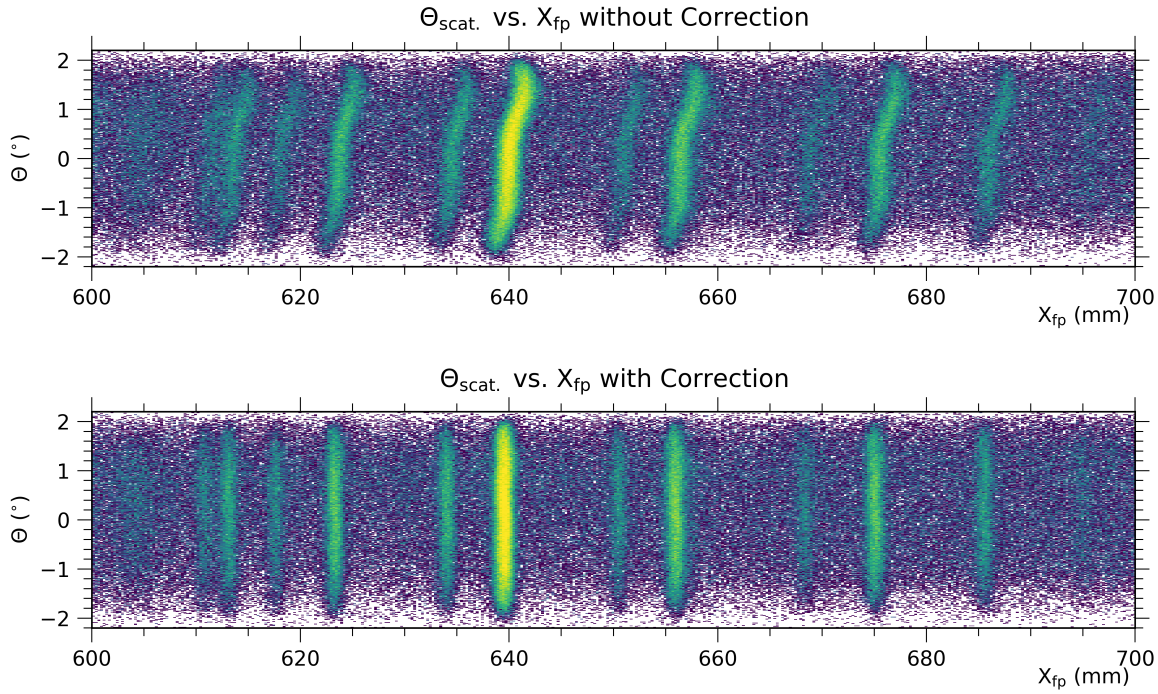

Figure 4.15: Θ_{scat} vs X_{fp} histograms of ^{26}Mg before and after the Θ_{scat} aberration and kinematic recoil corrections were applied.

4.6 Excitation-Energy Calibration

From the MWDCs signals, the position X_{fp} (in mm) of the scattered protons in the focal plane is reconstructed. For the energy calibration, the X_{fp} values of known states are paired with their E_x value from literature. Here, the excitation energies of the states in different nuclei cannot be directly compared because of the different recoil energies caused by the masses of the target nuclei. However, their magnetic rigidity value ($B\rho$), which is equal to the momentum p divided by the particle charge q_c, can be calculated for every state and nucleus using two-body kinematics. Through $B\rho$ values it is possible to combine states from different targets in one calibration.

$$B\rho = \frac{p}{q_c} \tag{4.6}$$

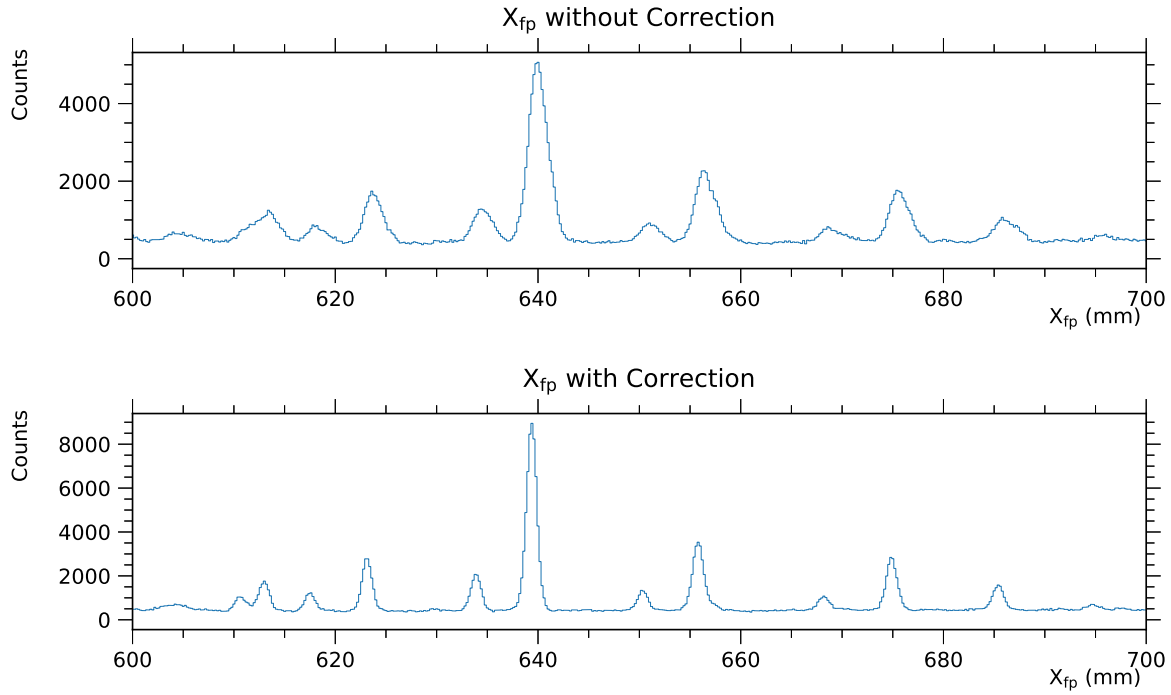

Figure 4.16: Position spectrum of ^{26}Mg before and after the Θ_{scat} aberration and kinematic recoil corrections were applied.

In Eq. (4.6), B represents the magnetic field strength of the $K600$ spectrometer and r describes the mean orbit of the protons [22].

The energy calibration is divided into two separate processes:

1. A calibration function (2^{nd} order polynomial) that connects the focal-plane position $\mathrm{X_{fp}}$ to the magnetic rigidity ($B\rho$), and

2. a kinematics calculation that connects the $B\rho$ values to the excitation energy.

In order to obtain the parameters of the calibration function, we fitted the position of states to their respective $B\rho$ values. It should be noted that the focal-plane position of each state is largely dependent on the magnetic field inside the $K600$ spectrometer, which in turn is very sensitive to external conditions like temperature and humidity. As a result, position offsets of each measurement run had to be applied to the calibration in advance. In addition, the smooth background in the $\mathrm{Y_{fp}}$ vs. $\mathrm{X_{fp}}$ plane was subtracted [see Sec. (4.7.1)]. We determined the position of the states employed in the calibration process by a Gaussian fit to their peak in the position spectrum. The respective magnetic rigidity values were calculated from the literature exciation energy ($\mathrm{E_x}$)

Table 4.2: States involved in the energy calibration process. The excited nuclei, J^π values and evaluated literature excitation energies are shown. In addition, the respective $B\rho$ values for 200 MeV proton scattering at the respective scattering angle calculated by Relkin [77] are shown.

Target Nucleus	J^π	lit. E_x (MeV)			$B\rho$ (kG·cm)				Weekends
					0° data		4° data		
^{12}C	2^+	4.438 91	(31)	[78]	-		2122.825	(2)	4
^{12}C	0^+	7.654 20	(15)	[78]	-		2103.631	(1)	4
^{12}C	1^+	12.710	(6)	[78]	2073.694	(37)	-		1
^{12}C	1^+	15.110	(3)	[78]	2059.105	(18)	-		1,2
^{14}N	$1^{(+)}$	3.9481	(2)	[79]	-		2125.821	(1)	4
^{14}N	2^+	7.029 12	(12)	[79]	-		2107.455	(1)	4
^{14}N	2^+	9.172 25	(12)	[79]	2095.060	(1)	-		1,2
^{14}N	2^+	10.432	(7)	[79]	2087.479	(43)	-		1,2
^{14}N	(1^+)	12.495	(9)	[79]	2075.016	(55)	-		1
^{26}Mg	2^+	1.808 74	(4)	[80]	-		2138.713	(1)	3,4
^{26}Mg	0^+	3.588 56	(9)	[80]	-		2128.171	(1)	3,4
^{26}Mg	0^+	4.972 30	(13)	[80]	-		2119.948	(1)	3,4
^{26}Mg	$1^{(+)}$	9.2389	(8)	[80]	2094.688	(5)	2094.444	(5)	1,2,3,4
^{26}Mg	1^+	9.5635	(8)	[80]	2092.739	(5)	2092.494	(5)	1,2,3,4
^{26}Mg	1^+	10.1471	(1)	[80]	2089.230	(1)	2088.986	(1)	1,2,3,4
^{26}Mg	1^+	10.3195	(7)	[80]	2088.193	(5)	2087.948	(4)	1,2,3,4
^{26}Mg	1^+	10.6473	(8)	[80]	2086.219	(5)	2085.975	(5)	1,2,3,4
^{26}Mg	(2^+)	10.824	(3)	[80]	2085.155	(18)	-		1,2
^{26}Mg	1^+	11.1535	(10)	[80]	2083.169	(6)	2082.925	(6)	1,2,3,4
^{26}Mg	(5^-)	11.465 62	(8)	[80]	2081.286	(1)	-		1,2
^{64}Zn	2^+	3.005 71	(14)	[81]	-		2131.775	(1)	3,4
^{64}Zn	(2^+)	3.7106	(7)	[81]	-		2127.595	(4)	3,4

values using the two-body kinematics code Relkin [77]. Strong states from ^{12}C [78], ^{14}N [79], ^{26}Mg [80] and ^{64}Zn[81] were used in the calibration process. Table (4.2) contains a list of the states used in the calibration procedure. The calculated $B\rho$ values were fitted to their respective X_{fp} values using a 2^{nd} order polynomial function. The fit for the first weekend is shown in Fig. (4.17a) and the calibration parameters of all measurement weekends are summarized in Tab. (4.3). To check the quality of the calibration, we compared the $B\rho$ values calculated from the literature E_x value to the $B\rho$ values calculated from the fitting function. This is shown in Fig. (4.17b). The deviations are less then 0.05 kG·cm, which corresponds to a difference in E_x of less than 6 keV. The calibrated 0° and 4° ^{64}Zn spectra are shown in Fig. (4.21).

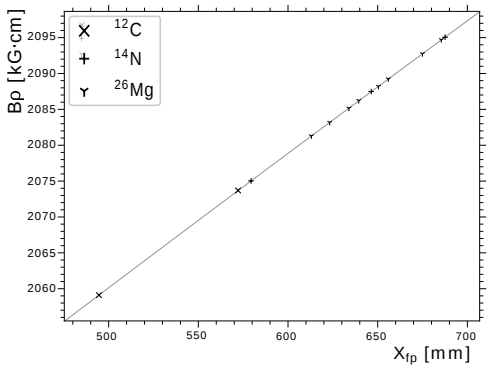

(a) $B\rho$ vs. X_{fp} calibration fit for the first measurement weekend using a 2nd order polynomial function. Errors in $B\rho$ and X_{fp} are included, but are to small to be visible.

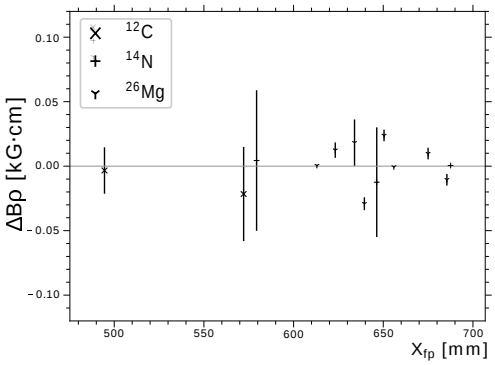

(b) Quality check for the calibration function. The difference $\Delta B\rho$ between $B\rho$ values calculated from the literature E_x values and the $B\rho$ values calculated from the calibration function is shown.

Table 4.3: X_{fp} to $B\rho$ calibration parameters for each experiment weekend.

order	Weekend 1	Weekend 2	Weekend 3	Weekend 4
0	1962.60	1961.13	1998.31	1998.76
1	0.20144	0.20143	0.20146	0.202242
2	-1.27902e-05	-1.28092e-05	-9.36438e-06	-1.06900e-05

4.7 Background Subtraction

In the previous sections we described analysis procedures that were applicable to the full data set of each weekend. From this point on, we will focus our discussion on the analysis of the data measured with the ^{64}Zn target.

4.7.1 Vertical Background

As described in Sec. (4.4), some instrumental background is still present after the particle identification. Figure (4.18) shows the distribution of events in the Y_{fp} vs E_x plane. The events related to nuclear excitations, also called *real events*, are 'sitting' on top of a featureless background. To determine the E_x distribution of background events, we projected the *background region* ($-40 < Y_{fp} < -5$ and $28 < Y_{fp} < 40$) to the E_x axis. Similarly, the spectrum of the region of real events was obtained by projecting the $-5 < Y_{fp} < 28$ region to the E_x axis. The background spectrum was smoothed and scaled to feature the background distribution visible in the real event's spectrum.

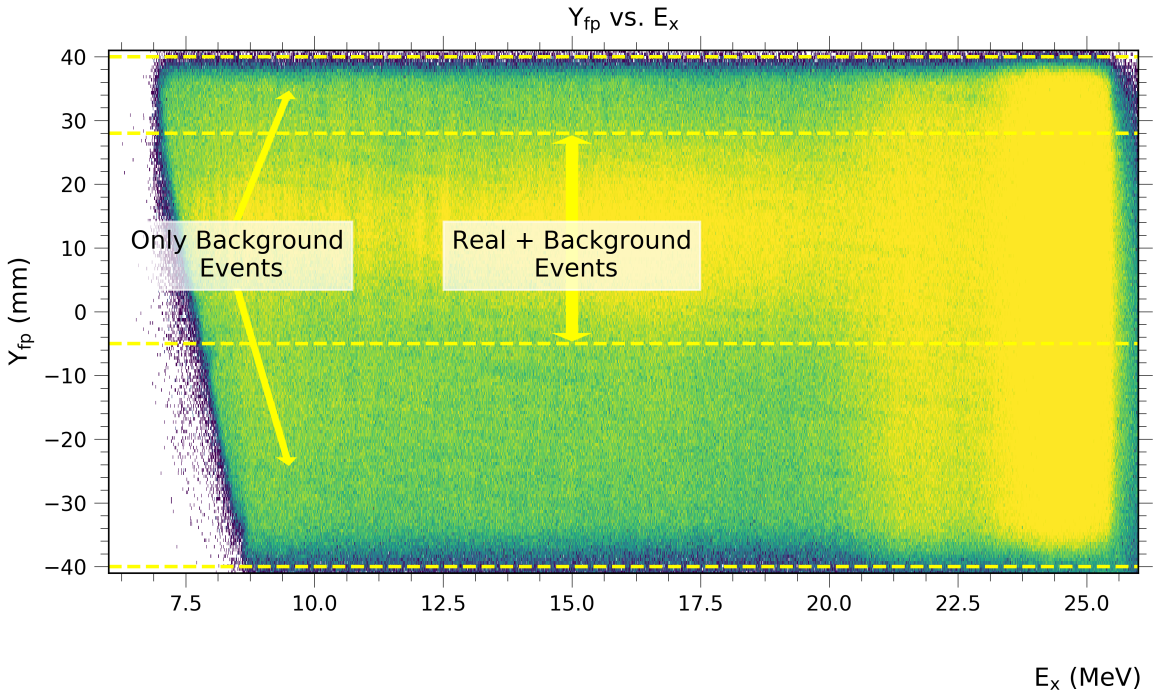

Figure 4.18: Y_{fp} vs E_x spectrum of ^{64}Zn at 0°.

To obtain the 'background-free' spectrum, the background spectrum was subtracted from the spectrum of the real events region. Figure (4.19) shows the background and the real events spectrum as well as a 'background-free' spectrum for ^{64}Zn. Around 22 and 25 MeV there is an increased contribution of background events. These events are caused by elastically scattered beam particles that punch through the neck of the $K600$ collimator and experience secondary scattering inside the spectrometer [26]. A detailed explanation of this process is given in Sec. (2.6). As seen in Fig. (4.18), these events also behave as a smooth function of Y_{fp} and thus were also removed during the subtraction procedure.

4.7.2 Residual Background and Contamination

After the subtraction of the vertical background contribution, target related background as well as instrumental background still contribute to our spectra. At low excitation energies we observed an erratic structure. This is caused by the fall-off of the acceptance of the detector system towards the high-momentum side [see Fig. (4.18) and (4.19)]. In addition, the contribution of secondary scattered beam particles increases in this region. In the subsequent analysis, we only analyzed states that were recorded at full detection

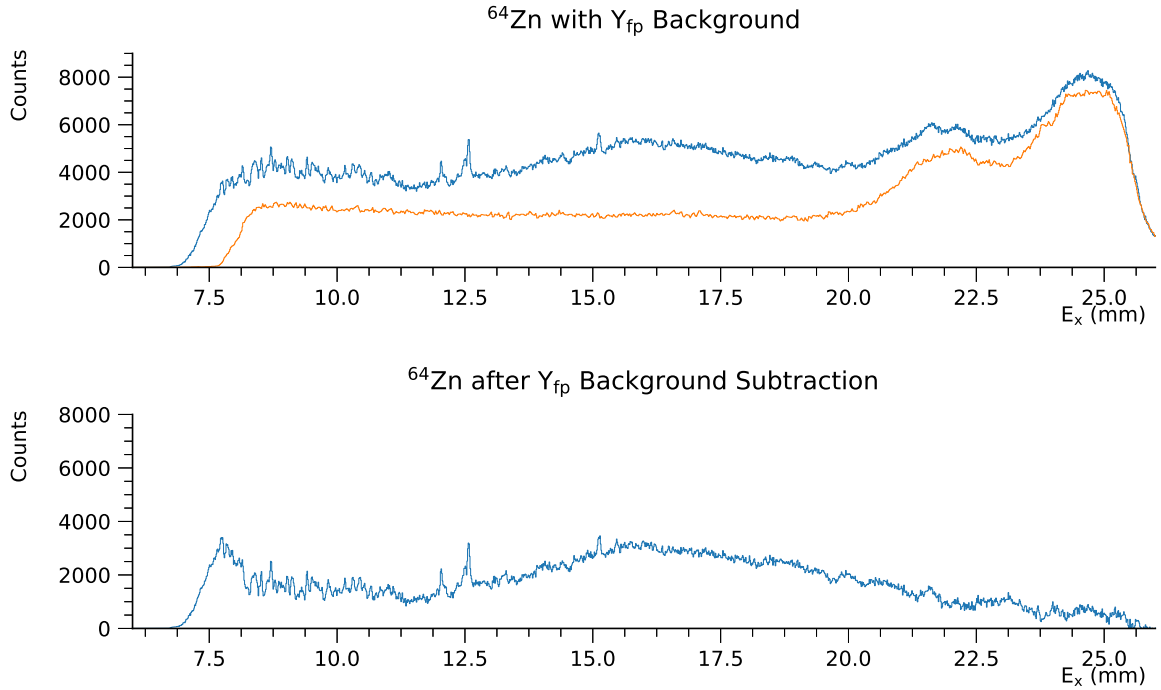

Figure 4.19: 0° spectrum of ^{64}Zn.

acceptance, i.e., above 8.2 MeV in the 0° and above 2.2 MeV in the 4° spectrum. At about 6 MeV, an increased background appears in our spectra [see Fig. (4.20)]. In this region, we expect the largest contribution of $T_0 = 2$ Spin-$M1$ states. In addition, $E1$ states akin to the PDR are expected in this region [see Sec. (1.5.3)]. Furthermore, the three-body nature of nucleon knockout quasi-elastic scattering reactions can contribute to a smooth background at these energies [8]. At even higher excitation energies above 11 MeV, we additionally observe a broad resonance-like structure with its center at about 16 MeV. This structure is linked to the GDR, which is predominantly excited at small scattering angles [see Sec. (1.5.2)].

To decompose all contributions of the background to the spectrum is difficult. Because this work mainly focuses on the evaluation of the structured part of the spectra, which is 'sitting' on top of the continuum, we subtracted the background by connecting the valleys in between states in a best-effort manner. The assumed background distribution and the 'background-free' spectrum are shown in Fig. (4.20).

One additional remark should be made for contributions to our spectra caused by target contamination. At ≈ 15.1 MeV we observe a rather strong peak [see Fig. (4.20)]. This peak is connected to the 15.110 MeV state of ^{12}C. We estimated the contribution

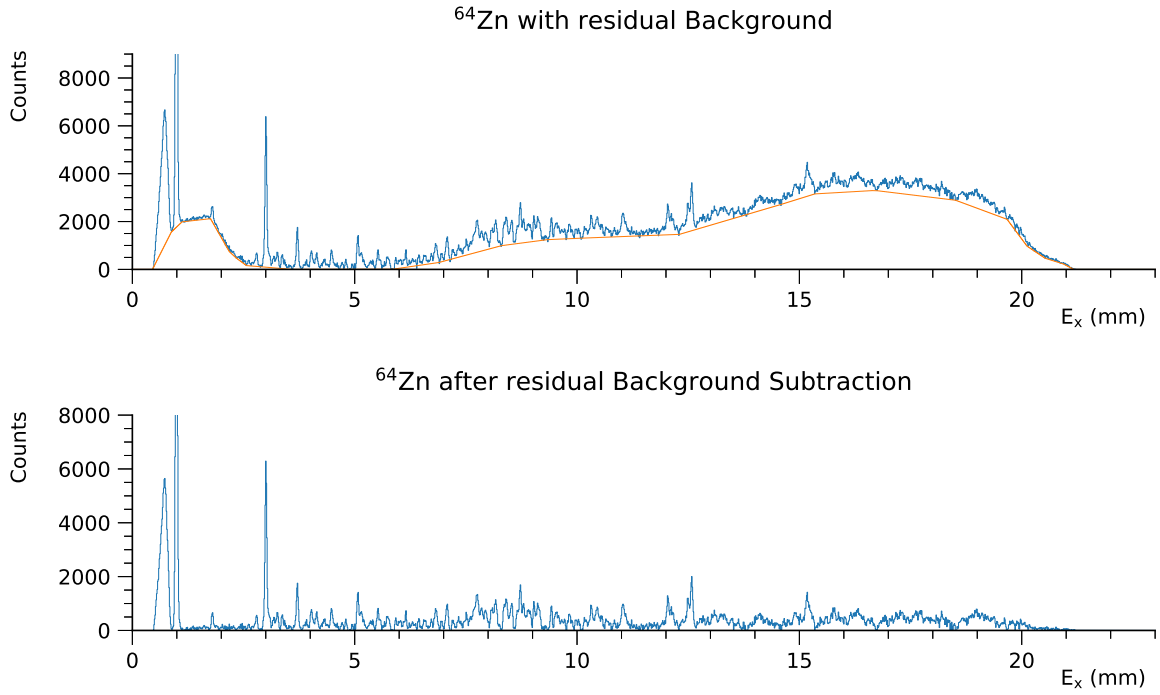

Figure 4.20: 4° spectrum of ^{64}Zn. The background was estimated by connecting the valleys between peaks.

from other ^{12}C states by comparing our ^{64}Zn spectrum to a Melamine spectrum taken under the same conditions and scaled by the height of the 15.110 MeV state. Because the other ^{12}C states are much weaker in the observed energy range, we did not recognize more contaminant states. Other likely contamination can originate from the stable ^{64}Zn isotopes, ^{66}Zn (27.7%), ^{67}Zn (4%), ^{68}Zn (18.5%), ^{70}Zn (0.6%). However, owing to the high enrichment of the employed target of $\approx 99\%$ [47], contribution from other Zinc isotopes should be negligibly small. Finally, we note that contamination stemming from other nuclei was not observed in our spectra.

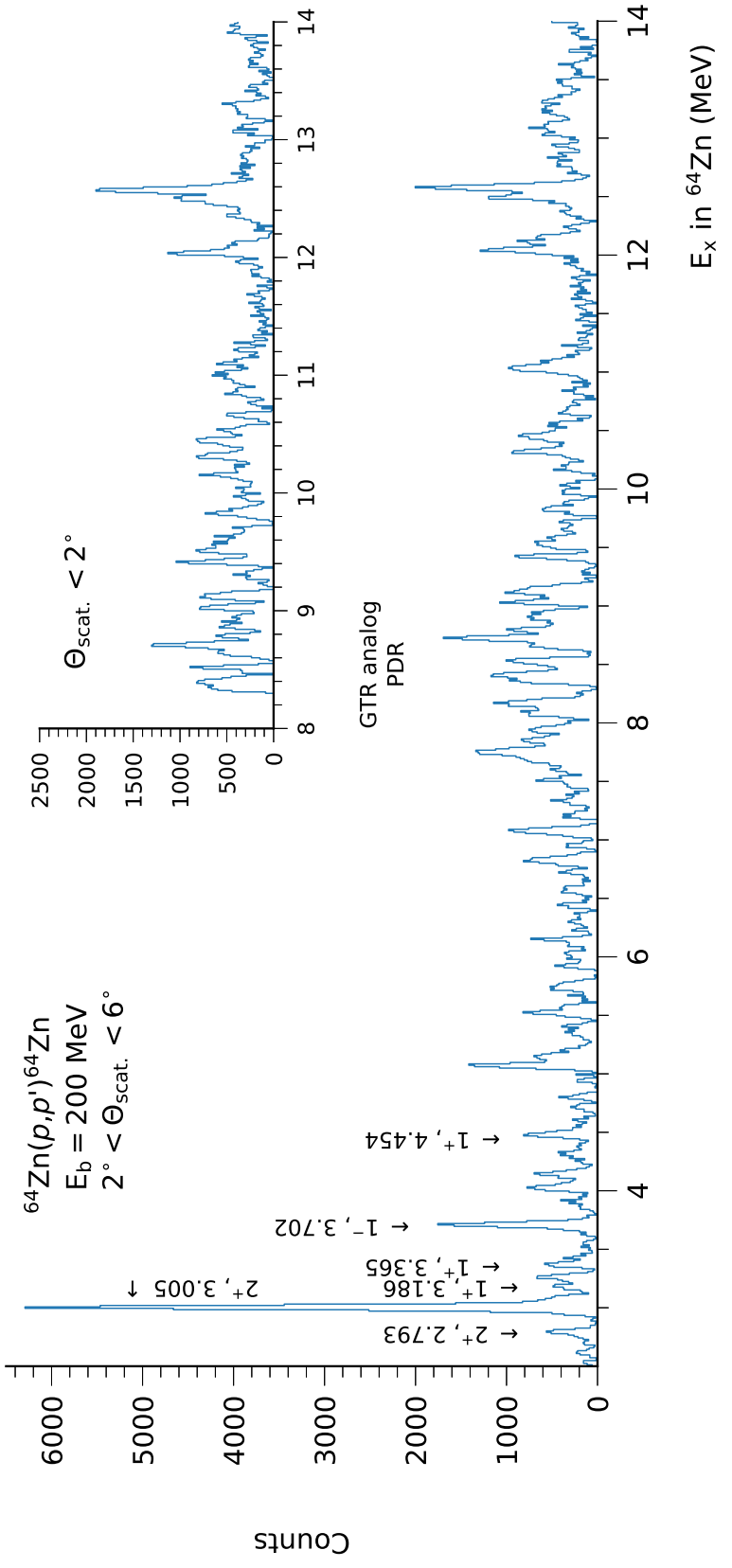

Figure 4.21: ^{64}Zn$(p,p')^{64}$Zn reaction spectra after calibration and background subtraction. Literature E_x values of states with known J^π values are indicated by arrows.

5 Analysis of Spectra

5.1 Peak-Deconvolution Analysis

The aim of the present work is the identification of the isospin of Spin-$M1$ states in ^{64}Zn and their analogs in ^{64}Ga and ^{64}Cu and the determination of the strength to these transitions. Among the desired Spin-$M1$ states, we also observe states excited by other transitions such as $E1$ or $E2$ in our spectra [see Sec. (1.5.2) and (1.5.3) and Fig. (4.21)]. As a result, the level density in the spectrum can be high and individual states may overlap. We can distinguish the nature of a transition by studying the properties of the respective excited state. In addition, we can determine the transition strength of Spin-$M1$ transitions from the yield of an identified Spin-$M1$ state. It is therefore crucial to disentangle the distribution of individual states in the spectrum. For that purpose, we performed peak-deconvolution procedures on the 0° and 4° ^{64}Zn spectra.

A standard peak shape was obtained from a detailed analysis of the shape of the prominent 3.006 MeV $J^\pi = 2^+$ [81] state. The standard peak shape is shown in Fig. (5.1). The central part of the peak was obtained directly from the 3.006 MeV state in the 4° spectrum. The tail parts on each side were interpolated from an exponential function fit to the counts in this region. This standard shape as well as the spectrum of interest and a list of peak positions were fed into the computer code SFit [82]. By varying the width, height, and position of the input states, the SFit routine reconstructs the shape of the underlying spectrum. The results of the SFit analysis for the ^{64}Zn spectrum at 0° and at 4° are shown in Fig. (5.2) and (5.3), respectively. Because the 0° spectrum

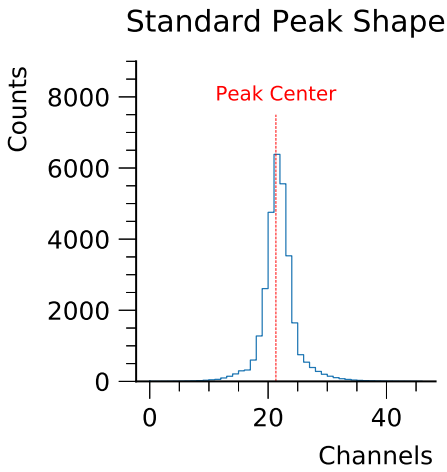

Figure 5.1: Standard peak shape obtained from the strong ^{64}Zn state at 3.006 MeV. The channels on the x axis are equivalent to the channels in the spectrum.

suffers from a large experimental background below 8 MeV, the deconvolution procedure was only applicable above that energy.

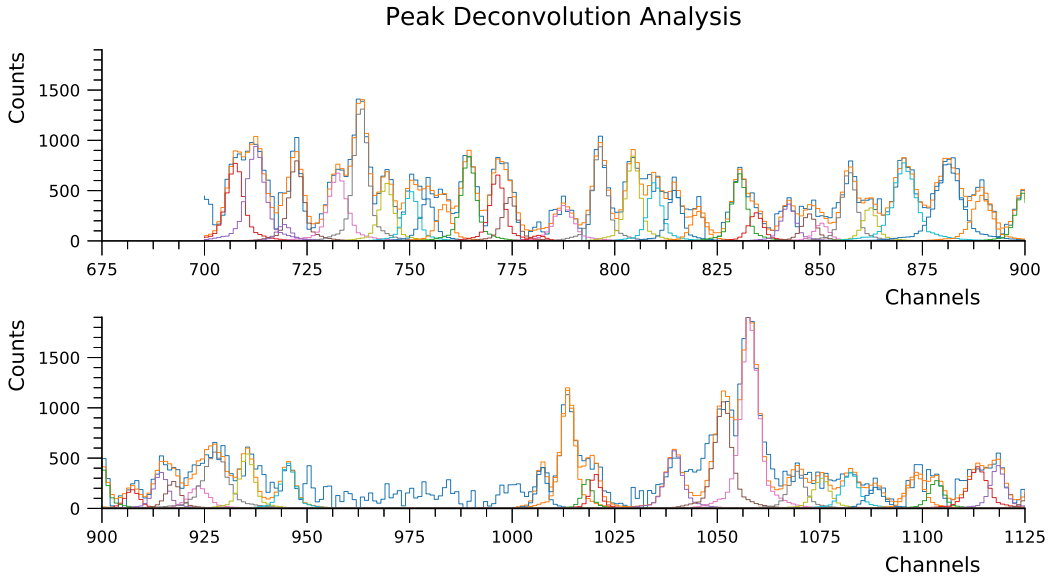

Figure 5.2: This figure shows the results of the peak deconvolution process performed for the ^{64}Zn(p,p')^{64}Zn spectra at 0°. The displayed range corresponds to energies from ≈ 8 to ≈ 15 MeV. Between 950 and 1000 channels, no clear states were observed.

5.2 Distorted-Wave Born Approximation Calculation

In Eq. (1.10), the distortion factor $K(\omega)$ describes the reaction kinematics involved in the (p,p') reaction. To account for this factor, we performed DWBA calculations using the DWBA code DWBA98 [83]. The optical model potential parameters were computed by the equations given by Schwandt *et al.* in [84]. We used the Shell-Model code Normod [1, 85, 86, 87] to calculate the nuclear wave functions and one-body transition densities (OBTDs). In the calculations, we determined the cross sections for the Spin-$M1$ transitions at 0° and 4° as a function of the excitation energy. Figure (5.4a) shows the calculated cross sections for 0° and 4° normalized by the respective ground state cross section. To obtain an analytic expression for these distributions, we fitted the calculated values using third order polynomials. The fitting parameters are listed in Tab. (5.1).

An additional application of the DWBA calculations for our analysis is the calculation of the angular distribution of transitions with different angular momentum transfer

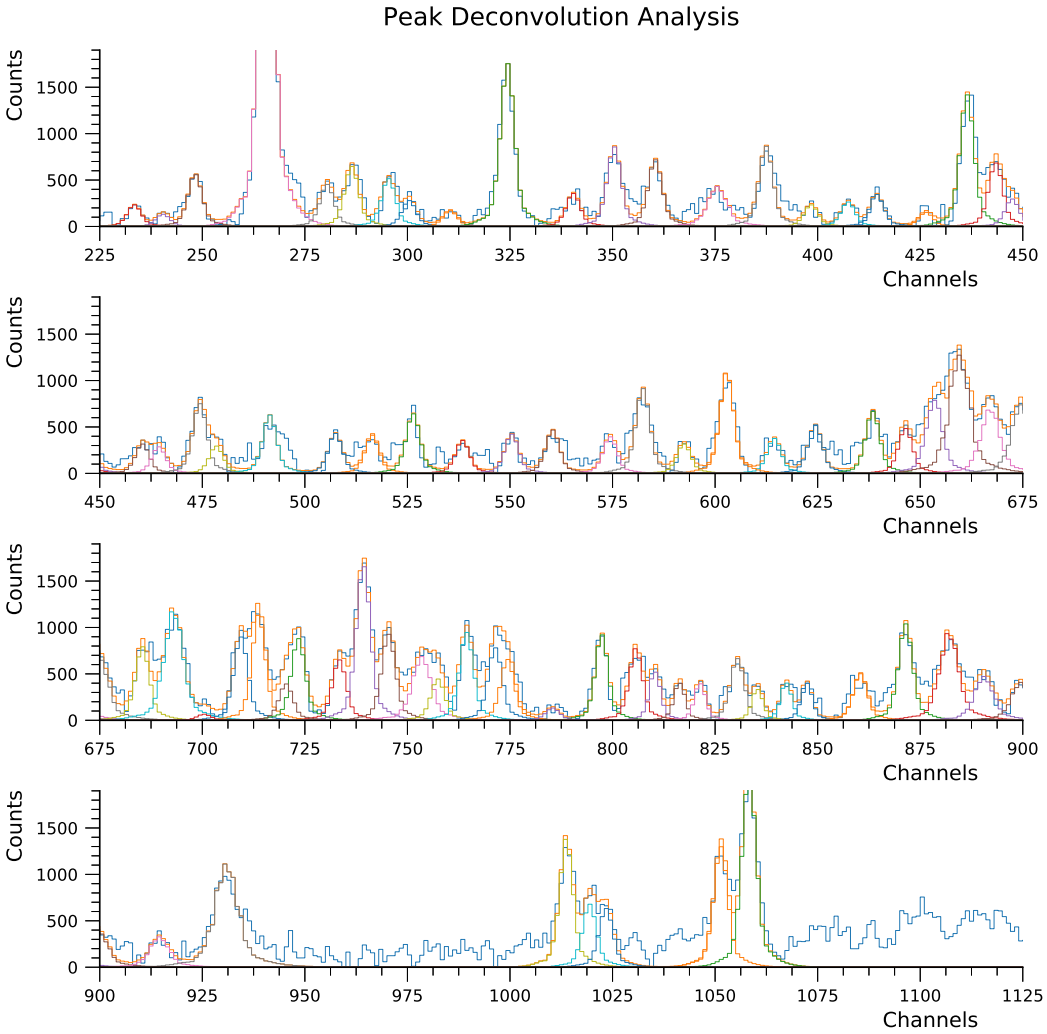

Figure 5.3: This figure shows the results of the peak deconvolution process performed for the ^{64}Zn(p,p')^{64}Zn spectra at 4°. The displayed range corresponds to energies from ≈ 2 to ≈ 15 MeV. Between 950 and 1000 channels and above 1070 channels, no clear states were observed.

(ΔL). Because known 1^- and 2^+ states are also observed in our ^{64}Zn spectra, we expect contributions from $E1$ and $E2$ transitions. We calculated the expected angular distribution for Spin-$M1$, $E1$ and $E2$ transitions between 0° and 10° at 12.0 MeV excitation energy. Similar to the description above, the nuclear wave functions and OBTDs were calculated with the code NORMOD. The results are shown in Fig. (5.4b).

Table 5.1: Parameters of third order polynomial functions fitted to the normalized DWBA cross sections at 0° and 4° between 0.0 and 30.0 MeV.

Θ	order of polynomial			
	0	1	2	3
0°	1.0	-2.76e-03	-9.32e-04	1.41e-05
4°	1.0	-2.24e-03	-8.29e-04	1.18e-05

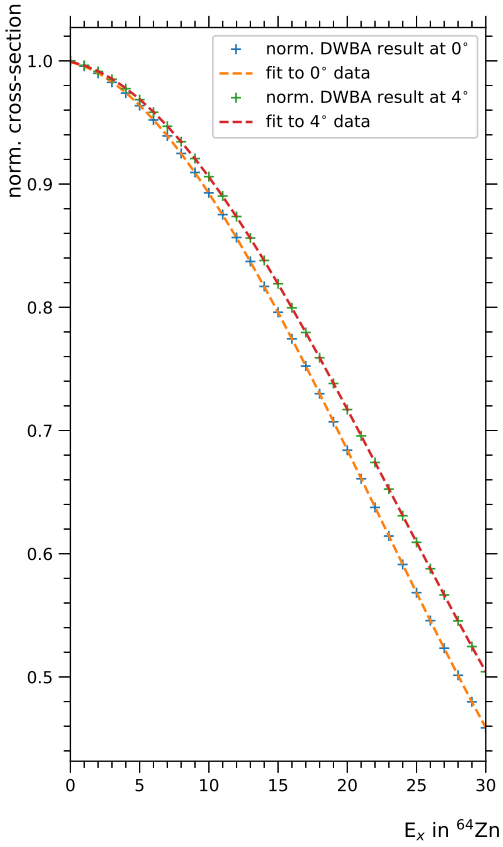

(a) Excitation energy dependence of the cross section for Spin-$M1$ transitions at 0° and 4° estimated by DWBA calculations. The estimated are normalized to the cross section at 0 MeV ($q = 0$). The crosses show the calculated values and the dashed lines mark third order polynomial functions fitted to these points.

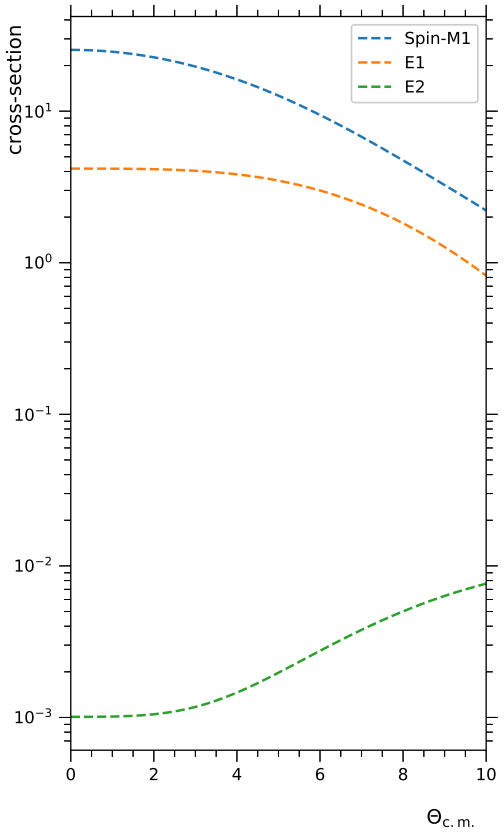

(b) This figure shows the DWBA calculated angular distributions of states excited by Spin-$M1$, $E1$, and $E2$ transitions at $E_x = 12$ MeV.

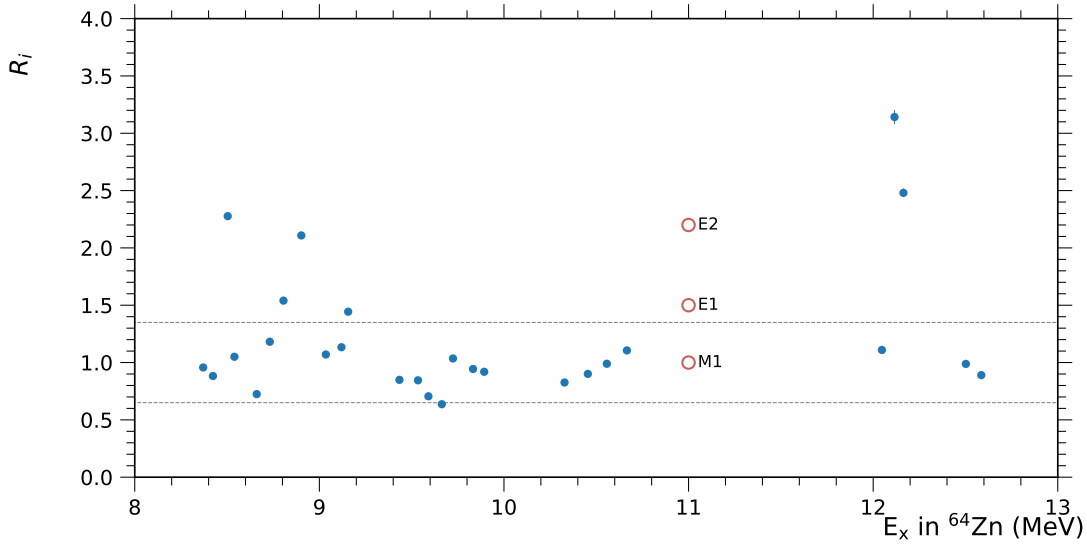

Figure 5.5: The R_i values of all states with corresponding partners in the 0° and the 4° spectra are shown. Statistical errors are included but are in most cases to small to be visible. The vertical lines indicate 35% deviation from unity. Following the approach introduced in [88], states within these lines should be assigned to $\Delta L = 0$ transitions. In contrast, states with R_i outside the vertical lines should be related to higher order ΔL transitions. The R_i values for $M1_\sigma$, $E1$, and $E2$ transitions estimated from DWBA calculations are shown as red circles.

5.3 Angular Distributions

The Spin-$M1$ transitions' angular distribution is strongly forward-peaked owing to the $\Delta L = 0$ property of the $\sigma\tau$ operator. For that reason, we expect that the cross section of the Spin-$M1$ transitions is largest in the 0° setup of our experiment. On the other hand, transitions with an angular momentum transfer larger than zero ($\Delta L \geq 1$) were also induced in our experiment. These transitions can be distinguished from the Spin-$M1$ transitions by the angular distribution of the excited states. In order to study the angular distribution of states in more detail, we performed measurements in the 0° and the 4° mode of the $K600$ spectrometer. In the 4° mode the true scattering angle of the protons at the target positions can be determined through the *Pepper-Pot* technique [see Sec. (2.5) and (4.3.2)]. This allowed us to sort our data into angular bins between 2° and 6°. However, because of the small peak-to-background ratio in our spectra, the reduced statistics in the angular bins introduced large ambiguities in the peak-deconvolution process. Consequently, we focused on the evaluation of the accumulated peak yields in the 0° and the 4° spectra.

In an earlier study, we compared the spectra of GT^- and GT^+ transitions starting

from ^{64}Zn [47] and found corresponding structures for the transitions to the $T_> = 3$ states. We compared our data to a recent ^{64}Zn(d,^{2}He)^{64}Cu reaction experiment [53] [see Sec. (1.7.2)]. As a result of the Gamow-Teller selection rules, only the $T = 3$, $J^\pi = 1^+$ states are excited in ^{64}Cu in the ^{64}Zn(d,^{2}He)^{64}Cu reaction. These states are the analog states to the $T = 3$, $J^\pi = 1^+$ states excited in the present ^{64}Zn(p,p')^{64}Zn experiment [see Fig. (1.5)]. By comparison of the ^{64}Zn and ^{64}Cu spectra, we found a good correspondence for the strong state at 12.047 MeV in ^{64}Zn and the 2.66 MeV state in ^{64}Cu as well as for the 12.584 MeV state in ^{64}Zn and the 3.19 MeV state in ^{64}Cu [see Fig. (5.6)]. We extracted the yield $\sigma(\Theta)$ of these two states in the 0° and the 4° spectrum and calculated the average ratio $\hat{r} = \frac{\sigma(4°)}{\sigma(0°)}$. Similarly, we calculated the ratio for all other states with corresponding peaks i in the 0° and the 4° spectra by $r_i = \frac{\sigma_i(4°)}{\sigma_i(0°)}$. The r_i values were then normalized by $\hat{r}$, i.e., $R_i = r_i/\hat{r}$. States with R_i values close to 1 should have a similar ratio of counts in the 4° and the 0° spectrum as the two identified Spin-$M1$ states and should therefore have a similar angular distribution of the cross section. The R_i values of all states evaluated in the analysis are shown in Fig. (5.5). It is important to note that the $\Delta L = 1$ $E1$ transitions are also expected to have a forward peaked cross section. This is a result of the deformation of the electric field of the protons at relativistic energies [89]. In Sec. (5.2) we calculated the angular distribution of the cross section of $M1_\sigma$, $E1$ and $E2$ states using DWBA calculations. From these results we can estimate the ideal R_i values for $M1$, $E1$, and $E2$ transitions. These ratios are shown in Fig. (5.5) as red circles. The DWBA calculations predict that the cross sections of $E1$ transitions do not decrease as rapidly as those of Spin-$M1$ transitions [see Fig. (5.4b)]. Therefore, $E1$ states are expected to have ratios around 1.5. Consequently, we only selected states with ratios deviating no more than 35% from unity as Spin-$M1$ candidates. This way, we were able to discover 20 Spin-$M1$ candidate states in the 0 and 4° spectrum.

5.4 Isospin Assignement

5.4.1 Comparison of GT$^+$ and GT$^-$ Strength

If isospin symmetry in the isospin multiplet around ^{64}Zn is present, $\sigma\tau$-type transitions starting from ^{64}Zn should excite states with corresponding excitation energies. In this case, these transitions are also expected to have similar strengths.

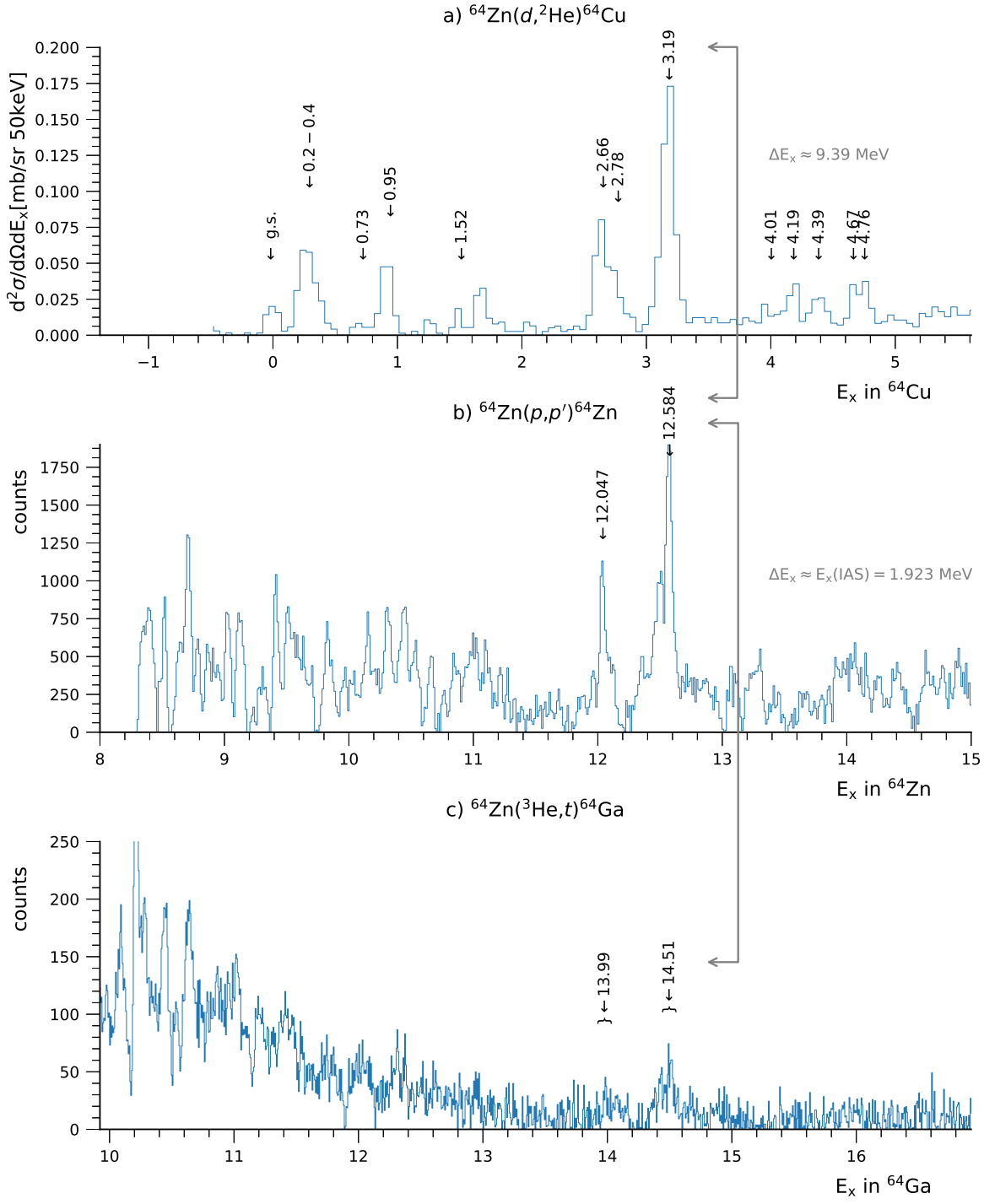

Figure 5.6: The ^{64}Zn(d,^{2}He)^{64}Cu, ^{64}Zn(p,p')^{64}Zn, and ^{64}Zn(^{3}He,t)^{64}Ga spectra aligned by the strong $T_> = 3$ states. The heights of the ^{64}Zn(p,p')^{64}Zn and the ^{64}Zn(d,^{2}He)^{64}Cu spectra are scaled by the heights of the prominent $T_> = 3$ states. The ^{64}Zn(^{3}He,t)^{64}Ga spectrum is scaled in a way that the states in the 10 to 11 MeV region have similar height as the states in the ^{64}Zn(p,p')^{64}Zn spectrum in the corresponding region.

As mentioned above, we compared our ^{64}Zn(p,p')^{64}Zn spectrum to the spectra measured in a ^{64}Zn(^{3}He,t)^{64}Ga and ^{64}Zn(d,^{2}He)^{64}Cu experiment. By doing so, we found a good agreement for the strong states at 12.047 and 12.584 MeV in ^{64}Zn with weak structures at 14.0 and 14.5 MeV in ^{64}Ga and also with analogs at 2.66 and 3.19 in ^{64}Cu. This already suggests that the isospin symmetry in this isospin multiplet is well established.

In the ^{64}Zn(^{3}He,t)^{64}Ga experiment, GT$^-$ states were identified by their angular distribution using a similar technique as described in Sec. (5.3). Because the level density was too large at high excitation energies, this technique could not be applied above $\approx$ 10.7 MeV. For that reason, the GT strength of the weak structures at $\approx$ 14.0 and $\approx$ 14.5 MeV was not determined. We reevaluated the data and estimated the $B(\mathrm{GT}^+)$ values from the cumulative cross section of the respective structures using Eq. (1.23). An R^2 value of 9.1 ± 0.4 was obtained from interpolation of the mass dependence of known R^2 values to $A = 64$ [see Sec. (1.6)]. The cross section of the Fermi transition was obtained from the IAS in the ^{64}Ga spectrum, assuming that the strength going to the IAS exhausts the full sum-rule value $B(\mathrm{F}) = 4$. In addition, it was assumed that the ratios of the Fermi and the GT cross sections are proportional to ratios of the yields of the corresponding structures in the spectrum at $q = 0$. This way we obtained a value of $B(\mathrm{GT}^-) = 0.029(2)$ for the transition to the structure at 14.0 MeV and $B(\mathrm{GT}^-) = 0.045(3)$ for the transition to the 14.5 MeV state.

The $B(\mathrm{GT}^+)$ values in the GT$^+$ direction were measured in a ^{64}Zn(d,^{2}He)^{64}Cu experiment [53]. In ^{64}Cu the states corresponding to the 13.99 MeV and the 14.51 MeV structures in ^{64}Ga are located at 2.66 and 3.19 MeV respectively. It is worth noting that the 2.66 MeV state in ^{64}Cu forms a doublet with a state at 2.78 MeV. Because these two states could not be separately resolved in the ^{64}Zn(d,^{2}He)^{64}Cu experiment, they were treated as one broad structure with $B(\mathrm{GT}^+) = 0.288(18)$ in the subsequent analysis. In contrast, the 3.19 MeV state is rather isolated in the ^{64}Ga spectrum. A $B(\mathrm{GT}^+)$ value of 0.512(21) is given for the transition to this state by Grewe *et al.* [53].

To make the $B(\mathrm{GT}^-)$ values from ^{64}Ga and the $B(\mathrm{GT}^+)$ values from ^{64}Cu comparable, the $B(\mathrm{GT}^+)$ values were normalized by the ratio of the respective isospin Clebsch-Gordon coefficients by

$$B(\mathrm{GT}^+)_{\mathrm{norm.}} = \frac{C^2_{\mathrm{GT\text{-}}}}{C^2_{\mathrm{GT+}}} B(\mathrm{GT}^+), \tag{5.1}$$

where $C^2_{\mathrm{GT+}} = 1$ and $C^2_{\mathrm{GT\text{-}}} = 1/15$. This way we obtained a $B(\mathrm{GT}^+)_{\mathrm{norm.}}$ of 0.019(1) for the transition to the accumulated 2.66 MeV state and value of 0.034(2) for the transition to the 3.19 MeV state.

Table 5.2: Comparison of $B(\mathrm{GT})$ values of the analog transitions to the two strong GT^+ $T_> = 3$ states in ^{64}Cu and the corresponding GT^- $T_> = 3$ structures in ^{64}Ga. In addition, the average of the $B(\mathrm{GT}^+)_{\mathrm{norm.}}$ and the $B(\mathrm{GT}^-)$ is shown.

E_x in ^{64}Cu (MeV)	$B(\mathrm{GT}^+)$	$B(\mathrm{GT}^+)_{\mathrm{norm.}}$	E_x in ^{64}Ga (MeV)	$B(\mathrm{GT}^-)$	avg. $B(\mathrm{GT}^-)$
2.66+2.78	0.288(24)	0.019(1)	13.99	0.029(2)	0.024(2)
3.19	0.512(21)	0.034(1)	14.51	0.045(3)	0.040(2)

In Tab. (5.2), we compare the strengths of the analog GT^+ and GT^- transitions to the two $T_> = 3$ states. For these transitions, the $B(\mathrm{GT})$ values in the GT^- direction appear to be on average 40% stronger than the $B(\mathrm{GT})$ values in the GT^+ direction. It is important to note that both values suffer from various ambiguities. The strength of the GT^- transitions is largely influenced by the assumption that respective structures in the spectrum are purely attributed to GT$-$ $T = 3$ states. However, in this high energy region the level density is large and therefore, GT states with $T <= 1$, $T_0 = 2$ as well as states excited by higher mulipolarity transitions can contribute to the observed structure. In addition, the $T_> = 3$ structures are sitting on top of a large background related to the so-called quasi-free scattering process. We estimated this background by a smooth function to separate the real events from the background distribution [88]. The assumed background distribution has a large influence on the extracted yield of the structures and therefore introduces another ambiguity. The strength of the GT^+ transitions starting from ^{64}Zn, on the other hand, was determined from the cross section of states in the ^{64}Cu spectrum. These states are rather isolated and only little contribution from transitions other than the desired GT^+ transition was observed in the spectrum. For that reason, the cross section of GT^+ states in ^{64}Cu could be obtained rather reliably. However, in [53] the $B(\mathrm{GT})$ values were calculated under the assumption that the cross section of states is proportional to the $B(\mathrm{GT})$ values [see Eq. (1.7)]. The proportionality factor (GT unit cross section) in Eq. (1.7) was calibrated with respect to the cross section of the g.s. to g.s. GT^+ transition and the $\log ft$ value of its reversed transition [90]. As can be seen in Fig. (5.6) (a), the g.s-g.s transition has a rather small cross section and is therefore affected by a large statistical error. Under the consideration of the ambiguities described above, we assume that the $B(\mathrm{GT})$ values of the analog transition shown in Tab. (5.2) are in reasonable agreement, although they exhibit an average difference of $\approx 40\%$.

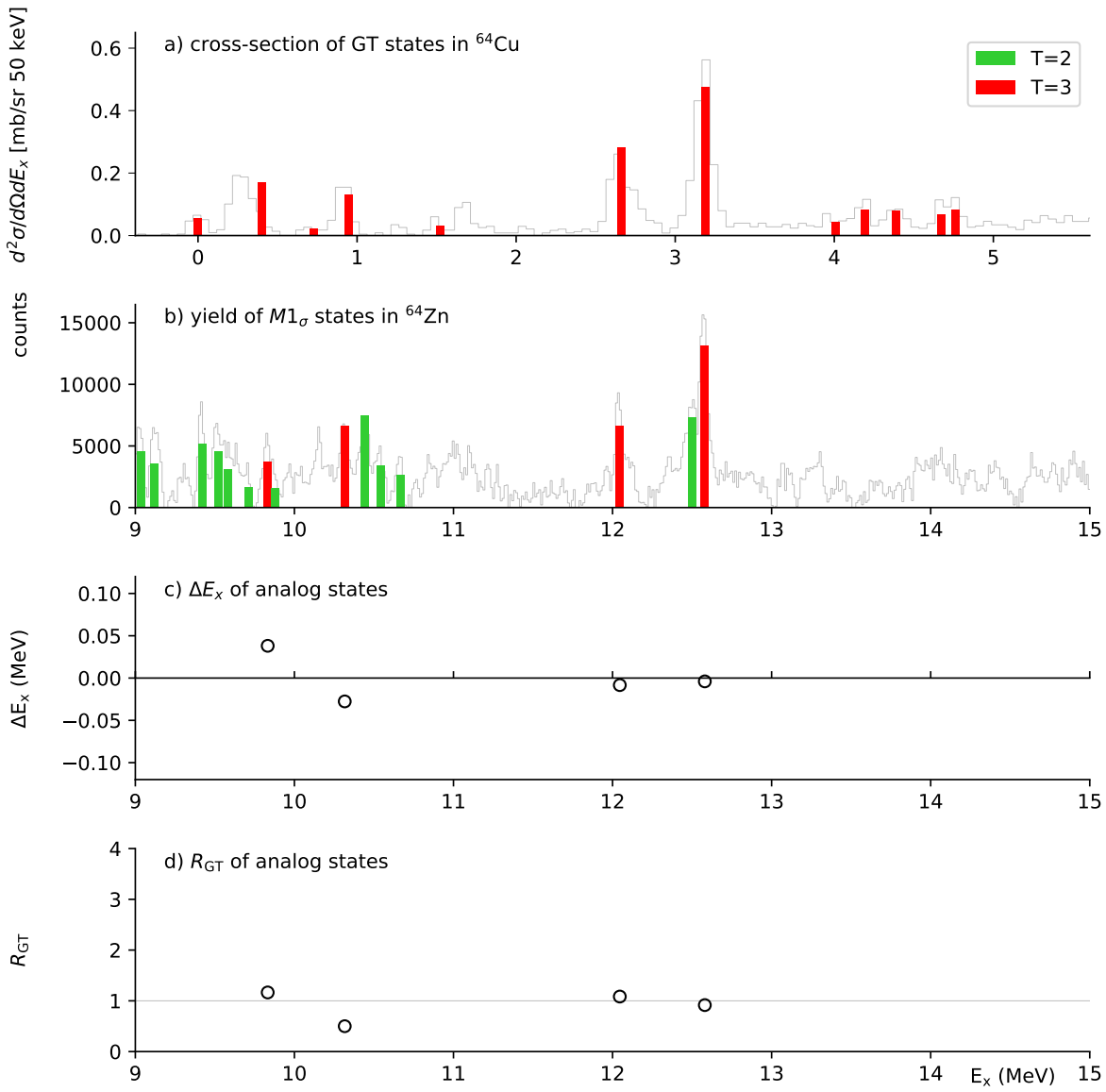

Figure 5.7: a) The cross section of GT states measured in a ^{64}Zn(d,^{2}He)^{64}Cu experiment [53]. The cross sections of states identified as $T = 3$ are shown as red colored bars. The grayed out ^{64}Zn(d,^{2}He)^{64}Cu spectrum is shown to indicate the states in the spectrum. The spectrum is scaled arbitrarily to show good correspondence with the height of the respective bars. b) Yields of the $M1_\sigma$ states obtained in the ^{64}Zn(p,p')^{64}Zn experiment. We extrapolated the yields to $q = 0$ using DWBA calculations to eliminate the dependence on the excitation energy. The yield of states identified as $T = 2$ and $T = 3$ are shown as green, and red colored bars, respectively. The grayed out ^{64}Zn(p,p')^{64}Zn spectrum is shown to indicate the states in the spectrum. The spectrum is scaled arbitrarily to show good correspondence with the height of the respective bars. c) Energy differences ΔE$_x$ of the corresponding Spin-$M1$ and GT states are shown. The energy difference of the strong $T_> = 3$ states $\Delta E = 9.39$ MeV is taken into account. d) The ratios R_{GT} of corresponding states are shown. The values are normalized to be 1 for the strong $T_> = 3$ states.

5.4.2 States in the 0° ^{64}Zn Spectrum

In Sec. (5.3) we described a method to select Spin-$M1$ candidate states in ^{64}Zn. Assuming good isospin symmetry, the isospin T value of these states can be identified if we can find GT states with corresponding excitation energies and strengths in ^{64}Ga and ^{64}Cu. In the previous section it was shown that the GT$^+$ and the GT$^-$ strengths of analog transitions to $T_> = 3$ states are in reasonable agreement.

To identify the $T_> = 3$ states in the ^{64}Zn spectrum, we aligned the ^{64}Cu to the ^{64}Zn spectrum. Because the E_x value of the IAS of ^{64}Cu in the ^{64}Zn spectrum is not known, we aligned the spectra via the two already identified $T = 3$ states [see Fig. (5.6) (a) and (b)]. In consequence, an average energy offset of the two spectra was determined to be ≈ 9.39 MeV. The IAS of the ^{64}Cu g.s. is therefore expected at ≈ 9.39 MeV in ^{64}Zn. In Fig. (5.7) (a) and (b) we compare the cross section of the GT$^+$ states in ^{64}Cuwith the yields of the Spin-$M1$ candidate states selected in the angular distribution analysis [see Sec. (5.3)]. The vertical scales of the plots are aligned by the height of the two $T = 3$ states described above. We calculated the energy difference $\Delta E_x = E_x{}^{M1_\sigma} - (E_x{}^{GT} + 9.39\text{MeV})$ of corresponding $M1_\sigma$ candidates and GT states in ^{64}Cu [53]. In Fig. (5.7) (c), we show the ΔE_x values of corresponding states. Although analog states are expected at similar excitation energies, isospin asymmetries can cause small shifts of corresponding E_x values. Following our assumption of good isospin symmetry, the analog transitions should also exhibit similar strengths. Because the cross section is proportional to the yield of the respective excited state in the spectrum, we can compare the relative strengths of GT and $M1_\sigma$ transitions in terms of the ratio of their yields in the respective spectrum. We calculated the relative yield of all corresponding GT and $M1_\sigma$ states and normalized them by the average of the relative yield of the two strong $T_> = 3$ states. The normalized ratios of corresponding states are defined as R_{GT} values. The R_{GT} values for all analog state candidates are shown in the bottom part of Fig. (5.7).

We were able to identify two additional $T_> = 3$ states candidates with corresponding E_x and R_{GT} values. They are located at 9.422 and 10.316 MeV in ^{64}Zn and their corresponding states in ^{64}Cu have $E_x = 0.3$ and $E_x = 0.95$ MeV, respectively. It is worth pointing out that the E_x value of the ^{64}Cu state around 0.3 MeV was given as $E_x = 0.2 - 0.4$ MeV in [53]. In Fig. (5.7) (a) we placed the bar showing the yield of this state at 0.3 MeV. As a result, the bar is shifted with respect to its corresponding state in the ^{64}Cu spectrum, which is shown in the same plot.

Some states in ^{64}Zn that were selected as Spin-$M1$ candidates in the angular-distribution analysis could not be correlated with a GT state in the ^{64}Cu spectrum. These

states are assigned the isospin value $T_0 = 2$. As a result of the different CG coefficients, the analogs of these states should be strongly enhanced in the ^{64}Zn(^{3}He,t)^{64}Ga spectrum compared to the $T_> = 3$ states. However, owing to the high level density in ^{64}Ga, we could not analyze the corresponding analogs. In addition, it is important to note that $E1$ states have a similar angular distribution as the Spin-$M1$ states in IE (p,p') scattering and therefore can be mistakenly selected as Spin-$M1$ states in the angular-distribution analysis. As a result, we can only give a tentative Spin-$M1$, $T = 2$ assignment to these states. In Fig. (5.7) (a) and (b), the tentative $T = 2$ states and the $T = 3$ states are indicated by blue and red bars, respectively.

5.4.3 States in the 4° ^{64}Zn Spectrum

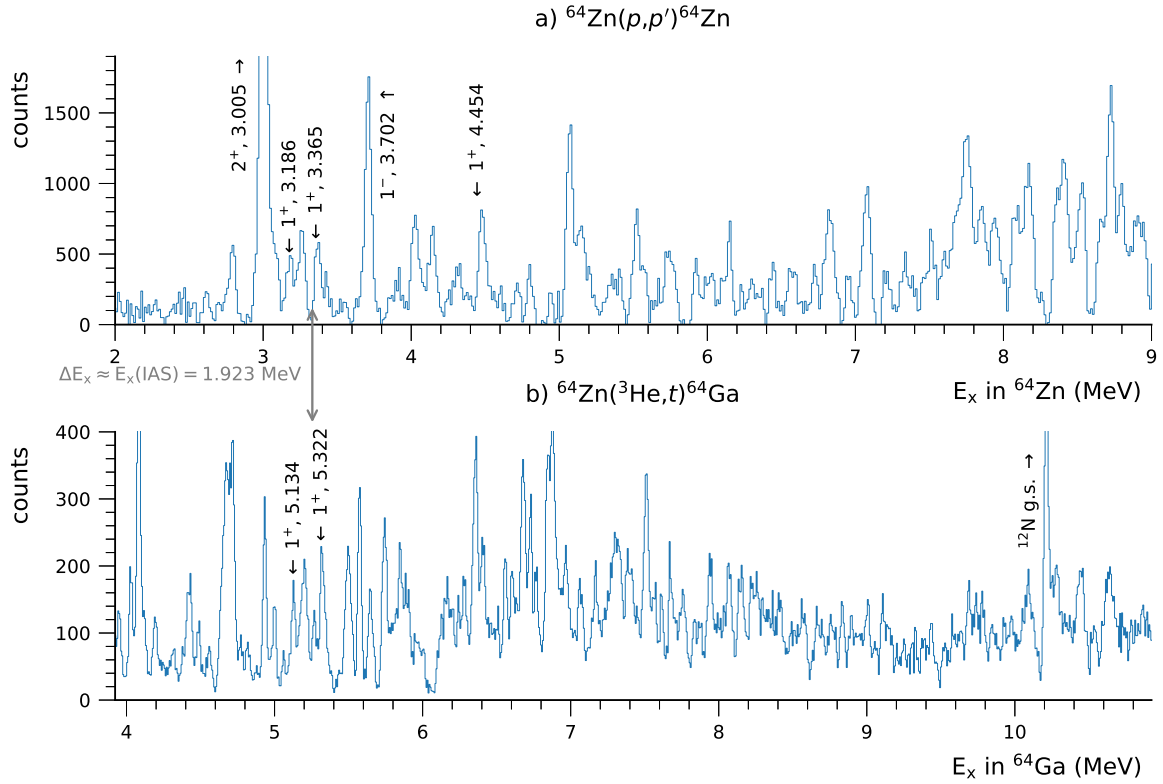

Figure 5.8: The ^{64}Zn(p,p')^{64}Zn and ^{64}Zn(^{3}He,t)^{64}Ga spectra aligned by the excitation energy of the IAS in ^{64}Zn.

In Sec. (5.3), we described a technique to distinguish Spin-$M1$ candidate states from states excited by higher multipolarity transitions by their angular distribution. This technique however, is only applicable to states that are observed in both the 0° and the

4° spectrum. In the 0° setting of the $K600$, the initial beam passes the spectrometer with the scattered protons. To protect the detector system from the beam, a beam stopper is placed at the high momentum side of the spectrometer exit. This comes at the cost of collimating excitations in the first ≈ 8 MeV of the 0° spectrum. For that reason, we can only determine the angular distribution of states above ≈ 8 MeV. In the 4° setting of the $K600$, we do not suffer directly from the incident beam. However, secondary scattering of the beam particles on the laboratory hardware contributes a large background to the detector events below ≈ 2.5 MeV.

Because we can not determine the angular distribution of states below ≈ 8 MeV, we have to rely on the assumption of good isospin symmetry. In Fig. (5.8) we compare the 4° ^{64}Zn(p,p')^{64}Zn spectrum and the ^{64}Zn(^{3}He,t)^{64}Ga spectrum. As described at the beginning of this section, we can identify the $T_0 = 2$ and $T_> = 3$ states in ^{64}Zn by the coexistence of states with corresponding relative strengths in the ^{64}Zn(^{3}He,t)^{64}Ga spectrum. In addition, we can distinguish the $T_< = 1$ states in ^{64}Ga by their non-existence in ^{64}Zn.

We aligned our 4° (p,p') spectrum and the ^{64}Zn(^{3}He,t)^{64}Ga spectrum, taking into account the E_x value of the IAS in ^{64}Zn = 1.923 MeV. This way we found a good agreement between the structures located at ≈ 14 and ≈ 14.5 MeV in ^{64}Ga and the strong states at 12.047 and 12.584 MeV. By comparison with a ^{64}Zn(d,^{2}He)^{64}Cu experiment we found that these structures are analog states with isospin $T = 3$. Because of the different CG coefficients, the $T_> = 3$ states in ^{64}Zn are enhanced by a factor of 2.5 when compared with the $T_0 = 2$ states, i.e.,

$$\frac{C^2_{M1_\sigma}(T_>)/C^2_{\mathrm{GT}}(T_>)}{C^2_{M1_\sigma}(T_0)/C^2_{\mathrm{GT}}(T_0)} = 2.5. \tag{5.2}$$

We calculated the ratio of the yield of the two corresponding $T_>$ states in ^{64}Ga and ^{64}Zn and normalized it to be 2.5. The methods we used to obtain the yields of these states in the respective spectra are described in Sec. (5.4.1) and (5.1). We used the same normalization for all states with corresponding E_x values in ^{64}Ga and ^{64}Zn. As a result, states that have isospin $T_0 = 2$ are expected to have a normalized ratio (R_{GT} value) close to one. In Fig. (5.9) (c) the energy difference ΔE_x is shown for corresponding GT and $M1_\sigma$ states. In addition, the R_{GT} values are shown in part (d) of Fig. (5.9). We were able to find 21 pairs of analog states with corresponding excitation energies and R_{GT} values close to one. We assign these states to $J = 1^+, T_0 = 2$ Spin-$M1$ states and mark them via the green bars in Fig. (5.9) (a) and (b).

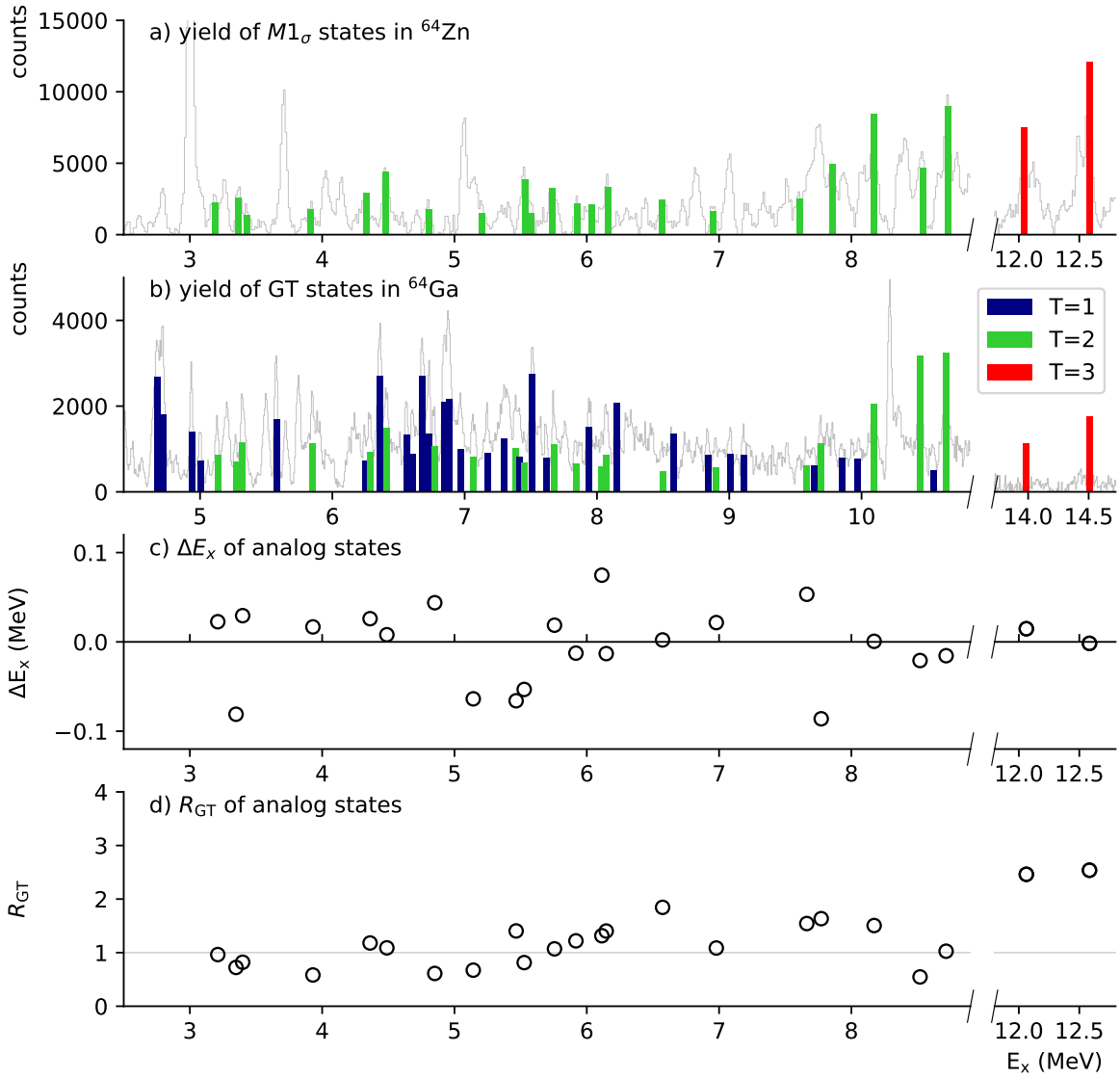

Figure 5.9: a) Yields of the states identified as Spin-$M1$ candidate states. We extrapolated the yields to $q = 0$ using DWBA calculations to eliminate the dependence on the excitation energy. The yield of states identified as $T = 2$, and $T = 3$ are shown as green and red colored bars, respectively. The grayed out ^{64}Zn(p,p')^{64}Zn spectrum is shown to indicate the states in the spectrum. The spectrum is scaled arbitrarily to show good correspondence with the height of the respective bars. b) Yields of the GT states obtained in the ^{64}Zn(^{3}He,t)^{64}Ga experiment. We extrapolated the yields to $q = 0$ using DWBA calculations to eliminate the dependence on the excitation energy. The yields of states identified as $T = 1$, $T = 2$, and $T = 3$ are shown as blue, green, and red colored bars, respectively. The grayed out ^{64}Zn(^{3}He,t)^{64}Ga spectrum is shown to indicate the states in the spectrum. The spectrum is scaled arbitrarily to show good correspondence with the height of the respective bars. c) The energy differences ΔE_x of the corresponding GT and Spin-$M1$ states are shown. The E_x value of the IAS = 1.923 MeV in ^{64}Zn is taken into account. d) The ratios R_{GT} of corresponding states are shown. The R_{GT} values are normalized to be 2.5 for the strong $T_> = 3$ states shown on the right-hand side.

Among the 21 $J = 1^+, T_0 = 2$ Spin-$M1$ states we found in this analysis, the four states at 3.186, 3.365, 3.425, and 4.454 MeV are known 1^+ states, observed in the β decay of ^{64}Cu [90]. This shows again how well the isospin symmetry is established in the isospin multiplet around ^{64}Zn. For several GT states in ^{64}Ga we were not able to find a corresponding partner in ^{64}Zn. Therefore, these states are assumed to have $T_< = 1$. In Fig. (5.9) (b) the $T_< = 1$ states in ^{64}Ga are indicated by the blue bars. We remark that for some states shown in Fig. (5.9) (a) and (b), the bar indicating the yield of a state appears much higher than the height of the corresponding peak in the spectrum. This is the result of a broader peak shape, caused for instance, when particle decay contributes to the width of a state. Similarly, the bar for the $T_> = 3$ states in ^{64}Ga is much higher than the corresponding peak, which is a result of our analysis of these states [see Sec. (5.4.1)]

5.5 Extraction of Spin-$M1$ Transition Strengths

The strength of Spin-$M1$ transitions is commonly compared in terms of their $B(M1_\sigma)$ values. We can calculate the $B(M1_\sigma)$ values of the transitions to the Spin-$M1$ states that we identified in the previous section, using Eq. (1.11):

$$\frac{d\sigma_{M1_\sigma}}{d\Omega}(q,\omega) \sim \hat{\sigma}_{M1_\sigma}(q,\omega) B(M1_\sigma),$$

where $\hat{\sigma}_{M1_\sigma}(q,\omega)$ is the $M1_\sigma$ unit cross section. In Sec. (1.6) we describe a technique to calculate $\hat{\sigma}_{M1_\sigma}(q,\omega)$ when a standard $B(\mathrm{GT})$ value of an analog transition is available. In our case, we were able to obtain the $B(\mathrm{GT}^+)$ as well as the $B(\mathrm{GT}^-)$ values from the analog GT^+ and GT^- transitions to the strong $T_> = 3$ states. In Sec. (5.4.1) we found that the $B(\mathrm{GT})$ values of these transitions are in agreement when the CG coefficients of the respective transitions are taken into account. The results are summarized in Tab. (5.2). We also calculated the average of the $B(\mathrm{GT}^-)$ and the $B(\mathrm{GT}^+)_{\mathrm{norm.}}$ values of these transitions. These values are shown in the right-most column of Tab. (5.2). To calculate $\hat{\sigma}_{M1_\sigma}(q,\omega)$, we estimated the standard $B(M1_\sigma)$ strength of the two strong $T_> = 3$ transitions from the averaged $B(\mathrm{GT}^-)$ values given in Tab. (5.2) via $B(M1_\sigma) = R_{\mathrm{MEC}} \times (C^2_{M1_\sigma}/C^2_{\mathrm{GT}}) \times B(\mathrm{GT})$ (1.24). To correctly propagate the errors of the initial values, we used a Monte-Carlo technique. We estimated the prior probability density

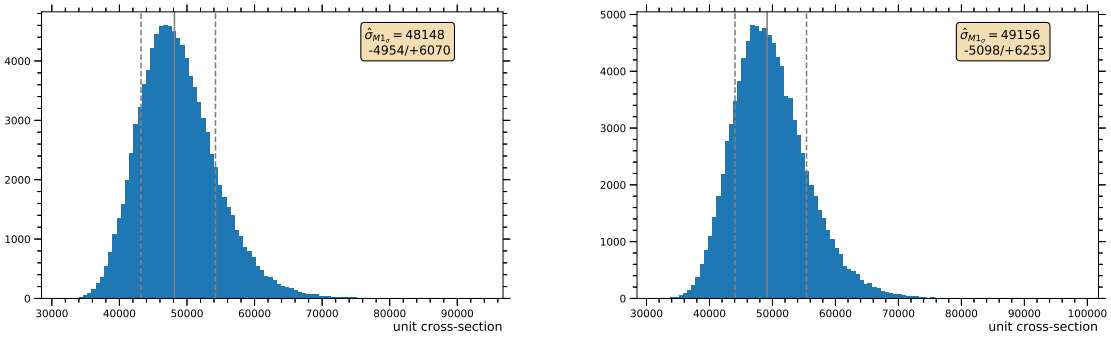

(a) 0° (b) 4°

Figure 5.10: Posterior distribution of $\hat{\sigma}_{M1_\sigma}(q,\omega)$ at 0° and 4°, calculated in a Monte-Carlo simulation.

function (pdf) of the values, which are susceptible to errors, by Gaussian distributions:

$$f(x \mid \mu, \sigma^2) = \frac{1}{\sqrt{2\pi\sigma^2}} e^{-\frac{(x-\mu)^2}{2\sigma^2}}, \tag{5.3}$$

where we used the values as the means (μ) and the errors as the standard deviation (σ) of the pdf. From the priors, we randomly sampled events and calculated the standard $B(M1_\sigma)$ value for each event. A total of 100,000 events were simulated for each standard $B(M1_\sigma)$ value. From the posterior distribution of the standard $B(M1_\sigma)$ values, we calculated the median and the negative and positive 1σ confidence intervals. This way, we obtained a standard $B(M1_\sigma)$ value of $0.152^{+0.026}_{-0.024}$ for the $M1_\sigma$ transition to the 12.047 MeV state and $B(M1_\sigma) = 0.254^{+0.039}_{-0.037}$ for the $M1_\sigma$ transition to the 12.584 MeV state. From the mean distribution of these standard $B(M1_\sigma)$ values and the average yield of the respective states in the spectrum, we then calculated the $M1_\sigma$ unit cross section. Similar to the standard $B(M1_\sigma)$ values, we used a Monte-Carlo technique, taking into account all error sources, such as the given covariance matrices of fitting parameters and the systematic and statistical error of the peak yields. We separately calculated the $M1_\sigma$ unit cross section using the yield of the peaks in the 0° and the 4° spectra. The histograms of the posterior distributions of $\hat{\sigma}_{M1_\sigma}(q,\omega)$ at 0° and 4° are shown in Fig. (5.10) (a) and (b). We obtained $\hat{\sigma}_{M1_\sigma}(q,\omega)$ values of 48148^{6070}_{-4954} at 0° and 49193^{+6253}_{-5098} at 4°, respectively. From the $\hat{\sigma}_{M1_\sigma}(q,\omega)$ values we calculated the $B(M1_\sigma)$ strengths of transitions to all states identified as Spin-$M1$ states in the respective spectra via Eq. (1.11), also in a Monte-Carlo manner. The results for the $B(M1_\sigma)$ values calculated from the yields of states in the 0° spectrum are shown in Fig. (5.11). Likewise, the results for

the $B(M1_\sigma)$ values calculated from the yields of states in the 4° spectrum are shown in Fig. (5.12). In Tab. (8.1), we summarize the transition strength of the $\sigma\tau$-type transitions starting from ^{64}Zn. The excitation energies for the levels excited by the respective transitions are also shown.

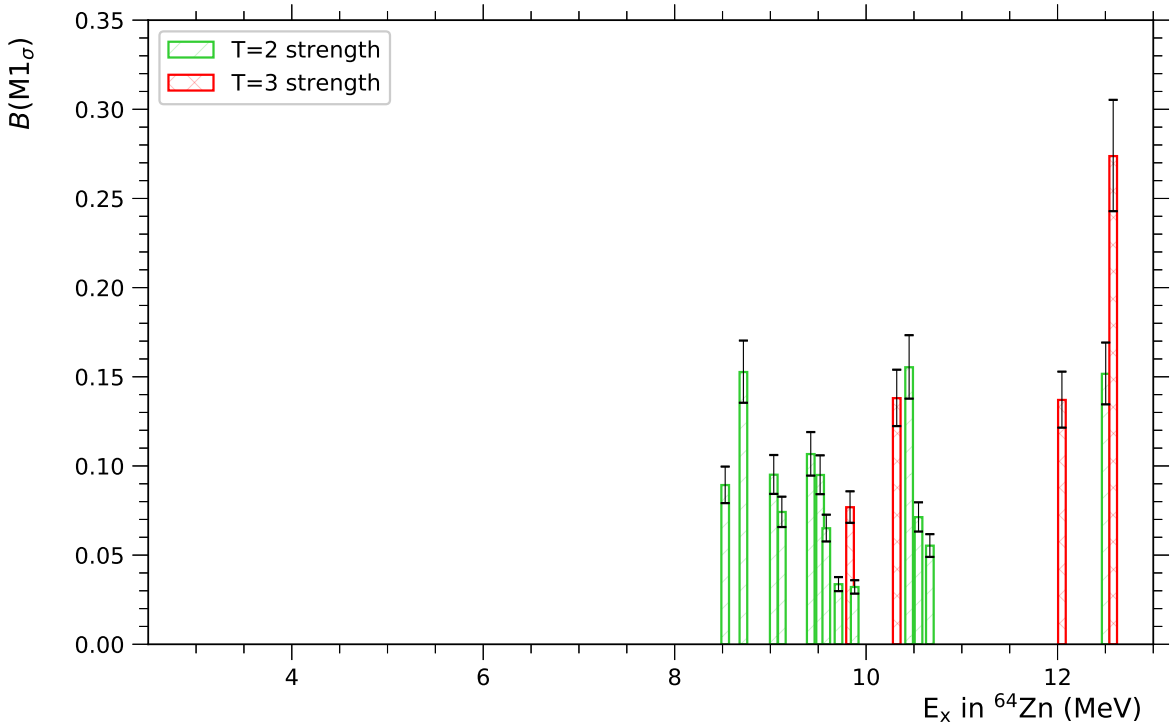

Figure 5.11: The $B(M1_\sigma)$ values calculated for the Spin-$M1$ states in the 0° ^{64}Zn spectrum.

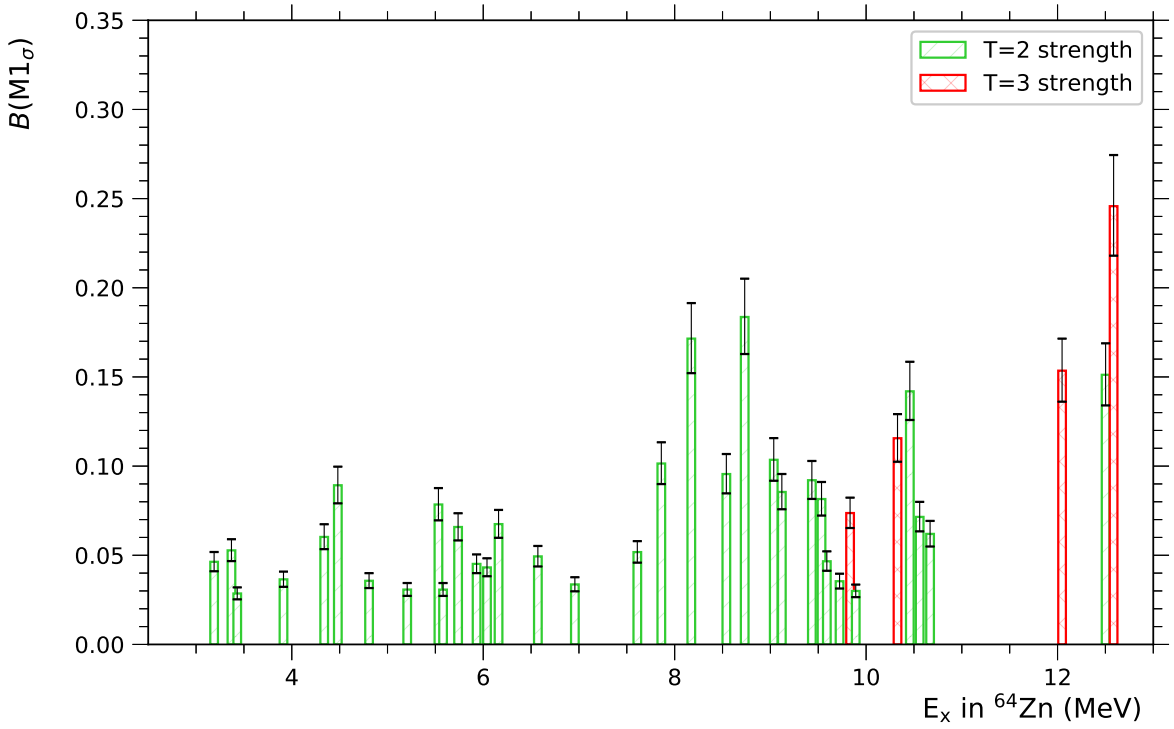

Figure 5.12: The $B(M1_\sigma)$ values calculated for the Spin-$M1$ states in the 4° ^{64}Zn spectrum.

6 Discussion and Summary

We combined the results of a ^{64}Zn(d,^{2}He)^{64}Cu, a ^{64}Zn(p,p')^{64}Zn, and a ^{64}Zn(^{3}He,t)^{64}Ga experiment to investigate the isospin structure of excited states in the isospin multiplet ^{64}Cu, ^{64}Zn, and ^{64}Ga. In the following sections, the results of each experiment will be described and the outcomes of their merged analysis will be summarized.

6.1 GT$^+$ Transitions from ^{64}Zn

The GT$^+$ transitions starting from ^{64}Zn were measured in a ^{64}Zn(d,^{2}He)^{64}Cu experiment at KVI in Groningen, The Netherlands, by Grewe *et al.* [53]. A description of the experiment is given in Chap. (1.7.2). In the analysis of the experimental data, GT$^+$ candidate states in the ^{64}Cu spectrum were selected through a comparison of their differential cross section with DWBA predictions. The selection of GT$^+$ states was cross-checked through a comparison with a ^{64}Ni(^{3}He,t)^{64}Cu spectrum [91]. Because of the isospin selection rules, the GT$^+$ transitions can only excite states with $T = 3$ in ^{64}Cu. The strengths of the transitions to the identified GT$^+$ states were calculated assuming the proportionality of the cross section and B(GT$^+$) values [see Eq. (1.7)]. The GT unit cross section in Eq. (1.7) was calibrated with respect to the cross section of the g.s. to g.s. GT$^+$ transition and the logft value of its reversed transition [90]. It should be noted that the cross section of the g.s. to g.s. GT$^+$ transition is rather small and, thus, the calibration can suffer from statistical and systematic error. The evaluated B(GT$^+$) values are shown in part (a) of Fig. (6.2). In addition, the spectrum measured in the ^{64}Zn(d,^{2}He)^{64}Cu reaction is shown in faint gray. The spectrum was scaled arbitrarily to match the height of the columns representing the B(GT$^+$) values. From the observed B(GT$^+$) values and the B(GT$^-$) values to analog states measured in ^{64}Ni(^{3}He,t)^{64}Cu [91], Grewe *et al.* [53] calculated the cumulative double Gamow-Teller matrix element $M^{(2\nu)}_{\mathrm{DGT}}$. The cumulative sum of the GT$^+$ strength $\sum B(\mathrm{GT}^+)$ was determined to be $1.604^{\pm 0.05(\mathrm{stat.})}_{\pm 0.25(\mathrm{sys.})}$ and the value of $\sum M^{(2\nu)}_{\mathrm{DGT}}$ was determined to be $0.41^{\pm 0.02(\mathrm{stat.})}_{\pm 0.04(\mathrm{sys.})}$. This is about one order of magnitude higher than the $\beta\beta$ matrix elements of similar studies, e.g., ^{48}Ca [92, 93] and ^{116}Cd

[94]. The extracted $B(\mathrm{GT}^+)$ and $B(\mathrm{GT}^-)$ values were compared with Shell-Model calculations using different effective interactions, such as KB3G, KB3Gmod, GXPF1, and KBF. The calculations performed with the GXPF1 and the KBF interactions gave a reasonable agreement with the experimental data. For the KB3G interaction, however, the proton gap had to be modified (KB3Gmod) to give acceptable results.

6.2 GT^- Transitions from ^{64}Zn

The GT^- transitions starting from ^{64}Zn were measured in a ^{64}Zn(^{3}He,t)^{64}Ga experiment at RCNP in Osaka, Japan. The experiment is described in Sec. (1.7.1). Because of the high energy-resolution achieved in the ^{64}Zn(^{3}He,t)^{64}Ga experiment, we were able to select GT^- candidate states by the angular distribution of their yields in the ^{64}Ga spectrum. We analyzed all states observed up to about 6 MeV. Above that energy, the level density increased and, for that reason, we were only able to investigate the pronounced states. Above 10.7 MeV, the level density became too high to analyze any individual states. We did, however, observe two smeared-out structures around 14 and 14.5 MeV, which we also accepted as GT candidates. The discussion on those structures is given in Sec. (6.3). Above the proton-separation threshold, the ^{64}Ga spectra suffered from a large background introduced by the three-body systematics of quasi-free scattering. We estimated the background distribution by a smooth function [88] and subtracted it from our spectra. The $B(\mathrm{GT}^-)$ values of the transitions to the selected GT^- states were calculated using Eq. (1.7). Here, we calibrated the GT unit cross section using an interpolated R^2 value [21] [see Sec. (1.2)]. The $B(\mathrm{GT}^-)$ values are shown in Fig. (6.2) (c). In addition, the corresponding ^{64}Zn(^{3}He,t)^{64}Ga spectrum is shown in faint gray. Note that the spectrum was scaled arbitrarily to match the height of the columns representing the $B(\mathrm{GT}^-)$ values. The GT^- strength distribution is rather fragmented in the region below 6 MeV. In the higher excitation-energy region, it appears that the strength is concentrated in two broad resonance-like structures, with their centers around 8 and 11 MeV. However, owing to the high level density, we were not able to analyze all states in this region.

Our collaborator, Michio Honma, calculated the transition strength of the GT^--type transitions starting from ^{64}Zn in a large-scale Shell-Model [49] calculation [95]. The calculations were performed with the GXPF1J interaction [50, 51, 52]. The results of the calculation are shown in Fig. (6.2) (d). Because the predicted level density is high, we separated the results with respect to the isospin T of the final state. By comparing

Figs. (6.2) (c) and (d) we see that the SM calculations show a good agreement for the transitions to the low-lying $T = 1$ states. Although a level-by-level comparison is difficult, the fragmentation and strength of states are well reproduced. At higher excitation energies, however, the strength distribution appears to be significantly overestimated by the SM. Comparing the experimental and theoretical strength distributions of the transitions to the $T = 2$ and $T = 3$ states, we observe similar features. In addition, the SM results also form two resonance-like structures around 8 MeV for the transitions to the $T = 1$ states and around 11 MeV for the $T = 2$ states. We also compared the experimental and theoretical strength distributions in terms of their cumulative sum $\sum B(\mathrm{GT}^+)$. Figure (6.1) shows that the $\sum B(\mathrm{GT}^+)$ distributions are rather similar up to about 7 MeV, when a quenching-factor of $(0.74)^2$ is included. Above this energy, however, the SM result largely overestimates our experimental results. The final value of the experimental $\sum B(\mathrm{GT}^+)$ at 10.7 MeV was determined to be 2.89(2).

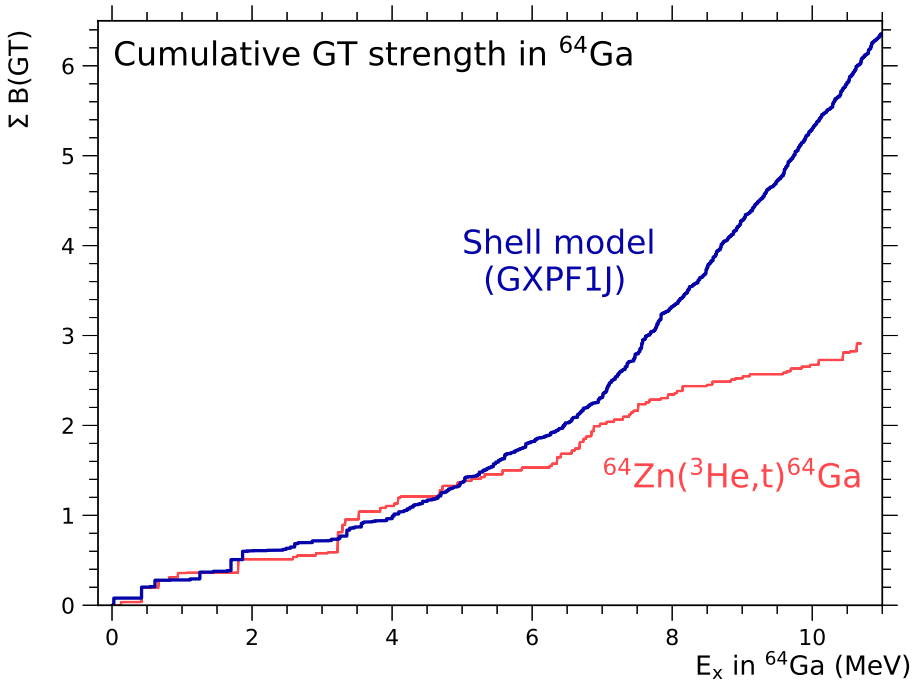

Figure 6.1: Comparison of the cumulative Gamow-Teller strength distribution from the ^{64}Zn(^{3}He,t)^{64}Ga experiment (red line) and the Shell-Model calculations (blue line) below 10.7 MeV. A quenching factor of $(0.74)^2$ is included in the SM result. The thickness of the experimental line (red) represents the error of the sum at any given point; however, the errors are too small to be recognizable. From [47].

We also compared our results to the outcome of (^{3}He,t) reaction experiments per-

formed on other $T_z = +2$ nuclei, i.e., ^{44}Ca [96], ^{48}Ti [97], ^{52}Cr [98], ^{56}Fe [99], and ^{60}Ni [100]. In the ^{44}Ca(^{3}He,t)^{44}Sc and ^{48}Ti(^{3}He,t)^{48}V measurements, the observed GT$^-$ strength was mainly concentrated in the lower E_x region below 6 MeV [96, 97]. On the other hand, in the measurements on ^{56}Fe and ^{60}Ni nuclei, the main part of the GT strength was found in the higher E_x region. It is suggested that this particular evolution of the GT strength distribution as a function of mass number A can be explained by the competition of the active isoscalar and isovector residual interactions [101].

6.3 Merged Analysis of GT$^+$ and GT$^-$ Transitions

Transitions to the $T_> = 3$ States

We compared the ^{64}Zn(d,^{2}He)^{64}Cu and the ^{64}Zn(^{3}He,t)^{64}Ga spectra and were able to find a good agreement between the strong states at 2.66 and 3.19 MeV in ^{64}Cu and the structures around 14.0 and 14.5 MeV in ^{64}Ga when the spectra were offset by $E_x \approx 11.31$ MeV $= 9.39 + E_x(^{64}\mathrm{Ga_{IAS}})$ [see Fig. (5.6))]. For that reason, we assume that these states are analog $T = 3$ states. The 2.66 MeV state in ^{64}Cu forms a doublet with the state at 2.78 MeV. Because these states could not be separately resolved in the ^{64}Zn(d,^{2}He)^{64}Cu experiment, we treated these states as one broad structure. To allow a comparison of the strength of the GT$^+$ and GT$^-$ transitions exciting the corresponding structures described above, we normalized the B(GT$^+$) values given in [53] by the ratio of the isospin CG coefficients. The B(GT$^-$) values were calculated assuming that all counts in the structures at 14.0 and 14.5 MeV in ^{64}Ga are related to the GT$^-$ transitions. We compared the $B(\mathrm{GT}^+)_{\mathrm{norm.}}$ and the B(GT$^-$) values [see Tab. (5.2)] and found a reasonable agreement of their average strength. It appears that the isospin symmetry structure in the isospin multiplet around ^{64}Zn is well established.

Sum Rule Limit

We calculated the limit of the available GT strength for GT$^-$- and GT$^+$-type transitions starting from ^{64}Zn using the Ikeda sum rule [27]. The sum rule is expressed as $\sum B(\mathrm{GT}_-) - \sum B(\mathrm{GT}_+) = 3(N - Z)$. For the GT transitions starting from ^{64}Zn, the neutron excess is 4, resulting in a $3(N - Z)$ value of 12. The results of the accumulated GT$^-$ and GT$^+$ strengths are summarized in Tab. (6.1). The obtained sum rule value of 1.29 corresponds to only $\approx 11\%$ of the expected sum rule limit (12). This small value can partly be explained by the analysis procedure of the ^{64}Zn(^{3}He,t)^{64}Ga experiment.

Table 6.1: Cumulative strength and sum rule limit of GT transitions starting from ^{64}Zn.

$\sum B(\mathrm{GT}^-)$	$\sum B(\mathrm{GT}^+)$	$3(N-Z)$ exp.	$3(N-Z)$ theo.
2.89(2)	$1.60^{\pm 0.05(\mathrm{stat})}_{\pm 0.25(\mathrm{sys})}$	1.29(26)	12

Because of the high level density, only strong states could be analyzed above 6 MeV and no isolated states were observed above 10.7 MeV. This can explain the missing strength to some extent. In addition, the background caused by the so-called quasi-free scattering was subtracted from the ^{64}Zn(^{3}He,t)^{64}Ga spectrum assuming a smooth function. If the assumed background distribution is overestimated, a decreased $\sum B(\mathrm{GT}^-)$ value is observed. In that sense, our result should be treated as a lower bound of the experimental sum rule value. On the other hand, as is described in Sec. (1.5.1), mechanisms like the formation of the $\Delta(1232)$-isobar and the mixing of high-lying $(2p, 2h)$ with low-lying $(1p, 1h)$ states can push the GT strength to high excitation energies. Further investigation in this field is needed. It would be interesting to see if such a mechanism can explain the sum rule deficiency [47].

6.4 $M1_\sigma$ Transitions from ^{64}Zn

The Spin-$M1$ transitions starting from the g.s. of ^{64}Zn were measured in a ^{64}Zn(p,p')^{64}Zn experiment performed at 200 MeV beam energy and small scattering angles, including 0°, at the iThemba LABS high-resolution facility in Cape Town, South Africa. To allow a level-by-level comparison with other experiments, we aimed for a high energy-resolution. By the application of dispersion-matching techniques to the beamline and the $K600$ spectrometer, we achieved an excellent energy resolution of $\Delta E = 35$ keV (FWHM). IE scattering experiments performed at 0° are difficult because the unscattered beam passes through the spectrometer along with the scattered particles. For that reason, the 0° spectrum suffers from a large instrumental background below 8 MeV. To measure excitations at lower excitation energies and obtain information on the angular distribution of excited states, measurements using the 4° facility of the $K600$ were performed. In this setting, the instrumental background was only observed below 2.5 MeV. The high-resolution spectra were reconstructed from the raw experimental data in a complex offline analysis. The procedure included the calibration of the raw detector signals, the selection of the events of interest over background events, and the correction of spec-

trometer aberration effects. The high-resolution spectra were energy calibrated by reference spectra with well-known excitations from ^{26}Mg, ^{12}C, and ^{14}N, taken under the same conditions. Instrumental and target-related background contributions were subtracted from the spectra. We compared the 0° and the 4° spectra to the ^{64}Zn(^{3}He,t)^{64}Ga and the ^{64}Zn(d,^{2}He)^{64}Cu spectra [see Fig. (5.6)]. The comparison revealed a good correspondence of the identified analog $T = 3$ states in ^{64}Cu and ^{64}Ga with the states at 12.047 and 12.584 MeV in the ^{64}Zn spectra, when an offset equal to the excitation energy of therespective IASs were taken into account. For that reason, we assign these new states in ^{64}Zn to be of $J^{\pi} = 1^{+}$, $T = 3$ Spin-$M1$ nature. States that showed an angular distribution similar to the $T = 3$ states were also selected as Spin-$M1$ candidates. In this way, a total of 20 new Spin-$M1$ 1^{+} candidate states in the 0° spectrum of ^{64}Zn were discovered. Comparison of the 4° ^{64}Zn(p,p')^{64}Zn spectrum and the ^{64}Zn(^{3}He,t)^{64}Ga spectrum revealed 19 additional states with corresponding excitation energies and relative cross sections. These states were also selected as Spin-$M1$ 1^{+} candidates. It is worth pointing out that in the region between 8 and 9 MeV we could select Spin-$M1$ states in the 0° spectrum not only from their angular distribution, but also from their coexistence in the ^{64}Zn(^{3}He,t)^{64}Ga spectrum. For three states that were selected as Spin-$M1$ candidates in the angular-distribution analysis, we could not find analog partners in ^{64}Ga. Therefore, these states were excluded from further analysis. Among the selected Spin-$M1$ candidates, we found a good agreement for three states with known 1^{+} states measured in the β decay of ^{64}Cu [81]. This is remarkable because these states were not considered in the preceding analysis and it is, therefore, evidence for the consistency of the applied analysis techniques. In addition, this also supports our assumption of good isospin symmetry being established in the isospin multiplet around ^{64}Zn.

We calculated the $M1_{\sigma}$ strength for all Spin-$M1$ candidates in the 0° and the 4° ^{64}Zn spectra using Eq. (1.11) assuming a good proportionality between the states' cross sections and $B(M1_{\sigma})$ values. To calibrate the $M1_{\sigma}$ unit cross section in Eq. (1.11), we used the averaged $B(\mathrm{GT}^{-})$and $B(\mathrm{GT}^{+})_{\mathrm{norm.}}$ values as $M1_{\sigma}$ standards. The strengths of $M1_{\sigma}$ states above 8 MeV were calculated from their cross sections in the 0° spectrum. For transitions to states below that energy, we used the cross section in the 4° spectrum. The $B(M1_{\sigma})$ values are shown in Fig. (6.2) (b). In addition, we show the 4° ^{64}Zn spectrum in faint gray. The spectrum was scaled arbitrarily to match the height of the columns representing the $B(\mathrm{GT}^{-})$ values.

Several states in our ^{64}Zn spectra could not be identified as being excited by Spin-$M1$ transitions. Because we also observe known 2^{+} and 1^{-} states in our spectra, it is expected

that the states that could not be related to Spin-$M1$ transitions are likely excited by $E1$ or $E2$ transitions. The $E1$ transitions are predominantly expected in the region of the PDR around 9 MeV. Recent random-phase approximation (RPA) calculations predict that $\approx 1\%$ of the $E1$ strength in ^{64}Zn splits from the GDR to the PDR [102]. In our spectrum, the expected PDR yield corresponds to the yield of three stronger states in the 9 MeV region. However, to identify the nature of the transitions to each state, additional experimental data are required.

6.5 Merged Analysis of $M1_\sigma$ and GT Transitions

To identify the Spin-$M1$ states with isospin $T = 3$, we compared the 0° ^{64}Zn(p,p')^{64}Zn with the ^{64}Zn(d,^{2}He)^{64}Cu spectrum. This way, we were able to find 4 pairs of $M1_\sigma$ and GT$^+$ states with corresponding excitation energies and strengths. These states were assigned the isospin value $T = 3$. The Spin-$M1$ candidates that could not be matched with GT$^+$ states were assigned $T = 2$. Owing to the high level density in ^{64}Zn, we were not able to find $M1_\sigma$ matches for the weaker GT$^+$ states in ^{64}Cu. Because the analog state of the g.s. of ^{64}Cu is expected at $\approx$ 9.39 MeV in ^{64}Zn, the $M1_\sigma$ states below that energy could be assigned the isospin $T = 2$. In addition, the analog GT$^-$ states of these states could also be assigned to $T = 2$. The GT$^-$ states in ^{64}Ga that could not be matched with $M1_\sigma$ states were assigned the isospin $T = 1$. Figure (6.2) shows the isospin and the strength of the GT$^+$, Spin-$M1$, and GT$^-$ transitions starting from ^{64}Zn. To show the analog structure of states, Figs. (6.2) (a), (b), and (c) are offset to each other by the excitation energy of the respective IAS. This way, analog states appear at the same position. In part (d) of Fig. (6.2), the results of Shell-Model calculations for the GT$^-$ transitions starting from ^{64}Zn are shown. Because the level density predicted by the Shell Model is high, we split Fig. (6.2) (d) in three parts with respect to the isospin of the states. In Tab. (8.1), we summarize the excitation energies, transition strengths and isospin values of the final states excited by GT$^+$, Spin-$M1$, and GT$^-$ transitions starting from ^{64}Zn. This table is complementary to Fig. (6.2). The states are ordered by the (estimated) excitation energy of their GT$^-$ analog state in ^{64}Ga (not shown).

6.6 Outlook

In the previous sections, we summarized the merged analysis of analog GT and $M1_\sigma$ transitions starting from ^{64}Zn. We found that there is a $\approx$ 40% deviation between the

$B(\mathrm{GT}^+)$ and the $B(\mathrm{GT}^-)$ values for the analog transitions to the observed $T = 3$ states. In the present discussion, we derived relative $B(\mathrm{GT}^-)$ values from a mass-dependent proportionality between the Fermi and GT cross sections. In order to calculate absolute $B(\mathrm{GT}^-)$ values, the normalization from $B(\mathrm{GT})$ values measured in β decay is required. These values can be obtained from the β decay of ^{64}Se, which is the mirror of ^{64}Zn. ^{64}Se is located at the proton dripline and has been observed for the first time in a ^{9}Be(^{78}Kr,X) reaction at NSCL [103]. During the experiment, a total of 4 events related to ^{64}Se were detected at the A1900 fragment separator in a beamtime of 32 hours. To obtain sufficient statistics to observe individual transitions, we measured the decay of ^{64}Se using the BigRIPS fragment separator at RIKEN in Tokyo, Japan in 2015. The recorded data are currently under evaluation by the B. Rubio group in Valencia. It will be interesting to see if $B(\mathrm{GT})$ values from the decay of ^{64}Se can eliminate the strength difference between the analog GT^+ and GT^- transitions from ^{64}Zn. Furthermore, the results will indicate how well the isospin symmetry structure is established between ^{64}Zn and its exotic mirror partner ^{64}Se.

We would also like to compare our data with the EM $M1$ transitions starting from ^{64}Zn. In this way, we will be able to determine a value for the contribution of the meson exchange current R_{MEC}. Additionally, we can investigate the constructive and destructive contributions of the IS and IV terms in the EM $M1$ operator for each analog transition. The EM $M1$ transitions have been measured in a ^{64}Zn(e,e') experiment [104]; however, the study focused on the evaluation of giant-resonance phenomena. It is, therefore, desirable to perform an (e,e') experiment with the focus on individual particle-hole-type excitations.

By combining the results of the ^{64}Se β decay and EM $M1$ transitions starting from ^{64}Zn with the results of the present work, we can get a detailed overview of the isospin symmetry structure in $A = 64$ isobars.

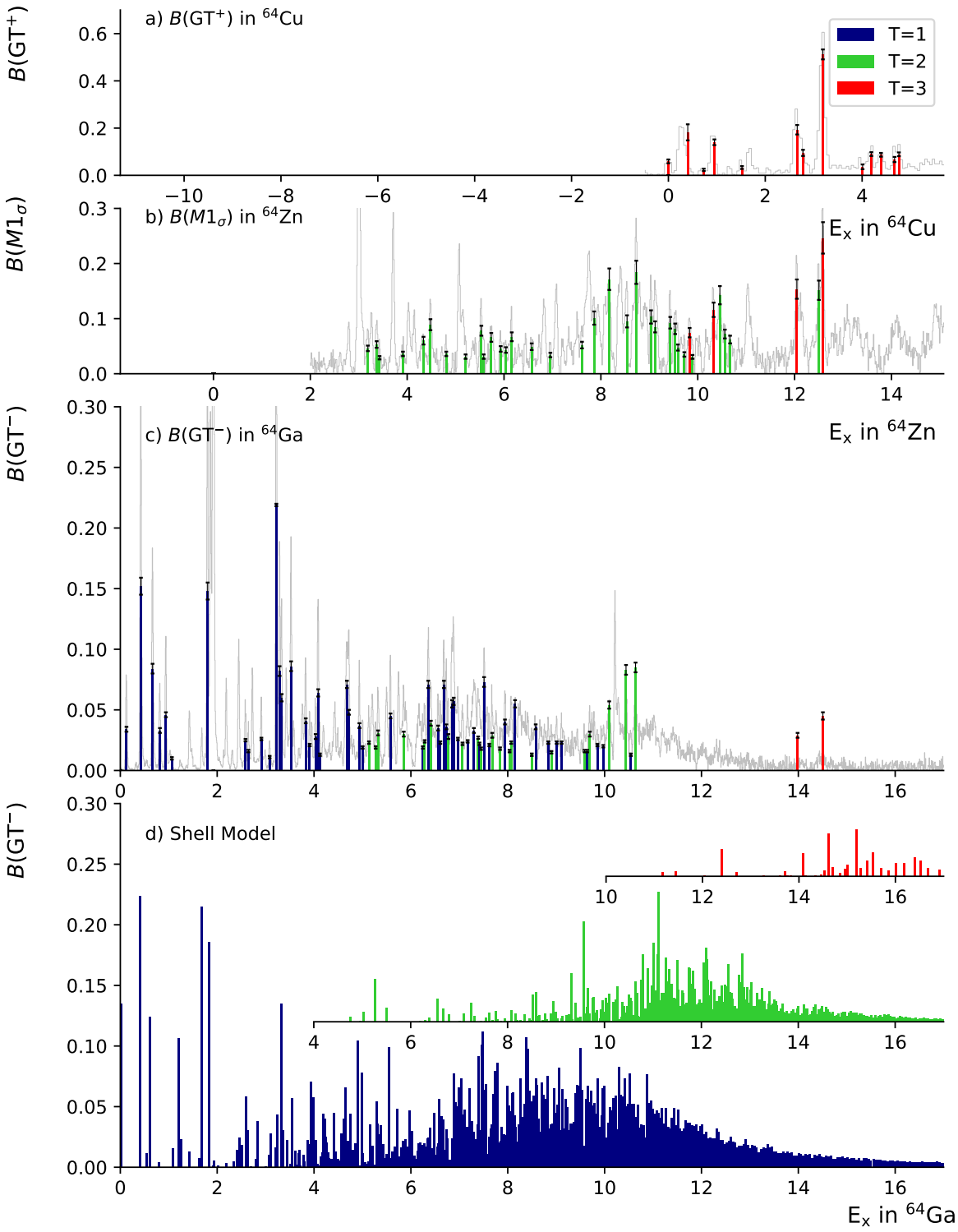

Figure 6.2: Comparison of the $B(\mathrm{GT}^+)$, $B(M1_\sigma)$, and $B(\mathrm{GT}^-)$ values measured in ^{64}Zn(d,^{2}He)^{64}Cu, ^{64}Zn(p,p')^{64}Zn, and ^{64}Zn(^{3}He,t)^{64}Ga reaction experiments, respectively. The results of Shell-Model calculations are also shown. The respective spectra are shown in faint gray. The height of part a) and b) are aligned by the height of the $T = 3$ states (red). The height of par b) and c) & d) are aligned by the height of the $T = 2$ states (green).

7 Conclusion

> "Sometimes science is more art than science, Morty. A lot of people don't get that."
> - Rick Sanches, Rick and Morty (Season 1, Episode 6)

In this work, we investigated the isospin symmetry structure in the isospin multiplet ^{64}Ga, ^{64}Zn, and ^{64}Cu. For that purpose, we performed a ^{64}Zn(p,p')^{64}Zn experiment at 200 MeV beam energy and small scattering angles, including 0°, at the high-resolution facility of iThemba LABS in Cape Town, South Africa. Through the application of beam-matching techniques to the spectrometer system, we were able to achieve an excellent energy resolution of 35 keV (FWHM). This is the first time a high-resolution ^{64}Zn spectrum up to high excitation energies was recorded. As a result of the good resolution, we were able to investigate individual states in our spectra. We selected Spin-$M1$ state candidates in the 0° spectrum by their angular distribution. The strengths of the transitions to these states were calculated assuming the proportionality of the cross sections and $B(M1_\sigma)$ values. The good energy resolution allowed us to compare our data with the results of a ^{64}Zn(d,^{2}He)^{64}Cu and a ^{64}Zn(^{3}He,t)^{64}Ga experiment using a state-by-state approach. In this procedure, we discovered many unknown Spin-$M1$, $J^\pi = 1^+$ states and were able to match them with their analog partners in ^{64}Cu and ^{64}Ga. In addition, we were able to identify the isospin T value of analog states by comparison of the strengths of analog transitions exciting them. The analysis revealed that the isospin symmetry is established remarkably well in the isospin mutliplet consisting of ^{64}Ga, ^{64}Zn, and ^{64}Cu. It is impressive how Spin-$M1$ and GT transitions induced in various experiment types are complementary in the study of the spin-isospin symmetry structure of atomic nuclei.

8 Appendix

8.1 Derivation of Beam-Matching Conditions

Following the notation in [70], any arbitrary charged particle inside the spectrometer system can be represented by the vector $\mathbf{X}$ with

$$\mathbf{X} = \begin{bmatrix} x \\ \theta \\ y \\ \phi \\ l \\ \delta \end{bmatrix}, \tag{8.1}$$

where the following definitions hold:

x = the horizontal displacement of the arbitrary ray with respect to the assumed central trajectory,

θ = the angle this ray makes in the horizontal plane with respect to the assumed central trajectory,

y = the vertical displacement of the ray with respect to the assumed central trajectory,

ϕ = the vertical angle of the ray with respect to the assumed central trajectory,

l = the path-length difference between the arbitrary ray and the central trajectory, and

$\delta = \Delta p/p$ is the fractional momentum deviation of the ray from the assumed central trajectory.

For the derivation of the matching conditions, it is sufficient to consider the components x, θ, and δ, of $\mathbf{X}$. At the source point of the spectrometer system, the particle is described by $\mathbf{x_0} = (x_0, \theta_0, \delta_0)$ [55]. Downstream from the source point, $\mathbf{x_0}$ is transformed by the beamline transport matrix $\mathbf{B} = (b_{\mu\nu})$ to $\mathbf{x_1} = (x_1, \theta_1, \delta_1)$:

$$\mathbf{x_1} = \mathbf{B}\mathbf{x_0} \tag{8.2}$$

$$= \begin{pmatrix} b_{11} & b_{12} & b_{16} \\ b_{21} & b_{22} & b_{26} \\ 0 & 0 & 1 \end{pmatrix} \begin{pmatrix} x_0 \\ \theta_0 \\ \delta_0 \end{pmatrix} \tag{8.3}$$

$$= \begin{pmatrix} b_{11}x_0 + b_{12}\theta_0 + b_{16}\delta_0 \\ b_{21}x_0 + b_{22}\theta_0 + b_{26}\delta_0 \\ \delta_0 \end{pmatrix} \tag{8.4}$$

$$= \begin{pmatrix} x_1 \\ \theta_1 \\ \delta_1 \end{pmatrix} \tag{8.5}$$

Here, we use $\mu, \nu = 1, 2, 6$ with respect to the indices of x, θ, and δ in $\mathbf{X}$. It should be noted that $\delta_1 = \delta_0$, because the beamline does not change the momentum of the beam particles.

In a real spectrometer system, $\mathbf{x_1}$ corresponds to the coordinates of the beam particle entering the target chamber. The interaction with the target is described by the function T, which handles the reaction angle α and the target angle ϕ_T. T is of the form

$$T = \cos(\alpha - \phi_\mathrm{T}) / \cos\phi_\mathrm{T}, \tag{8.6}$$

which acts on the coordinate x_1 as $x_2 = Tx_1$. In addition to the position component, the angle component of $\mathbf{x_1}$ is changed by the scattering angle Θ of the nuclear reaction with $\Theta = \theta_2 - \theta_1$ and, therefore,

$$\theta_2 = \theta_1 + \Theta. \tag{8.7}$$

Lastly, the momentum component δ_1 is also changed in the projectile-target interaction by

$$\delta_2 = K(\theta_2 - \theta_1) + C\delta_1 \tag{8.8}$$

$$= K\Theta + C\delta_0 \tag{8.9}$$

In Eq. (8.8) C and K carry the information on the reaction kinematics with:

$$K = \frac{1}{P_{\text{out}}} \frac{\delta P_{\text{out}}}{\alpha} \text{ and } C = \frac{\delta P_{\text{out}}}{\delta P_{\text{in}}} \frac{P_{\text{in}}}{P_{\text{out}}}. \tag{8.10}$$

Finally, the transformation of the target acting on the incoming particle can be written as:

$$\mathbf{x_2} = \begin{pmatrix} Tx_1 \\ \theta_1 + \Theta \\ K\Theta + C\delta_0 \end{pmatrix} \tag{8.11}$$

$$= \begin{pmatrix} b_{11}Tx_0 + b_{12}T\theta_0 + b_{16}T\delta_0 \\ b_{21}x_0 + b_{22}\theta_0 + b_{26}\delta_0 + \Theta \\ K\Theta + C\delta_0 \end{pmatrix}. \tag{8.12}$$

The last transformation that has to be considered is the influence of the spectrometer on the beam particle. Analogous to the transport matrix $\mathbf{B}$ of the beam, the spectrometer transport matrix is $\mathbf{S}$ and the coordinates in the focal plane are given by:

$$\mathbf{x}_{\text{fp}} = \mathbf{S}\mathbf{x_2} \tag{8.13}$$

$$= \begin{pmatrix} s_{11} & s_{12} & s_{16} \\ s_{21} & s_{22} & s_{26} \\ s_{61} & s_{62} & s_{66} \end{pmatrix} \begin{pmatrix} b_{11}Tx_0 + b_{12}T\theta_0 + b_{16}T\delta_0 \\ b_{21}x_0 + b_{22}\theta_0 + b_{26}\delta_0 + \Theta \\ K\Theta + C\delta_0 \end{pmatrix} \tag{8.14}$$

Just like the beamline, the spectrometer does not change the total momentum of the beam particle and so $s_{61} = s_{62} = 0$ and $s_{66} = 1$. The coordinates of the particle at the focal plane position $\mathbf{x}_{\text{fp}}$ can thus be simplified as functions of the coordinates at the

source point [55, 72, 105]:

$$\begin{aligned} x_{\mathrm{fp}} &= x_0(s_{11}b_{11}T + s_{12}b_{21}) \\ &+ \theta_0(s_{11}b_{12}T + s_{12}b_{22}) \\ &+ \delta_0(s_{11}b_{16}T + s_{12}b_{26} + s_{16}C) \\ &+ \Theta(s_{12} + s_{16}K) \end{aligned}$$

$$\begin{aligned} \theta_{\mathrm{fp}} &= x_0(s_{21}b_{11}T + s_{22}b_{21}) \\ &+ \theta_0(s_{21}b_{12}T + s_{22}b_{22}) \\ &+ \delta_0(s_{21}b_{16}T + s_{22}b_{26} + s_{26}C) \\ &+ \Theta(s_{22} + s_{16}K) \end{aligned}$$

$$\delta_{\mathrm{fp}} = \delta_2 = K\Theta + C\delta_0$$

The transformations of the complete spectrometer system starting from the source point $\mathbf{x_0}$ can be summarized by (inspired by [26, 55]):

$$\mathbf{B}\begin{pmatrix} x_0 \\ \theta_0 \\ \delta_0 \end{pmatrix} \rightarrow \begin{pmatrix} x_1 \\ \theta_1 \\ \delta_0 \end{pmatrix} \Rightarrow \mathbf{T}(\begin{pmatrix} x_1 \\ \theta_1 \\ \delta_0 \end{pmatrix}) \rightarrow \begin{pmatrix} x_2 \\ \theta_2 \\ \delta_2 \end{pmatrix} \Rightarrow \mathbf{S}\begin{pmatrix} x_2 \\ \theta_2 \\ \delta_2 \end{pmatrix} \rightarrow \begin{pmatrix} x_{\mathrm{fp}} \\ \theta_{\mathrm{fp}} \\ \delta_{\mathrm{fp}} \end{pmatrix}$$

beamline transf.	in front of target	target transf.	after target	spectr. transf.	at K600 focal plane

8.2 Lineshape Correction

When the incident protons are in-elastically scattered, the target nuclei can be excited and so the beam protons loose energy. On top of that, the target nuclei are recoiled in the scattering process. This recoil causes an additional energy loss for the protons depending on the scattering angle. The transferred recoil energy is zero for 0° scattering and is largest at 180° (complete back scattering). After interacting with the target, the beam protons are dispersed by the $K600$ spectrometer according to their momentum (energy). Although, the recoil energies are small compared to the energy transferred in a nuclear reaction, the effect contributes to the position of the protons in the focal plane. Therefore, the spectral line of a nuclear excitation is distorted with respect to the scattering angle of the protons. In addition to the recoil effect, the aberration

of the $K600$ magnetic field introduces another distortion of the spectral lines in the focal plane, which acts on top of the recoil distortion. Because the excitation energy spectrum is made by a projection of the spectral lines to the position axis, distortions of the spectral lines decrease the energy resolution of the spectrum. In order to maintain the high energy resolution achieved through the application of dispersion matching, the distortion of the spectral lines have to be removed. An illustration of the correction of spectral line distortions is given in Fig. (8.1). In Fig. (8.1) the correction function F' is

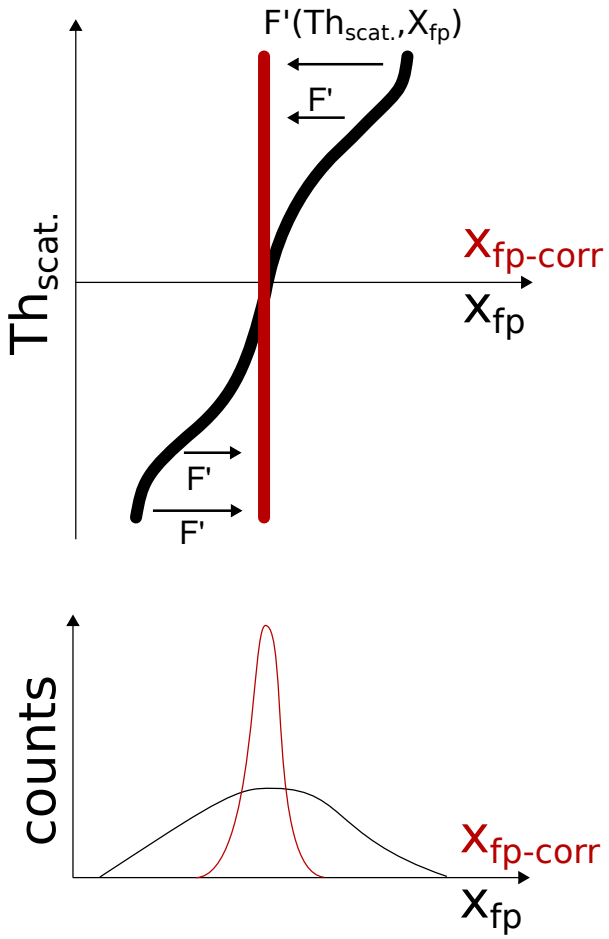

Figure 8.1: Illustration of the effect of the spectral line correction onto the resolution of the spectrum.

a polynomial function of Θ_{scat} and $\mathrm{X_{fp}}$, which is of the form of Eq. (8.15).

$$\mathrm{X_{fp-corr}} = \sum_i \sum_j \mathrm{par}_{i,j} \cdot {\Theta_{\mathrm{scat}}}^i \cdot {\mathrm{X_{fp}}}^j, \tag{8.15}$$

where $par_{i,j}$ are the correction parameters. To determine these parameters it is necessary to investigate the lineshape of each spectral line in the spectrum. Figure (8.2) shows an example of the lineshape investigation of the 10.647 MeV [80] line in ^{26}Mg.

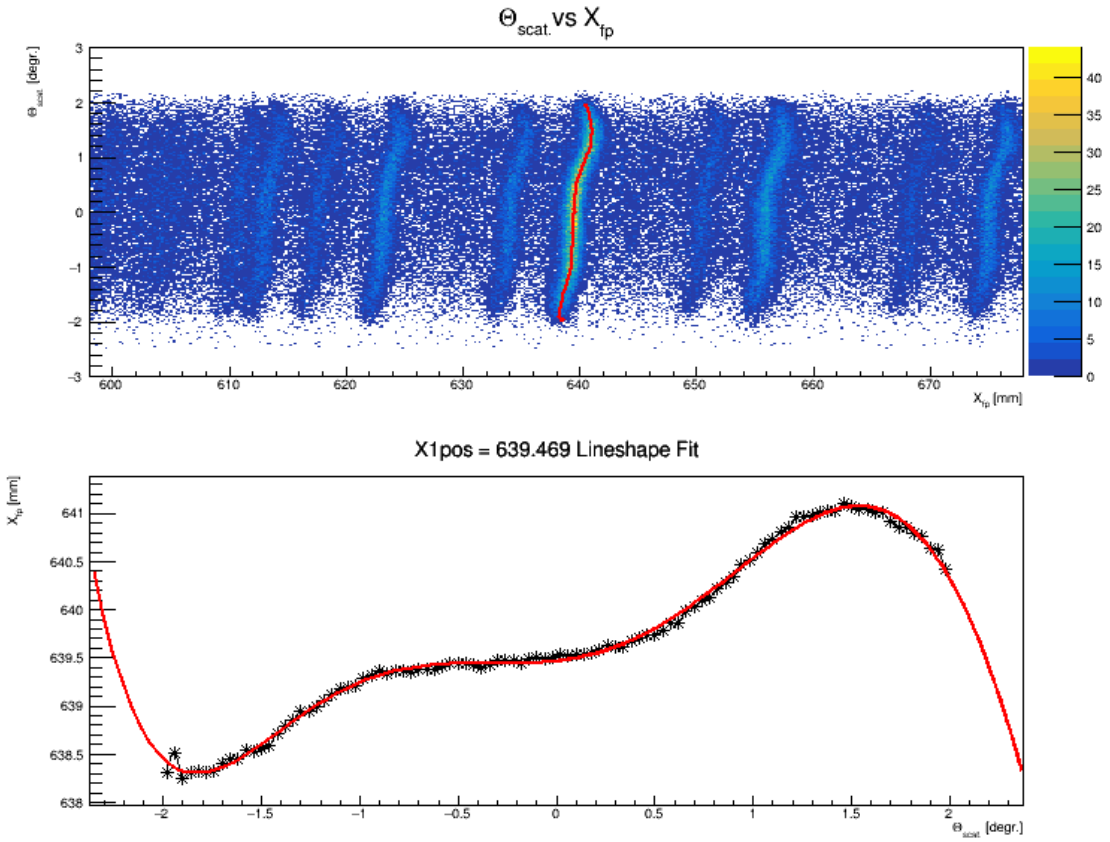

Figure 8.2: Image of the investigation of the 10.647 MeV [80] spectral line. Top: The spectral lines in the Θ_{scat} vs. X_{fp} plane of ^{26}Mg. The red line is composed of points along the 10.647 MeV spectral line. Bottom: The black points correspond to the red line in the top figure. The red line is a polynomial fit to the black points. Note that the Θ_{scat} and X_{fp} axis are interchanged compared to the top figure.

In the top part of Fig. (8.2), the spectral lines in the Θ_{scat} vs. X_{fp} plane of the ^{26}Mg spectrum are shown. The red line is composed of points along the spectral line. In bottom part of Fig. (8.2), the Θ_{scat} and X_{fp} axis are interchanged. Here, the black points correspond to the red line in the top part of the figure. The red line in the bottom plot is a fit of a polynomial function to these points. This procedure is repeated for all spectral lines in the spectrum to obtain their linefit parameters.

In order to obtain the correction parameters of Eq. (8.15) we solve the linear system:

$$\boldsymbol{A}\hat{p} = \hat{y}, \tag{8.16}$$

where $\boldsymbol{A}$ is a matrix containing the ${\Theta_{\mathrm{scat}}}^{i}{\cdot}{\mathrm{X_{fp}}}^{j}$ values for $(\Theta_{\mathrm{scat}}, \mathrm{X_{fp}})$ points along the spectral lines, $\hat{y}$ is the desired destination along a straight line for the respective $(\Theta_{\mathrm{scat}}, \mathrm{X_{fp}})$ point and $\hat{p}$ is a vector containing the correction parameters. By solving Eq. (8.16) for $\hat{p}$, we can obtain the parameters in Eq. (8.15). Through this method the distortion of spectral lines can be corrected if the target nucleus has strong isolated lines, spread across the greater part of the focal plane.

In the present experiment we aimed to correct the spectral line distortions in ^{64}Zn. Because the level density is very high and ^{64}Zn has only a few weak spectral lines, we could not obtain the correction parameters directly. Therefore, we combined spectral lines from ^{26}Mg, ^{12}C and ^{14}N to calculate the correction parameters for ^{64}Zn. As described above, it is crucial to consider the contribution of the mass dependent kinematic line distortion. This kinematic distortion inhibits us from directly combining spectral lines from different target nuclei, for the calculation of the correction parameters $\mathrm{par}_{i,j}$. However, the kinematics involved in nuclear scattering are well-understood and the kinematic distortions can be calculated by software. Here, we used the computer code Relkin [77] with an updated mass table to perform kinematic calculations. We calculated the recoil energies in small angle steps along each spectral from ^{26}Mg, ^{12}C and ^{14}N. The resulting points were fitted using second order polynomials. This way we obtained the kinematic contribution to the spectral line distortions. As illustrated in Fig. (8.3) (a), by *subtracting* the kinematic distortion polynomials from the initially distorted spectral lines, the kinematic recoil distortion was removed. Through this procedure, the distortion of the spectral line polynomials is reduced to contain the $K600$ aberration only. Similarly, we used Relkin to calculate the kinematic distortions in ^{64}Zn for the spectral lines obtained from ^{26}Mg, ^{12}C and ^{14}N. The obtained kinematic distortions were then *added* to the respective spectral line [see Fig. (8.3) (b)]. This way, the spectral lines from ^{26}Mg, ^{12}C and ^{14}N can be transformed to act as spectral lines from ^{64}Zn. By combining the transformed spectral lines and solving Eq. (8.15), the correction parameters for the desired target nucleus (here ^{64}Zn) can be determined, even when no strong spectral lines are available in the respective spectrum.

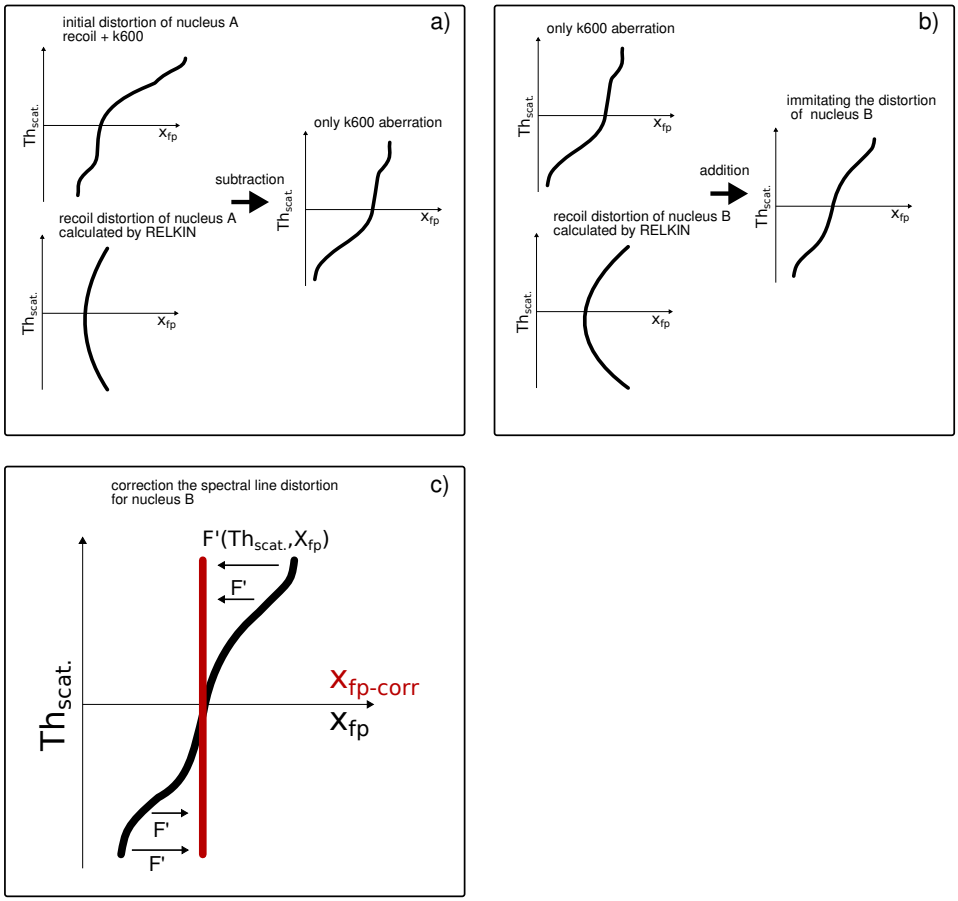

Figure 8.3: Illustration of the spectral line correction including kinematic recoil corrections. Here, spectral lines from nucleus A are used to correct the distortions in nucleus B. a) Subtraction of the kinematic effect of the target nucleus (A) to reduce the spectral line distortion to the $K600$ aberration. b) Addition of the kinematic effect of the nucleus to be corrected (B), to make the spectral line from A to act as spectral lines from B. c) Correction of the resulting spectral line distortion.

8.3 Spin-Isospin States in ^{64}Cu, ^{64}Zn, and ^{64}Ga

Table 8.1: The excitation energies and transitions strength of all $\sigma\tau$ type transitions starting from ^{64}Zn are shown. The GT$^+$ states were measured in a ^{64}Zn(d,^{2}He)^{64}Cu reaction experiment by Grewe *et al.* [53]. The $M1_\sigma$ states were measured in a ^{64}Zn(p,p')^{64}Zn reaction experiment. Their analysis is the major concern of the present work. The GT$^-$ states were measured in a ^{64}Zn(^{3}He,t)^{64}Ga reaction experiment and analyzed as part of [22, 47]. The isospin T quantum number evaluated in this work are shown in the right-most column.

^{64}Zn(d,^{2}He)^{64}Cu			^{64}Zn(p,p')^{64}Zn		^{64}Zn(^{3}He,t)^{64}Ga			
E_x	$B(GT)_p$	$\Delta B(GT)_p$	E_x	$B(M1_\sigma)$	E_x	$B(GT)_m$	$\Delta B(GT)_m$	Isospin
					0.127	0.034	±0.002	1
					0.426	0.152	±0.007	1
					0.666	0.084	±0.004	1
					0.818	0.033	±0.002	1
					0.941	0.046	±0.002	1
					1.065	0.01	±0.001	1
					1.803	0.148	±0.007	1
					1.923	IAS		2
					2.585	0.025	±0.001	1
					2.645	0.016	±0.001	1
					2.913	0.026	±0.001	1
					3.084	0.011	±0.001	1
					3.222	0.219	±0.001	1
					3.289	0.082	±0.004	1
					3.332	0.06	±0.003	1
					3.527	0.086	±0.004	1

Table 8.1 – continued from previous page

^{64}Zn(d,^{2}He)^{64}Cu			^{64}Zn(p,p')^{64}Zn		^{64}Zn(^{3}He,t)^{64}Ga			
E_x	$B(GT)_p$	$\Delta B(GT)_p$	E_x	$B(M1_\sigma)$	E_x	$B(GT)_m$	$\Delta B(GT)_m$	Isospin
					3.829	0.041	±0.002	1
					3.911	0.021	±0.001	1
					4.033	0.028	±0.002	1
					4.086	0.064	±0.003	1
					4.121	0.013	±0.001	1
					4.679	0.071	±0.003	1
					4.721	0.048	±0.002	1
					4.937	0.037	±0.002	1
					5.004	0.019	±0.001	1
			3.188	$0.046^{+0.005}_{-0.005}$	5.134	0.023	±0.001	2
			3.43	$0.029^{+0.003}_{-0.003}$	5.272	0.019	±0.001	2
			3.37	$0.053^{+0.006}_{-0.006}$	5.322	0.031	±0.002	2
					5.578	0.045	±0.002	1
			3.913	$0.036^{+0.004}_{-0.004}$	5.853	0.03	±0.002	2
					6.247	0.019	±0.001	1
			4.338	$0.06^{+0.007}_{-0.007}$	6.285	0.024	±0.001	2
					6.359	0.071	±0.003	1
			4.481	$0.089^{+0.01}_{-0.01}$	6.412	0.039	±0.002	2
					6.562	0.035	±0.002	1
					6.608	0.023	±0.001	1
					6.682	0.071	±0.003	1

Table 8.1 – continued from previous page

^{64}Zn(d,^{2}He)^{64}Cu			^{64}Zn(p,p')^{64}Zn		^{64}Zn(^{3}He,t)^{64}Ga			
E_x	$B(\mathrm{GT})_p$	$\Delta B(\mathrm{GT})_p$	E_x	$B(M1_\sigma)$	E_x	$B(\mathrm{GT})_m$	$\Delta B(\mathrm{GT})_m$	Isospin
					6.733	0.036	±0.002	1
			4.807	$0.036^{+0.004}_{-0.004}$	6.774	0.028	±0.002	2
					6.85	0.055	±0.003	1
					6.884	0.057	±0.003	1
					6.971	0.026	±0.001	1
			5.206	$0.031^{+0.004}_{-0.004}$	7.065	0.022	±0.001	2
					7.173	0.024	±0.001	1
					7.301	0.033	±0.002	1
			5.532	$0.078^{+0.009}_{-0.009}$	7.389	0.027	±0.001	2
					7.416	0.022	±0.001	1
			5.58	$0.031^{+0.004}_{-0.004}$	7.45	0.018	±0.001	2
					7.511	0.073	±0.004	1
					7.619	0.021	±0.001	1
			5.737	$0.066^{+0.008}_{-0.008}$	7.679	0.029	±0.002	2
			5.931	$0.045^{+0.005}_{-0.005}$	7.841	0.018	±0.001	2
					7.942	0.04	±0.002	1
			6.039	$0.043^{+0.005}_{-0.005}$	8.037	0.016	±0.001	2
			6.16	$0.067^{+0.008}_{-0.008}$	8.07	0.023	±0.001	2
					8.151	0.055	±0.003	1
			6.571	$0.049^{+0.006}_{-0.006}$	8.496	0.013	±0.001	2
					8.577	0.036	±0.002	1

Table 8.1 – continued from previous page

^{64}Zn(d,^{2}He)^{64}Cu			^{64}Zn(p,p')^{64}Zn		^{64}Zn(^{3}He,t)^{64}Ga			
E_x	$B(GT)_p$	$\Delta B(GT)_p$	E_x	$B(M1_\sigma)$	E_x	$B(GT)_m$	$\Delta B(GT)_m$	Isospin
					8.838	0.023	±0.001	1
			6.957	$0.034^{+0.004}_{-0.004}$	8.902	0.015	±0.001	2
					9.01	0.023	±0.001	1
					9.112	0.023	±0.001	1
			7.61	$0.052^{+0.006}_{-0.006}$	9.586	0.016	±0.001	2
					9.641	0.016	±0.001	1
			7.861	$0.101^{+0.012}_{-0.012}$	9.695	0.03	±0.002	2
					9.851	0.021	±0.001	1
					9.973	0.02	±0.001	1
			8.174	$0.171^{+0.02}_{-0.019}$	10.095	0.054	±0.003	2
			8.54	$0.095^{+0.011}_{-0.011}$	10.442	0.083	±0.004	2
					10.544	0.013	±0.001	1
			8.731	$0.152^{+0.018}_{-0.017}$	10.639	0.085	±0.004	2
			9.035	$0.095^{+0.011}_{-0.011}$				2
			9.12	$0.074^{+0.009}_{-0.008}$				2
0.0	0.059	±0.008						3
			9.433	$0.107^{+0.012}_{-0.012}$				2
			9.534	$0.095^{+0.011}_{-0.011}$				2
			9.59	$0.065^{+0.008}_{-0.007}$				2
			9.723	$0.034^{+0.004}_{-0.004}$				2
0.4	0.182	±0.034	9.832	$0.077^{+0.009}_{-0.009}$				3

Table 8.1 – continued from previous page

^{64}Zn(d,^{2}He)^{64}Cu			^{64}Zn(p,p')^{64}Zn		^{64}Zn(^{3}He,t)^{64}Ga			
E_x	$B(\mathrm{GT})_p$	$\Delta B(\mathrm{GT})_p$	E_x	$B(M1_\sigma)$	E_x	$B(\mathrm{GT})_m$	$\Delta B(\mathrm{GT})_m$	Isospin
			9.892	$0.032^{+0.004}_{-0.004}$				2
0.73	0.023	±0.005						3
0.95	0.14	±0.012	10.328	$0.138^{+0.016}_{-0.016}$				3
			10.457	$0.155^{+0.018}_{-0.017}$				2
			10.56	$0.071^{+0.008}_{-0.008}$				2
			10.668	$0.055^{+0.007}_{-0.006}$				2
1.52	0.033	±0.006						3
2.66	0.193	±0.02	12.047	$0.137^{+0.016}_{-0.015}$	13.985	0.029	±0.002	3
2.78	0.095	±0.013						3
			12.502	$0.151^{+0.018}_{-0.017}$				2
3.19	0.512	±0.021	12.586	$0.273^{+0.032}_{-0.031}$	14.507	0.045	±0.003	3
4.01	0.036	±0.01						3
4.19	0.09	±0.008						3
4.39	0.087	±0.008						3
4.67	0.067	±0.011						3
4.76	0.089	±0.008						3

Bibliography

[1] A. Bohr and B. R. Mottelson, *Nuclear structure*, Vol. 1 (Benjamin,New York, 1969).

[2] W. Heisenberg, Z. Phys. **77**, 1 (1932).

[3] D. Warner, M. Bentley, and P. van Isacker, Nature Physics , 311–318 (2006).

[4] K. S. Krane, *Introductory nuclear physics* (Wiley, New York, NY, 1988).

[5] E. Wigner, Phys. Rev. **51**, 106 (1937).

[6] E. Fermi, Z. Phys. **88**, 161–177 (1934).

[7] G. Gamow and E. Teller, Phys. Rev. **49**, 895 (1936).

[8] M. Harakeh and A. Woude, *Giant Resonances: Fundamental High-frequency Modes of Nuclear Excitation*, Oxford science publications (Oxford University Press, 2001).

[9] J. Hardy and I. Towner, Phys. Rev. C **79**, 055502 (2009).

[10] J. Hardy and I. Towner, Nucl. Phys. News **16**, 11 (2006).

[11] Y. Fujita, VI European Summer School on Experimental Nuclear Astrophysics (2011).

[12] S. Hanna and D. Wilkinson, *Isospin in nuclear physics* (Amsterdam : North Holland Pub. Co, 1970).

[13] H. Morinaga and T. Yamazaki, *In-beam gamma-ray spectroscopy* (North-Holland Pub. Co, 1976).

[14] H. Ejiri and M. d. Voigt, *Gamma-ray and electron spectroscopy in nuclear physics* (Oxford: Clarendon Press, 1976).

[15] Y. Fujita, B. Rubio, and W. Gelletly, Prog. Part. Nucl. Phys. **66**, 549 (2011).

[16] A. R. Edmonds, *Angular Momentum in Quantum Mechanics* (1960).

[17] L. Zamick and D. C. Zheng, Phys. Rev. C **37**, 1675 (1988).

[18] W. G. Love and M. A. Franey, Phys. Rev. C **24**, 1073 (1981).

[19] F. Petrovich and W. Love, Nucl. Phys. A **354**, 499 (1981).

[20] C. D. Goodman, C. A. Goulding, M. B. Greenfield, J. Rapaport, D. E. Bainum, C. C. Foster, W. G. Love, and F. Petrovich, Phys. Rev. Lett. **44**, 1755 (1980).

[21] T. Taddeucci, C. Goulding, T. Carey, R. Byrd, C. Goodman, C. Gaarde, J. Larsen, D. Horen, J. Rapaport, and E. Sugarbaker, Nucl. Phys. A **469**, 125 (1987).

[22] F. Diel, Masters Thesis: Study of $T_z = +2 \rightarrow +1$ Gamow-Teller transitions in a ^{64}Zn(^{3}He,t)^{64}Ga reaction. **Unpublished** (Cologne, 2015).

[23] F. Osterfeld, Rev. Mod. Phys. **64**, 491 (1992).

[24] G. M. Crawley, N. Anantaraman, A. Galonsky, C. Djalali, N. Marty, M. Morlet, A. Willis, J. C. Jourdain, and P. Kitching, Phys. Rev. C **26**, 87 (1982).

[25] Y. Fujita, B. A. Brown, H. Ejiri, K. Katori, S. Mizutori, and H. Ueno, Phys. Rev. C **62**, 044314 (2000).

[26] L. M. Donaldson, Ph.D. thesis, Faculty of Science, University of the Witwatersrand (2016).

[27] K. Ikeda, S. Fujii, and J. Fujita, Phys. Lett. **3**, 271 (1963).

[28] M. Ichimura, H. Sakai, and T. Wakasa, Prog. Part. Nucl. Phys. **56**, 446 (2006).

[29] T. Wakasa, H. Sakai, H. Okamura, H. Otsu, S. Fujita, S. Ishida, N. Sakamoto, T. Uesaka, Y. Satou, M. B. Greenfield, and K. Hatanaka, Phys. Rev. C **55**, 2909 (1997), and references therin.

[30] W. Bothe and W. Gentner, Z. Phys **71**, 236 (1937).

[31] W. Kuhn, Z. Physik **33**, 408 (1925).

[32] F. Reiche and W. Thomas, Z. Physik **34**, 510–525 (1925).

[33] C. Djalali, N. Marty, M. Morlet, and A. Willis, Nucl. Phys. A **380**, 42 (1982).

[34] A. Zilges, Jour. Phys.: Conference Series **590**, 012006 (2015).

[35] D. Savran, T. Aumann, and A. Zilges, Prog. Part. Nucl. Phys. **70**, 210 (2013).

[36] G. A. Bartholomew, Ann. Rev. Nucl. Sci. **11**, 259 (1961).

[37] R. Mohan, M. Danos, and L. C. Biedenharn, Phys. Rev. C **3**, 468 (1971).

[38] J. Piekarewicz, Phys. Rev. C **73**, 044325 (2006).

[39] A. Klimkiewicz, N. Paar, P. Adrich, M. Fallot, K. Boretzky, T. Aumann, D. Cortina-Gil, U. D. Pramanik, T. W. Elze, H. Emling, H. Geissel, M. Hellström, K. L. Jones, J. V. Kratz, R. Kulessa, C. Nociforo, R. Palit, H. Simon, G. Surówka, K. Sümmerer, D. Vretenar, and W. Waluś (LAND Collaboration), Phys. Rev. C **76**, 051603 (2007).

[40] S. Goriely, Physics Letters B **436**, 10 (1998).

[41] R. Neveling, H. Fujita, F. Smit, T. Adachi, G. Berg, E. Buthelezi, J. Carter, J. Conradie, M. Couder, R. Fearick, S. Förtsch, D. Fourie, Y. Fujita, J. Görres, K. Hatanaka, M. Jingo, A. Krumbholz, C. Kureba, J. Mira, S. Murray, P. von Neumann-Cosel, S. O'Brien, P. Papka, I. Poltoratska, A. Richter, E. Sideras-Haddad, J. Swartz, A. Tamii, I. Usman, and J. van Zyl, Nuclear Instruments and Methods in Physics Research Section A: Accelerators, Spectrometers, Detectors and Associated Equipment **654**, 29 (2011).

[42] T. Adachi, Y. Fujita, A. D. Bacher, G. P. A. Berg, T. Black, D. De Frenne, C. C. Foster, H. Fujita, K. Fujita, K. Hatanaka, M. Honma, E. Jacobs, J. Jänecke, K. Kanzaki, K. Katori, K. Nakanishi, A. Negret, T. Otsuka, L. Popescu, D. A. Roberts, Y. Sakemi, Y. Shimbara, Y. Shimizu, E. J. Stephenson, Y. Tameshige, A. Tamii, M. Uchida, H. Ueno, T. Yamanaka, M. Yosoi, and K. O. Zell, Phys. Rev. C **85**, 024308 (2012).

[43] P. von Neumann-Cosel, A. Richter, Y. Fujita, and B. D. Anderson, Phys. Rev. C **55**, 532 (1997).

[44] Y. Fujita, H. Akimune, I. Daito, M. Fujiwara, M. N. Harakeh, T. Inomata, J. Jänecke, K. Katori, C. Lüttge, S. Nakayama, P. von Neumann-Cosel, A. Richter, A. Tamii, M. Tanaka, H. Toyokawa, H. Ueno, and M. Yosoi, Phys. Rev. C **55**, 1137 (1997).

[45] G. Eulenberg, D. Sober, W. Steffen, H.-D. Gräf, G. Küchler, A. Richter, E. Spamer, B. Metsch, and W. Knüpper, Phys. Lett. B **116**, 113 (1982).

[46] D. I. Sober, B. C. Metsch, W. Knüpfer, G. Eulenberg, G. Küchler, A. Richter, E. Spamer, and W. Steffen, Phys. Rev. C **31**, 2054 (1985).

[47] F. Diel, Y. Fujita, H. Fujita, F. Cappuzzello, E. Ganioglu, E. Grewe, T. Hashimoto, K. Hatanaka, M. Honma, T. Itho, J. Jolie, B. Liu, T. Otsuka, K. Takahisa, G. Susoy, B. Rubio, and A. Tamii, Phys. Rev. C **In Revision** (2018).

[48] K. Langanke and G. Martınez-Pinedo, Rev. Mod. Phys. **819**, 75 (2003).

[49] T. Otsuka, M. Honma, T. Mizusaki, N. Shimizu, and Y. Utsuno, Prog. Part. Nucl. Phys. **47**, 319 (2001).

[50] M. Honma, T. Otsuka, T. Mizusaki, M. Hjorth-Jensen, and B. Brown, J. Phys.: Conf. Ser. **20**, 7 (2005).

[51] M. Honma, T. Otsuka, B. A. Brown, and T. Mizusaki, Phys. Rev. C **65**, 061301 (2002).

[52] M. Honma, T. Otsuka, B. A. Brown, and T. Mizusaki, Phys. Rev. C **69**, 034335 (2004).

[53] E.-W. Grewe, C. Bäumer, H. Dohmann, D. Frekers, M. N. Harakeh, S. Hollstein, H. Johansson, K. Langanke, G. Martínez-Pinedo, F. Nowacki, I. Petermann, L. Popescu, S. Rakers, D. Savran, K. Sieja, H. Simon, J. H. Thies, A. M. v. d. Berg, H. J. Wörtche, and A. Zilges, Phys. Rev. C **77**, 064303 (2008).

[54] G. W. Hitt, R. G. T. Zegers, S. M. Austin, D. Bazin, A. Gade, D. Galaviz, C. J. Guess, M. Horoi, M. E. Howard, W. D. M. Rae, Y. Shimbara, E. E. Smith, and C. Tur, Phys. Rev. C **80**, 014313 (2009).

[55] S. A. Martin, A. Hardt, J. Meissburger, G. P. Berg, U. Hacker, W. Hürlimann, J. G. Römer, T. Sagefka, A. Retz, O. W. Schult, K. L. Brown, and K. Halbach, Nucl. Instr. and Meth. **214**, 281 (1983).

[56] G. Berg, L. Bland, D. DuPlantis, C. Foster, D. Miller, P. Schwandt, R. Sawafta, K. Solberg, and E. Stephenson, IUCF Ann. Rep. (1986).

[57] A. Bacher, G. Berg, D. Bilodeau, C. Foster, J. Lisantti, T. Rinckel, P. Schwandt, E. Stephenson, Y. Wang, and S. Wells, IUCF Ann. Rep. (1990).

[58] G. Berg, S. Wells, Y. Wang, T. Hall, A. Bacher, D. Bilodeau, J. Doskow, G. East, C. Foster, J. Lisantti, T. Rinckel, P. Schwandt, E. Stephenson, and W. Braithwaite, IUCF Ann. Rep. (1991).

[59] G. Berg, S. Wells, A. Bacher, S. Bowyer, S. Chang, M. Clark, J. Crail, C. Foster, W. Franklin, J. Hall, T. annd Liu, E. Stephenson, and S. Wissink, IUCF Ann. Rep. (1993).

[60] H. Fujita, G. Berg, Y. Fujita, K. Hatanaka, T. Noro, E. Stephenson, C. Foster, H. Sakaguchi, M. Itoh, T. Taki, K. Tamura, and H. Ueno, Nucl. Instr. Meth. A **469**, 55 (2001).

[61] T. Wakasa, K. Hatanaka, Y. Fujita, G. Berg, H. Fujimura, H. Fujita, M. Itoh, J. Kamiya, T. Kawabata, K. Nagayama, T. Noro, H. Sakaguchi, Y. Shimbara, H. Takeda, K. Tamura, H. Ueno, M. Uchida, M. Uraki, and M. Yosoi, Nucl. Instr. Meth. A **482**, 79 (2002).

[62] H. Fujita, Y. Fujita, G. Berg, A. Bacher, C. Foster, K. Hara, K. Hatanaka, T. Kawabata, T. Noro, H. Sakaguchi, Y. Shimbara, T. Shinada, E. Stephenson, H. Ueno, and M. Yosoi, Nucl. Instr. Meth. A **484**, 17 (2002).

[63] A. Tamii, Y. Fujita, H. Matsubara, T. Adachi, J. Carter, M. Dozono, H. Fujita, K. Fujita, H. Hashimoto, K. Hatanaka, T. Itahashi, M. Itoh, T. Kawabata, K. Nakanishi, S. Ninomiya, A. Perez-Cerdan, L. Popescu, B. Rubio, T. Saito, H. Sakaguchi, Y. Sakemi, Y. Sasamoto, Y. Shimbara, Y. Shimizu, F. Smit, Y. Tameshige, M. Yosoi, and J. Zenhiro, Nucl. Inst. Meth. A **605**, 326 (2009).

[64] A. Botha, H. Jungwirth, and F. Marti, eds., *Cyclotrons and their applications. Proceedings, 10th International Conference, East Lansing, USA, April 30 - May 3, 1984*, IEEE (IEEE, Piscataway, USA, 1984).

[65] H. Enge, Nucl. Instr. and Meth. **187**, 1 (1981).

[66] Technoland Corporation, Model P-TM 005, 16 Channel Preamplifier and Discriminator Card.

[67] CAEN, Model V1190A, 128 Channel Multievent Time-to-Digital Converter.

[68] The MIDAS (Maximum Integration Data Acquisition System) Data Acquisition System, Paul Scherrer Institute, https://midas.psi.ch.

[69] B. L. Cohen, Rev. Sci. Inst. **30**, 415 (1959), https://doi.org/10.1063/1.1716643 .

[70] K. Brown, R. F., D. C. Carey, and C. Iselin, CERN-80-04 (1983).

[71] R. Neveling, F. Smit, H. Fujita, P. Adsley, K. Li, J. Brümmer, Marín-Lambárri, and R. Newman, K600 manual **Unpublished** (2017).

[72] H. Fujita, G. Berg, Y. Fujita, K. Hatanaka, T. Noro, E. Stephenson, C. Foster, H. Sakaguchi, M. Itoh, T. Taki, K. Tamura, and H. Ueno, Nucl. Instr. Meth. A **17**, 469 (2002).

[73] H. Wollnik, *Optics of charged Particles* (Academic Press, San Diego, 1987).

[74] R. Kehl, Masters Thesis **Unpublished** (Cologne, 2018).

[75] W. Bertozzi, M. Hynes, C. Sargent, C. Creswell, P. Dunn, A. Hirsch, M. Leitch, B. Norum, F. Rad, and T. Sasanuma, Nucl. Inst. Meth. **141**, 457 (1977).

[76] R. Leo, *Techniques for Nuclear and Particle Physics Experiments* (1994).

[77] J. Davidson, N. Jarmie, and A. Niethammer, (1969).

[78] J. Kelley, J. Purcell, and C. She, NP A968, 71 (2017).

[79] F. Ajzenberg-selove, J. Kelley, and C. Nesaraja, NP A523,1 (1991).

[80] M. S. Basunia and A. M. Hurs, NDS 134, 1 (2016).

[81] B. Singh, NDS 108, 197 (2007).

[82] H. Fujita, (2013), private Communication.

[83] J. Raynal, computer code DWBA98, NEA , 1209/05 (1998).

[84] P. Schwandt, H. O. Meyer, W. W. Jacobs, A. D. Bacher, S. E. Vigdor, M. D. Kaitchuck, and T. R. Donoghue, Phys. Rev. C **26**, 55 (1982).

[85] A. Bohr and B. R. Mottelson, *Nuclear structure*, Vol. 2 (Benjamin,New York, 1975).

[86] M. Hofstee, S. van der Werf, A. van den Berg, N. Blasi, J. Bordewijk, W. Borghols, R. D. Leo, G. Emery, S. Fortier, S. Galès, M. Harakeh, P. den Heijer, C. de Jager, H. Langevin-Joliot, S. Micheletti, M. Morlet, M. Pignanelli, J. Schippers, H. de Vries, A. Willis, and A. van der Woude, Nucl. Phys. A **588**, 729 (1995).

[87] S. van der Werf, KVI Groningen (1991), computer code NORMOD (unpublished).

[88] Y. Shimbara, Y. Fujita, T. Adachi, G. P. A. Berg, H. Fujimura, H. Fujita, K. Fujita, K. Hara, K. Y. Hara, K. Hatanaka, J. Kamiya, K. Katori, T. Kawabata, K. Nakanishi, G. Martìnez-Pinedo, N. Sakamoto, Y. Sakemi, Y. Shimizu, Y. Tameshige, M. Uchida, M. Yoshifuku, and M. Yosoi, Phys. Rev. C **86**, 024312 (2012).

[89] Y. Fujita, (2013), private Communication.

[90] R. Firestone and V. Shirley, *Table of Isotopes*, 8th ed. (John Wiley & Sons, Inc., New York, 1996).

[91] L. Popescu, T. Adachi, G. P. A. Berg, P. v. Brentano, D. Frekers, D. D. Frenne, K. Fujita, Y. Fujita, E. W. Grewe, M. N. Harakeh, K. Hatanaka, E. Jacobs, K. Nakanishi, A. Negret, Y. Sakemi, Y. Shimbara, Y. Shimizu, Y. Tameshige, A. Tamii, M. Uchida, H. J. Wörtche, and M. Yosoi, Phys. Rev. C **79**, 064312 (2009).

[92] S. Rakers, C. Bäumer, A. M. van den Berg, B. Davids, D. Frekers, D. De Frenne, Y. Fujita, E.-W. Grewe, P. Haefner, M. N. Harakeh, M. Hunyadi, E. Jacobs, H. Johansson, B. C. Junk, A. Korff, A. Negret, L. Popescu, H. Simon, and H. J. Wörtche, Phys. Rev. C **70**, 054302 (2004).

[93] E.-W. Grewe, D. Frekers, S. Rakers, T. Adachi, C. Bäumer, N. T. Botha, H. Dohmann, H. Fujita, Y. Fujita, K. Hatanaka, K. Nakanishi, A. Negret, R. Neveling, L. Popescu, Y. Sakemi, Y. Shimbara, Y. Shimizu, F. D. Smit, Y. Tameshige, A. Tamii, J. Thies, P. v. Brentano, M. Yosoi, and R. G. T. Zegers, Phys. Rev. C **76**, 054307 (2007).

[94] S. Rakers, C. Bäumer, A. M. v. d. Berg, B. Davids, D. Frekers, D. D. Frenne, E.-W. Grewe, P. Haefner, M. N. Harakeh, S. Hollstein, M. Hunyadi, E. Jacobs, B. C. Junk, A. Korff, A. Negret, L. Popescu, and H. J. Wörtche, Phys. Rev. C **71**, 054313 (2005).

[95] M. Honma, (2015), private Communication.

[96] Y. Fujita, T. Adachi, H. Fujita, A. Algora, B. Blank, M. Csatlós, J. M. Deaven, E. Estevez-Aguado, E. Ganioğlu, C. J. Guess, J. Gulyás, K. Hatanaka, K. Hirota, M. Honma, D. Ishikawa, A. Krasznahorkay, H. Matsubara, R. Meharchand, F. Molina, H. Okamura, H. J. Ong, T. Otsuka, G. Perdikakis, B. Rubio, C. Scholl, Y. Shimbara, E. J. Stephenson, G. Susoy, T. Suzuki, A. Tamii, J. H. Thies, R. G. T. Zegers, and J. Zenihiro, Phys. Rev. C **88**, 014308 (2013).

[97] E. Ganioğlu, H. Fujita, B. Rubio, Y. Fujita, T. Adachi, A. Algora, M. Csatlós, J. M. Deaven, E. Estevez-Aguado, C. J. Guess, J. Gulyás, K. Hatanaka, K. Hirota, M. Honma, D. Ishikawa, A. Krasznahorkay, H. Matsubara, R. Meharchand, F. Molina, H. Okamura, H. J. Ong, T. Otsuka, G. Perdikakis, C. Scholl, Y. Shimbara, G. Susoy, T. Suzuki, A. Tamii, J. H. Thies, R. G. T. Zegers, and J. Zenihiro, Phys. Rev. C **93**, 064326 (2016).

[98] Y. Fujita, H. Fujita, B. Rubio, W. Gelletly, and B. Blank, Act. Phys. Pol. B **43**, 463 (2012).

[99] H. Fujita, Y. Fujita, T. Adachi, H. Akimune, N. T. Botha, K. Hatanaka, H. Matsubara, K. Nakanishi, R. Neveling, A. Okamoto, Y. Sakemi, T. Shima, Y. Shimizu, F. D. Smit, T. Suzuki, A. Tamii, and M. Yosoi, Phys. Rev. C **88**, 054329 (2013).

[100] L. Popescu, Private Communication.

[101] Y. Fujita, H. Fujita, T. Adachi, C. L. Bai, A. Algora, G. P. A. Berg, P. von Brentano, G. Colò, M. Csatlós, J. M. Deaven, E. Estevez-Aguado, C. Fransen, D. De Frenne, K. Fujita, E. Ganioğlu, C. J. Guess, J. Gulyás, K. Hatanaka, K. Hirota, M. Honma, D. Ishikawa, E. Jacobs, A. Krasznahorkay, H. Matsubara, K. Matsuyanagi, R. Meharchand, F. Molina, K. Muto, K. Nakanishi, A. Negret, H. Okamura, H. J. Ong, T. Otsuka, N. Pietralla, G. Perdikakis, L. Popescu, B. Rubio, H. Sagawa, P. Sarriguren, C. Scholl, Y. Shimbara, Y. Shimizu, G. Susoy, T. Suzuki, Y. Tameshige, A. Tamii, J. H. Thies, M. Uchida, T. Wakasa, M. Yosoi, R. G. T. Zegers, K. O. Zell, and J. Zenihiro, Phys. Rev. Lett. **112**, 112502 (2014).

[102] T. Inakura, T. Nakatsukasa, and K. Yabana, Phys. Rev. C **84**, 021302 (2011).

[103] A. Stolz, T. Baumann, N. Frank, T. Ginter, G. Hitt, E. Kwan, M. Mocko, W. Peters, A. Schiller, C. Sumithrarachchi, and M. Thoennessen, Phys. Lett. B **627**, 32 (2005).

[104] S. Khan, Ph.D. thesis, Max Planck Institut, Heidelberg (1987).

[105] Y. Fujita, K. Hatanaka, G. Berg, K. Hosono, N. Matsuoka, S. Morinobu, T. Noro, M. Sato, K. Tamura, and H. Ueno, Nucl. Instr. and Meth. B **274**, 126 (1997).

List of Figures

List of Tables

Erklärung

Ich versichere, dass ich die von mir vorgelegte Dissertation selbständig angefertigt, die benutzten Quellen und Hilfsmittel vollständig angegeben und die Stellen der Arbeit - einschließlich Tabellen, Karten und Abbildungen - , die anderen Werken im Wortlaut oder Sinn nach entnommen sind, in jedem Einzelfall als Entlehnung kenntlich gemacht habe; dass diese Dissertation noch keiner anderen Fakultät oder Universität zur Prüfung vorgelegen hat; dass sie - abgesehen von den angegebenen Teilpublikationen - noch nicht veröffentlicht worden ist sowie, dass ich eine solche Veröffentlichung vor Abschluss des Promotionsverfahrens nicht vornehmen werde. Die Bestimmungen der Promotionsordnung sind mir bekannt. Die von mir vorgelegte Dissertation ist von Prof. Dr. Jan Jolie betreut worden.

Teilpublikationen

1 F. Diel, Y. Fujita, H. Fujita, *et al.*, Phys. Rev. C **In Revision** (2018)

2 E.-W. Grewe *et al.*, Phys. Rev. C **77**, 064303 (2008)

Köln, im März 2019

(Felix Diel)